OPTICAL SPECTROSCOPY OF DONOR BOUND EXCITONS AND SPIN RELAXATION OF DONOR ELECTRONS IN ISOTOPICALLY ENRICHED SILICON

Von der Fakultät für Mathematik und Physik
der Gottfried Wilhelm Leibniz Universität Hannover

zur Erlangung des akademischen Grades
Doktor der Naturwissenschaften
Dr. rer. nat.

genehmigte Dissertation
von

M.Sc. Michael Beck

2019

Referent: Prof. Dr. Michael Oestreich
Korreferent: Prof. Dr. Fei Ding
Korreferent: Prof. Dr. Christian Schüller
Tag der Promotion: 22.08.2019

ABSTRACT

The spin of electrons bound to neutral phosphorus donors in isotopically enriched silicon is a promising candidate for future quantum information processing. In this thesis, the intriguing properties of the associated optical transition, i.e., the donor bound exciton (D^0X) transition are investigated by means of high precision laser absorption spectroscopy. The ultra-narrow spectral linewidth of the D^0X transition allows for individual optical addressability of the electron spin and the phosphorus nuclear spin which is used to unambiguously quantify the microscopic origin of the enhanced donor electron spin lattice relaxation rate caused by optical excitation. For this purpose, the transient decay of the donor electron polarization is studied via a time-resolved pump-probe absorption spectroscopy technique where a significant shortening of the polarization decay with increasing laser excitation is observed. The theoretical analysis of the complete optically driven donor system shows that this shortening is caused by the creation of free electrons via the ubiquitous D^0X Auger recombination. It is shown that, in addition to electron-phonon interaction, the hot Auger electrons relax their excess energy via inelastic collisions with donors and promote the donor electron from the ground state to a spin-mixed excited state giving rise to an Orbach-type spin relaxation mechanism which sets a fundamental limit to the spin relaxation and spin coherence time of optically driven donor systems. Furthermore, the ultra-narrow linewidth of the D^0X transition enables the test of fundamental semiconductor physics such as the low temperature behavior of the silicon bandgap and the extraction of material parameters like the Landé g-factors.

Keywords: Transient absorption spectroscopy,
optical spin pumping, spin relaxation

CONTENTS

LIST OF ACRONYMS, SYMBOLS AND CONSTANTS . 7

I INTRODUCTION AND FUNDAMENTALS

1 INTRODUCTION 13

2 FUNDAMENTALS 17

2.1 Isotopically Enriched Silicon 17

2.2 Donor Bound Electrons 19

2.3 Donor Bound Excitons and Optical Selection Rules . 24

2.4 Spin Relaxation of Bound Electrons in Silicon 26

II EXPERIMENTAL METHODS

ABSTRACT PART II 31

3 EXPERIMENTAL SETUP 33

3.1 Important Components 33

3.1.1 External Cavity Diode Laser 33

3.1.2 Electro-Optic Modulator 35

3.1.3 Cryostat 36

3.2 Optical Setup 37

3.3 Home-Built Helium Reservoir 39

4 PHASE MODULATION SPECTROSCOPY 43

III A HIGH STABILITY DIODE LASER FOR SPECTROSCOPY OF ULTRA LOW DOPED SILICON

ABSTRACT PART III 51

5 CAVITY FUNDAMENTALS AND DESIGN 53

5.1 The Fabry Perot Cavity 53

5.2 Cavity Design Considerations 54

5.3 FEM Simulation 55

5.4 Cavity Mounting and Temperature Stabilization . . 59

5.5 The Pound-Drever-Hall Technique 62

6 EVALUATION OF CAVITY PARAMETERS AND STABILITY 65

6.1 Evaluation of Stability and Calibration of the Wavemeter 65

6.2 Determination of the Zero Crossing Temperature . . 69

IV ABSORPTION SPECTROSCOPY OF DONOR BOUND EXCITONS

ABSTRACT PART IV 75

7 ABSORPTION WITHOUT MAGNETIC FIELD 77

7.1 Absorption Coefficient of the No-Phonon Line 77

7.2 Considerations on Spectral Width and Lineshape . . 79

7.3 Temperature Dependent Spectroscopy 82

8 ABSORPTION WITH MAGNETIC FIELD 87

8.1 Optical Selection Rules 87

8.2 Determination of the Landé g-Factors 90

V OPTICAL SPIN PUMPING OF DONOR BOUND ELECTRONS

ABSTRACT PART V 97

9 CONCEPTUAL IDEA AND MECHANISM 99

10 TIME RESOLVED POLARIZATION DECAY 105

10.1 Experimental Polarization Dynamics 105

10.2 A Microscopic Picture 109

VI OUTLOOK AND SUMMARY

ABSTRACT PART VI 119

11 OUTLOOK 121

11.1 Spin and Occupation Noise Spectroscopy 121

11.2 Optical Spin Injection and Detection 131

12 SUMMARY 137

VII APPENDIX

ABSTRACT 143

A EXCITON FORMATION IN GALLIUM ARSENIDE 145

BIBLIOGRAPHY 151

LIST OF FIGURES 161

LIST OF TABLES 163

SCIENTIFIC CONTRIBUTIONS 167

CURRICULUM VITAE 171

ACKNOWLEDGMENTS 173

LIST OF ACRONYMS, SYMBOLS AND CONSTANTS

ACRONYMS

BR	Balanced Receiver
BS	Beamsplitter
CAD	Computer-Aided Design
CTE	Coefficient of Thermal Expansion
DBR	Distributed Bragg Reflector
DSO	Digital Storage Oscilloscope
DSP	Degree of Spin Polarization
D^0	Donor Bound Electron
D^0X	Donor Bound Exciton
ECDL	External Cavity Diode Laser
EOM	Electro-Optic Modulator
FWHM	Full Width at Half Maximum
FEM	Finite Element Method
HWHM	Half Width at Half Maximum
HWP	Half-Wave Plate
IGP	Ion Getter Pump
LCR	Liquid Crystal Retarder
LP	Linear Polarizer
MBE	Molecular Beam Epitaxy
OVC	Outer Vacuum Chamber
PDH	Pound-Drever-Hall
PSD	Power Spectral Density
QWP	Quarter-Wave Plate
ULE	Ultra Low Expansion glass
SNS	Spin Noise Spectroscopy
WLM	Wavelength Meter or Wavemeter

SYMBOLS

A	phosphorus donor hyperfine coupling constant
a	factor in the linear CTE of ULE
a_B	bohr radius
$a_{B,D}$	donor electron bohr radius
$a_{B,X}$	exciton bohr radius
a_0	lattice constant
B	magnetic field
E_D	donor binding energy
E_L	bound exciton localization energy
E_X	exciton binding energy
E_0	Orbach constant
$\mathcal{F}$	finesse
G	optical excitation rate
g_e	electron g-factor
$g_{1/2}$	light hole g-factor
$g_{3/2}$	heavy hole g-factor
$\mathcal{H}$	Hamilton operator
$\mathbf{I}$	nuclear spin
L	length
m^*	effective electron mass
n	dispersive part of the refractive index
n_d	donor density
$n_{d,i}$	ionized donor density
R	reflectivity
$\mathbf{S}$	electron spin
$S_{\Delta\nu}(f)$	laser frequency noise PSD
T	temperature
T_0	cavity zero-crossing temperature
T_1	longitudinal spin relaxation time
T_2	spin dephasing time
T_2^*	inhomogeneous spin dephasing time

T_X	donor cross-relaxation time
w_0	focused $1/e^2$ laser beam radius
α	dissipative part of the refractive index (absorption coefficient)
α_p	pressure coefficient of the WLM calibration
β	low energy stretching factor of the skewed Lorentzian
β_T	pressure coefficient of the WLM calibration
Γ	FWHM linewidth of the $\mathrm{D^0X}$ transition
Γ_0	low temperature FWHM linewidth of the $\mathrm{D^0X}$ transition
$\Gamma_{D^0T_2}$	decay rate of the excited 1S-$\mathrm{T_2}$ donor state
γ	HWHM linewidth of the $\mathrm{D^0X}$ transition
Δ	energy difference between the donor 1S-$\mathrm{A_1}$ and 1S-$\mathrm{T_2}$ state
Δ_P	pump laser detuning
$\Delta\nu_{rms}$	root mean square laser linewidth
δ	ULE ring coupling parameter
ϵ_r	relative permittivity
ζ	Number of collision a single hot Auger electron performs with one donor
η	Total energy loss of one Auger electron due to inelastic collisions with donors
Θ_F	Faraday rotation angle
κ	time constant of free exciton cooling
λ	wavelength
μ^*	reduced effective mass
ν	laser frequency
Π	linear polarization
ρ	donor electron spin polarization
$\sigma^{+(-)}$	left-handed (right-handed) circular polarization
τ	lifetime
τ_A	$\mathrm{D^0X}$ Auger lifetime
τ_{DAP}	donor acceptor pair recombination time constant
τ_c	capture time
Ω	phase modulation frequency

ω	laser angular frequency

CONSTANTS

c	vacuum speed of light, $2.997\,924\,58 \times 10^{8}\,\mathrm{m\,s^{-1}}$
e	elementary charge, $1.602\,176\,62 \times 10^{-19}\,\mathrm{C}$
h	planck constant, $6.626\,070\,15 \times 10^{-34}\,\mathrm{J\,s}$
$\hbar$	reduced planck constant, $1.054\,571\,817 \times 10^{-34}\,\mathrm{J\,s}$
k_B	Boltzmann constant, $1.380\,649 \times 10^{-23}\,\mathrm{J\,s^{-1}}$
m_0	free electron mass, $9.109\,383\,70 \times 10^{-31}\,\mathrm{kg}$
ϵ_0	vacuum permittivity, $8.854\,187\,812\,8 \times 10^{-12}\,\mathrm{A\,s\,V^{-1}\,m}$

Part I

INTRODUCTION AND FUNDAMENTALS

1

INTRODUCTION

Silicon is one of the most important semiconductors and forms the building block of the information age due to its versatile use in integrated circuits. This was only made possible through decades of extensive research regarding electronic transport properties and the physics of shallow dopants. Besides the charge degree of freedom, shallow impurities also possess an additional spin degree of freedom which has the potential to revolutionize conventional charge-based electronics [1, 2, 3]. The understanding of the spin physics of localized states began in 1954 with the first electron spin resonance experiments by Fletcher et al. [4] and the first relaxation time measurement by Honig [5]. Supported by theoretical studies on the electronic structure and spin relaxation [6, 7, 8, 9] Feher et al. have contributed three related publications [10, 11, 12] which count up to now to the most comprehensive experimental studies on shallow impurities in silicon. Using the electron nuclear double resonance (ENDOR) technique they were able to determine the electronic structure of the ground states and excited states of donors and the Landé g-factor of electrons. Most importantly, they find that the donor electron spin exhibits extremely long T_1 relaxation times with a reported value of $\approx 3000\,\mathrm{s}$ at $1.25\,\mathrm{K}$. Under these conditions, the phosphorus nuclear spin relaxation time exceeded $10\,\mathrm{h}$.

In 1998, these extraordinarily long relaxation times lead Kane to the proposal of a quantum computer based on the hyperfine coupled system of the phosphorus donor electron and nuclear spin [1]. In this framework, the donor system will serve as the smallest unit of information storage, the so called qubit, which allows for the storage of superposition states, the key ingredient to the potentially superior performance of quantum computers. The qubit itself could, in principle, consist of any well defined quantum mechanical two-level system as provided in semiconductor quantum dots [13] or the nitrogen vacancy center in diamond [14]. However, the existing know-how in the field of silicon growth, processing, and device fabrication favors silicon as the host for future quantum information processing. Despite its numerous advantages, the relatively short coherence lifetime T_2 on the ms scale at low temperatures [15, 16, 17] constitutes a drawback. Even though coherent control of a single spin-qubit in natural silicon has been demonstrated [18], longer T_2 times are desirable for quantum computation. One reason for this striking discrepancy between the T_1 and the T_2 time can be found in the presence of ^{29}Si isotopes with a nuclear spin $I = 1/2$ and an abundance of $\approx 4.7\,\%$ in natural silicon. These nuclear spins are mutually coupled by dipolar interaction leading to spin flip-flops. This is sensed as random field fluctuations by the donor electron and thus leading to decoherence, an effect which has been termed nuclear-induced spectral diffusion [19, 20]. This problem was circumvented in 2004 in the course of the Avogadro project [21] where isotopically purified crystals containing $> 99.99\,\%$ of ^{28}Si became available which has extended the coherence time of the donor electron spins to $\approx 10\,\mathrm{s}$ [22].

The availability of highly enriched silicon not only brought about an increase in spin coherence but also had a significant impact on the optical properties. The optical recombination of an exciton bound to a neutral phosphorus donor ($\mathrm{D^0X}$) in natural silicon was already one of the narrowest transitions in the solid state with an optical width of $\approx 1.2\,\mathrm{GHz}$ [23]. The lack of isotopical randomness and the associated fluctuation in the bandgap energy in ^{28}Si drastically reduced the width to $\approx 36\,\mathrm{MHz}$ [24] and finally a width of $\approx 4.8\,\mathrm{MHz}$ was found in a so called hole burning experiment [25] which is remarkably close to the 585 kHz natural linewidth set by the 272 ns Auger decay time [26]. Most strikingly, the linewidth has decreased below the value of the donor ground state hyperfine coupling constant $A = 117.53\,\mathrm{MHz}$ [10] which enables the optical addressability of a specific donor or nuclear spin state by means of optical spectroscopy [24]. In the context of qubit initialization, it has been shown that this individual addressability can be used to polarize the donor spin ensemble up to $90\,\%$ via selective spin pumping [27]. The latter has paved the way for hybrid techniques where qubit initialization and readout is achieved by optical means and coherent manipulation is accomplished by conventional electron spin resonance or nuclear magnetic resonance techniques [28, 29, 30].

A common feature to all schemes where qubit initialization is realized by optical means is the generation of free electrons via the $\mathrm{D^0X}$ Auger decay and it has been recognized that the existence of free electrons enhances the donor spin relaxation rate [27]. Earlier studies [11] have also noted this enhancement but a convincing, quantitative microscopic picture did not exist so far. This is the point where the present work sets in.

In this thesis, the spin dynamics of the donor bound electron system is investigated under the influence of optically induced carriers where a time-resolved pump-probe absorption spectroscopy technique is utilized to monitor the transient electron polarization decay. In order to quantitatively account for the polarization decay, a set of coupled differential rate equations for the complete optically driven donor system is solved. It is found that each hot Auger electron collides on average with $\zeta = 3.2$ donors while promoting the donor electron from the A_1 ground state to the T_2 excited state, giving rise to an Orbach-type spin relaxation mechanism [31]. This physical picture is supported by complementary calculations of the transient energy loss of hot electrons mediated by acoustic and optical phonons. Therefore, this mechanism provides a fundamental limit to the spin pumping efficiency and quantifies the trade-off relation between a high degree of spin polarization and slow longitudinal spin relaxation.

This work is organized as follows: Part I summarizes the required theoretical prerequisites on the material system under investigation and the electronic structure of shallow donors in silicon and defines the optical selection rules associated with donor bound excitons. In part II the optical setup for (pump-probe) absorption spectroscopy of donor bound excitons is outlined where special focus is placed on the phase modulation technique. Part III introduces a laser frequency stabilization scheme based on a high finesse Fabry Perot resonator. It is shown that the resulting laser frequency stability is in principle sufficient to resolve even the natural linewidth of bound excitons which is $< 1\,\mathrm{MHz}$. In part IV the fundamental properties of the $\mathrm{D}^0\mathrm{X}$ are investigated under external parameters, i.e, temperature and magnetic field. Part V reveals the influence of optically induced carriers on the donor T_1 time (see above). Finally, part VI provides a detailed outlook on the feasibility of spin noise spectroscopy in silicon and suggests the $\mathrm{D}^0\mathrm{X}$ transition as an excellent detector for optical spin injection.

2

FUNDAMENTALS

2.1 ISOTOPICALLY ENRICHED SILICON

Silicon is located in the group IV (carbon group) of the periodic table of elements with an atomic number of 14 and four valance electrons under normal conditions. It crystallizes in the cubic diamond structure (see Fig. 2.1) which consists of two interleaved face centered cubic (fcc) lattices displaced by $(\frac{a_0}{4}, \frac{a_0}{4}, \frac{a_0}{4})$ where $a_0 = 5.43\,\text{Å}$ is the lattice constant [32]. The symmetry properties of the lattice directly lead to the electronic bandstructure depicted in Fig. 2.2 which has been obtained using a local-pseudopotential method (solid lines) [33]. The dashed lines are experimental data. The maximum of the top valance band $(E = 0)$ occurs at $\mathbf{k} = 0$,

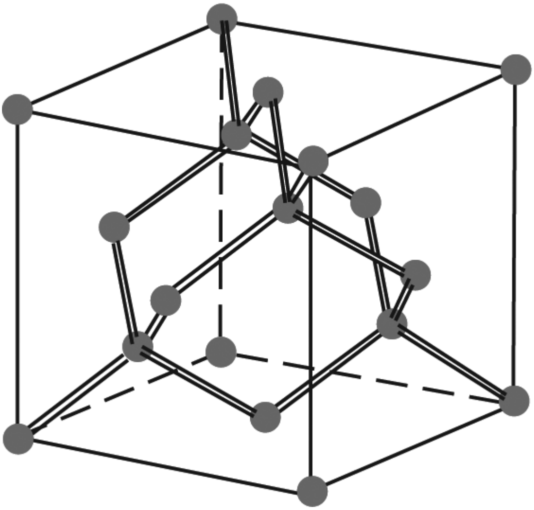

Figure 2.1: Crystal structure of silicon. Adapted from [32].

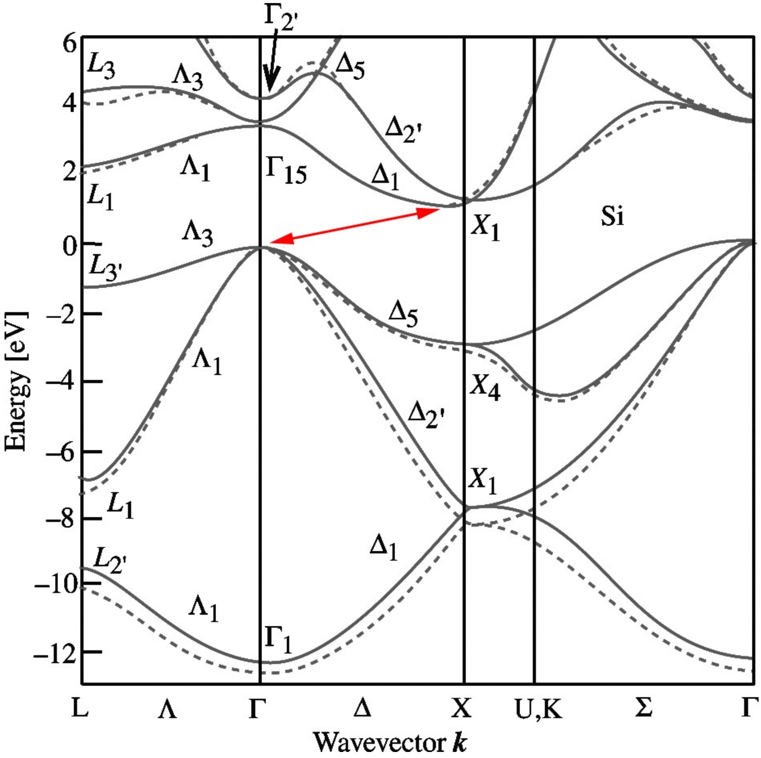

Figure 2.2: Local pseudo-potential calculation of the silicon bandstructure (solid lines) and experimental data (dashed lines). Adapted from [33].

the so called Γ-point. The minimum of the lowest conduction band however, is not located at the Γ-point but rather lies approximately 85 % towards the Brillouin zone boundary (X-point). Therefore, silicon is termed an indirect semiconductor which is responsible for the inherent weakness of optical processes across the indirect gap (red arrow in Fig. 2.2). A further implication of the indirect bandgap is the multivalley structure of the conduction band which plays an important role in the energy spectrum of electrons bound to shallow impurities (compare chapter 2.2). In nature, three stable silicon isotopes exist which are listed in table 2.1.

Isotope	Nuclear spin	natural abundance (%)
^{28}Si	0	92.33
^{29}Si	1/2	4.57
^{30}Si	0	3.10

Table 2.1: Natural abundance of silicon isotopes

The natural abundance of silicon isotopes suggests the elimination of the ^{29}Si and ^{30}Si isotopes. This has been achieved in the framework of the Avogadro project [21] which aimed at a re-definition of the Avogadro constant by counting the number of atoms in a sphere containing more than 99.99 % of the ^{28}Si isotope. The fabrication of such crystals requires several steps which are the centrifugation of SiF_4 gas, the subsequent conversion of the enriched gas to SiH_4, the growth of a polycrystal by chemical vapor deposition and finally the growth of a monocrystal by (several) float zone processes.
In this work, the sample under investigation is a cuboid with dimensions of 4 mm × 2 mm × 0.8 mm enriched to 99.994 % and a nominal phosphorus donor density of $n_d = 1.2 \times 10^{15}\,\mathrm{cm}^{-3}$.

2.2 DONOR BOUND ELECTRONS

Phosphorus (P) belongs to the group V of the periodic table of elements, holds one extra valance electron compared to silicon, and acts as a substitutional donor which behaves effectively like a hydrogen atom in the silicon lattice. The attractive Coulomb potential between the P nucleus and the extra electron is screened by the dielectric background of the silicon host and the remaining four valance electrons giving rise to the notion of a *hydrogen-like* impurity [32] where the extra electron is only loosely bound to the P donor. A theoretical description of this extra donor electron is usually accomplished by assuming that the positive charge of the P nucleus is screened by the dielectric background of the host. Therefore the attractive Coulomb potential reads [32]

$$V_S = +\frac{|e|}{4\pi\epsilon_0\epsilon_r r}, \tag{2.1}$$

where ϵ_0 is the vacuum permittivity, e is the elementary charge and ϵ_r is the dielectric constant of the silicon host. The corresponding Schrödinger equation is given by

$$(\mathcal{H}_0 - |e|\, V_S)\,\Psi(r) = E\Psi(r), \tag{2.2}$$

where $\mathcal{H}_0$ is the one-electron Hamiltonian of the perfect crystal and $\Psi(r)$ is the donor electron wave function. In silicon, the positions of valance band maximum and conduction band minimum do not coincide at the zone center and the conduction band minimum consists of six equivalent valleys which can be characterized by a second-rank effective mass tensor

$$\mathbf{m} = \begin{pmatrix} m_l & 0 & 0 \\ 0 & m_t & 0 \\ 0 & 0 & m_t \end{pmatrix}, \tag{2.3}$$

where the subscripts $l(t)$ denote the direction longitudinal(transverse) to the [100] axis. Taking this into account, the Schrödinger equation can be expressed in the *effective mass approximation* as

$$\left[-\left(\frac{\hbar^2}{2}\right)\left(\frac{2\nabla_t^2}{m_t} + \frac{2\nabla_l^2}{m_l}\right) - |e|\, V_S\right] F_i(r) \approx \left[E - E_c(k_0)\right] F_i(r), \tag{2.4}$$

where $F_i(r)$ is the envelope wave function which is related to the complete donor electron wave function $\Psi(r)$ by [34]

$$\Psi(r) = \sum_{i=1}^{6} F_i(r)\phi_i(r), \tag{2.5}$$

where the index i runs over the six equivalent conduction band minima, and $\phi_i(r)$ is the rapidly varying Bloch function. Figure 2.3 illustrates $\Psi(r)$ in real space. In the simplest case of a parabolic conduction band with its minimum located at the Brillouin zone center, the energy levels of the donor electron are given by a modified Rydberg series

$$E - E_c(0) = -\frac{R}{N^2} \quad N = 1, 2, 3..., \tag{2.6}$$

where $E_c(0)$ is the conduction band minimum and R is the Rydberg constant for the donor electron which is related to the Rydberg constant R_H of the hydrogen atom by

$$R = \left(\frac{m^*}{m_0}\right)\left(\frac{1}{\epsilon_r^2}\right) R_H = \left(\frac{m^*}{m_0}\right)\left(\frac{1}{\epsilon_r^2}\right) \frac{m_0 e^4}{8\epsilon_0^2 h^2}, \tag{2.7}$$

where m^* is the effective band mass and m_0 is the free electron mass.

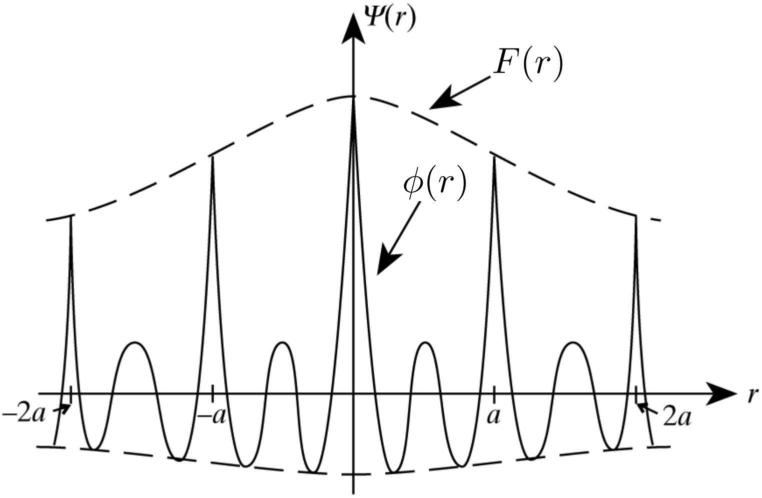

Figure 2.3: Real space representation of the donor electron wave function. $F(r)$ is the envelope function and $\phi(r)$ denotes the Bloch function. Adapted from [32].

The impurity central cell correction leads in the case of silicon to a coupling between the six degenerate conduction band valleys. This effect is known as *valley-orbit coupling* and splits the Rydberg ground state $N = 1$ into an A_1 ground state and two excited states labeled E and T_2 [1]. This is illustrated in Fig. 2.4 for several donor species. For the P donor, the values are $A_1 = -45.5\,\text{meV}$, $E = -32.6\,\text{meV}$ and $T_2 = -33.9\,\text{meV}$ [32]. Another important mechanism which alters the energy level of the donor ground state is the hyperfine interaction between the donor electron spin with operator $\mathbf{S}$ and the phosphorus nuclear spin with operator $\mathbf{I}$. For a magnetic field B oriented in z-direction, the interaction Hamiltonian $\mathcal{H}_{int}$ reads

$$\mathcal{H}_{int} = \gamma_e B S_z - \gamma_P B I_z + A\mathbf{S} \cdot \mathbf{I}, \tag{2.8}$$

where A is the hyperfine coupling constant between the donor ground state and the P nuclear spin. The constants γ_e and γ_P are

---

[1] It is customary to use the point group notations for the energy levels. This directly reveals the symmetry of the underlying wave function.

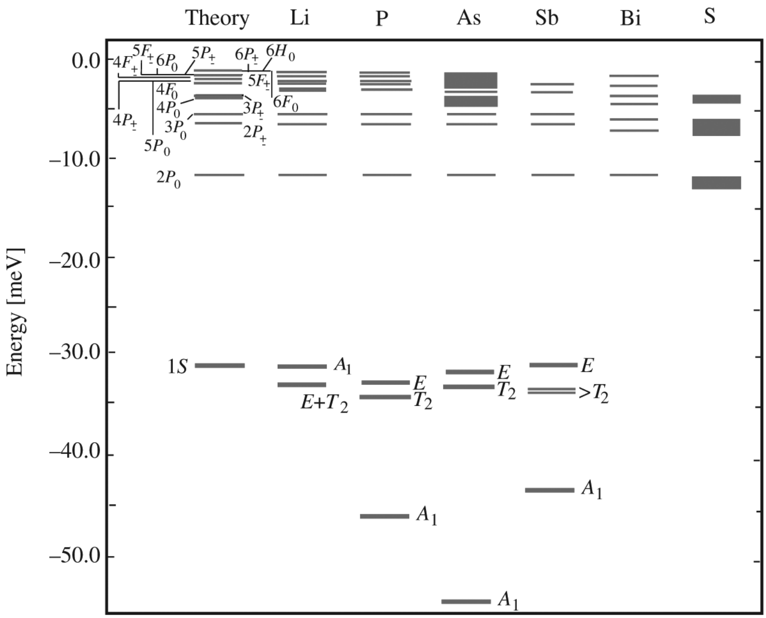

Figure 2.4: Theoretical and experimental donor energy levels of different donor species. Taken from [32].

the gyromagnetic ratios of the donor electron and the P nucleus respectively and are defined as

$$\gamma_e = \frac{g_e \mu_B}{h}, \quad \gamma_P = \frac{g_n \mu_N}{h}, \tag{2.9}$$

where g_e is the electron Landé g-factor, μ_B is the Bohr magneton, g_n is the nuclear Landé g-factor, μ_N is the nuclear magneton and h is the Planck constant.

The eigenvalues of Eq. 2.8 are given by the Breit-Rabi equation [35]

$$\begin{aligned} \Delta E = \frac{E(F = \pm 1/2, M)}{A} &= -\frac{1}{2(2I+1)} - \frac{M}{\gamma_e/\gamma_P - 1}x \\ &\pm \frac{1}{2}\sqrt{1 + \frac{4M}{2I+1}x + x^2}, \end{aligned} \tag{2.10}$$

where $F = S + I$ is the total angular momentum which is in the case of $^{28}\mathrm{Si}:\mathrm{P}$ either $F = 0$ for the singlet state or $F = 1$ for the triplet state. The number M is the projection of F and ranges from

$-F$ to F. Figure 2.5 shows the result of Eq. 2.10 as a function of the normalized magnetic field

$$x = \frac{(\gamma_e - \gamma_P)\,B}{A}. \tag{2.11}$$

Given that A amounts to 117.53 MHz for P donors in silicon [10], the energy splittings caused by hyperfine interaction are on the same scale as the optical linewidth Γ of the $\mathrm{D}^0\mathrm{X}$ transition.

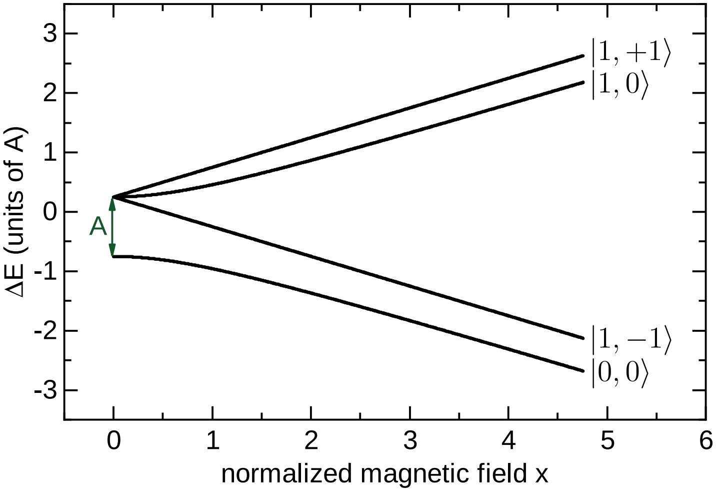

Figure 2.5: Evolution of the hyperfine coupled donor system according to the Breit-Rabi equation. The brackets denote $|F = S + I, M\rangle$.

2.3 DONOR BOUND EXCITONS AND OPTICAL SELECTION RULES

An exciton is a quasi-particle consisting of a free electron in the conduction band and a free hole in the valance band which are bound by Coulomb interaction. The exciton can be treated in analogy to the hydrogen atom with its binding energy E_X given by

$$E_X = -\frac{1}{(4\pi\epsilon_0\epsilon_r)^2}\frac{\mu^* e^4}{2\hbar^2}\frac{1}{n^2}, \tag{2.12}$$

where $\mu^* = \left((m_e^*)^{-1} + (m_h^*)^{-1}\right)^{-1}$ is the reduced mass of the effective electron and hole masses. Using typical values for silicon ($\mu^* = 0.12 m_0$, $\epsilon_r = 12.1$) the binding energy of the $n = 1$ exciton is determined to be $\approx 11\,\mathrm{meV}$ and the associated Bohr radius amounts to $a_{B,X} \approx 5.3\,\mathrm{nm}$. This estimate reveals that excitons in silicon can be classified as Wannier excitons. This type of exciton is most often observed in covalent semiconductors and is characterized by an extend of the wave function over many unit cells, i.e., $a_{B,X} \gg a_0$[2]. Furthermore, if an exciton is said to be free, it can move through the crystal with a kinetic energy of

$$E_{kin,X} = \frac{\hbar^2 \mathbf{K}^2}{2\left(m_e^* + m_h^*\right)}, \tag{2.13}$$

where $\mathbf{K}$ is the momentum vector associated with the motion of the exciton mass center.

The spectroscopic footprint of free excitons strongly depends on the quality of the crystal and the existence of neutral impurities. The latter represent an attractive potential to the free exciton giving rise to the notion of bound excitons (BX) which can be regarded as a three particle complex consisting either of two holes and an electron, when bound to a neutral acceptor (A^0X), or two electrons and one hole, when bound to a neutral donor ($\mathrm{D^0X}$)[3]. Characteristics of those bound excitons in the emission spectrum are narrower linewidths due to the lack of kinetic energy and a redshift of the emission lines both compared to the free exciton emission. The existence of bound excitons was first observed experimentally by Haynes [37] who found that the localization energy E_L of the D^{0}X depends on the specific donor ground state energy E_D as

---

[2] In contrast, a Frenkel exciton is characterized by a large binding energy and $a_{B,X} \approx a_0$. They can be observed in, e.g., organic semiconductors.

[3] The possibility of forming an exciton bound to an ionized impurity, i.e., (A^-X) or (D^+X), is neglected since these complexes cannot exist in silicon [36].

$$E_L \cong 0.1 \times E_D, \tag{2.14}$$

which enabled the identification of a variety of shallow impurities in semiconductors. The recombination of D^{0}X in silicon is dominated by phonon-assisted emission lines due to the need for a wave vector conserving phonon. However, it is also possible that the short range central cell potential of the impurity scatters the electron towards the Brillouin zone center which results in the so called no-phonon transition investigated in this work.

The hyperfine interaction between the donor electron spin and the P nuclear spin (compare Eq. 2.8) together with the Zeeman splitting of the D^{0}X leads to a rich structure and distinct optical selection rules for the bound exciton which is displayed in Fig. 2.6. The bottom left hand side shows the evolution of the hyperfine-coupled D^0 ground state as a function of the magnetic field (compare Fig. 2.5). The D^0 state can be considered as the initial state of the transition D$^0 + h\nu \rightarrow$ D^{0}X. Therefore, the evolution of the D^0 state has to be taken into account as well as the evolution of the final state, i.e., the D^{0}X. The Zeeman splitting of the latter is governed by the hole spin only because the two electrons occupy a singlet state. If the external magnetic field is substantially larger than the hyperfine coupling constant, i.e. $\gamma_e B > A$, twelve dipole allowed transitions can be observed which is depicted on the right hand side of Fig. 2.6, where $m_h = 3/2$ denotes the heavy hole and $m_h = 1/2$ the light hole. It is worth noting, that these twelve transitions can also be considered as six doublets where the doublet splitting amounts to $\approx A/2$.

2.4 SPIN RELAXATION OF BOUND ELECTRONS IN SILICON

The process of spin relaxation can be defined in terms of the phenomenological Bloch equations [38] with an external magnetic field $\mathbf{B} = B_0\mathbf{z}$ oriented in z-direction:

$$\frac{\partial S_x}{\partial t} = \gamma\left(\mathbf{S}\times\mathbf{B}\right)_x - \frac{S_x}{T_2}, \tag{2.15}$$

$$\frac{\partial S_y}{\partial t} = \gamma\left(\mathbf{S}\times\mathbf{B}\right)_y - \frac{S_y}{T_2}, \tag{2.16}$$

$$\frac{\partial S_z}{\partial t} = \gamma\left(\mathbf{S}\times\mathbf{B}\right)_z - \frac{S_z - S_0}{T_1}, \tag{2.17}$$

where $\mathbf{S}$ is the (ensemble) spin polarization and S_0 is the equilibrium polarization in the direction of the magnetic field. The symbol T_2 is termed the spin dephasing time and determines the coherence of the spin precession in the x,y plane. On the other hand, T_1 is

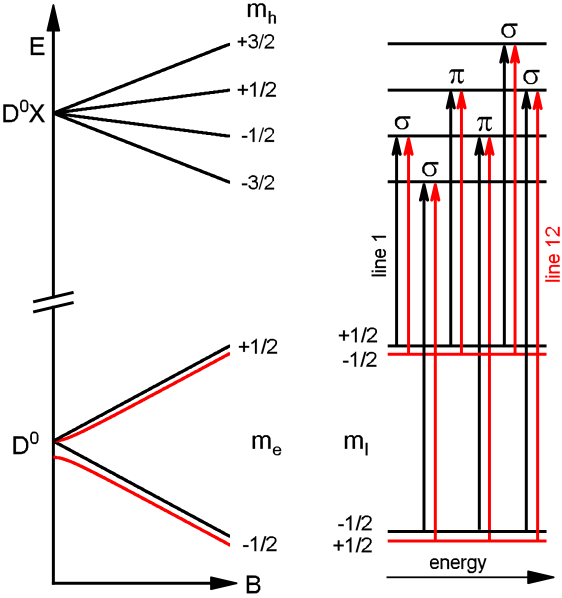

Figure 2.6: **(left)** Evolution of hyperfine-coupled donor states in an external magnetic field and the corresponding Zeeman shift of the D^0X. **(right)** Level diagram of the twelve dipole allowed transitions.

the longitudinal spin relaxation time and describes the return of the polarization along the direction of the magnetic field to its equilibrium value.

The temperature dependence of the spin relaxation rate for donor bound electron spins in silicon is given by the empirical formula[4] [39]

$$\frac{1}{T_1} = AT + BT^7 + CT^9 + DT^{13} + E_0 \exp\left(-\frac{\Delta}{k_B T}\right) \tag{2.18}$$

where the constants A to D contain known material constants like deformation potentials, velocities of sound, and E_0 is the Orbach constant[5]. The first term (AT) arises from emission or absorption of a single phonon with energy equal to the Zeeman splitting of the donor ground state [9]. This causes the electron spin to flip from $|\uparrow\rangle$ to $|\downarrow\rangle$ or vice versa. The terms B to D arise from a Raman process where a phonon is scattered from state q to a state q' while the donor electron spin flips. The T^7 term comes from anisotropic magnetic interaction [8], the T^9 term is caused by spin orbit interaction [39], and the T^{13} term is obtained by only considering dilatational deformations [7]. The most important relaxation mechanism in this work (compare chapter 10.2) is the exponential term in Eq. 2.18 which can be attributed to Orbach spin lattice relaxation where Δ is the level spacing between the A_1 donor ground state and the T_2 excited state (compare chapter 2.2). Despite the fact that the exact theoretical treatment of the Orbach process in silicon is rather intricate (see Ref. [31]) an intuitive simplified picture is straightforward.

Consider a $|\uparrow\rangle$ electron in the A_1 donor ground state. Thermal excitation provides fractional occupation of the T_2 states according to $\exp(-\Delta/k_B T)$. The key to spin relaxation is that the T_2 state is a mixed spin state $|\uparrow\downarrow\rangle$. Therefore, the T_2 electron originating from the A_1 $|\uparrow\rangle$ state may also relax back to the A_1 $|\downarrow\rangle$ state. The numerical value of the Orbach constant E_0 can be obtained from electron spin resonance experiments in ^{28}Si by fitting the experimentally determined spin lattice relaxation rate [17] with

$$\frac{1}{T_1} = E_0 \exp\left(-\frac{\Delta}{k_B T}\right). \tag{2.19}$$

---

[4] The magnetic field dependence of the A and B contribution is neglected since it is only observed for magnetic fields $> 800\,\mathrm{mT}$. The magnetic fields applied in this work never exceed $100\,\mathrm{mT}$.

[5] In Ref. [39] the exponential dependence in Eq. 2.18 is not attributed to the Orbach process since it was not known at that time.

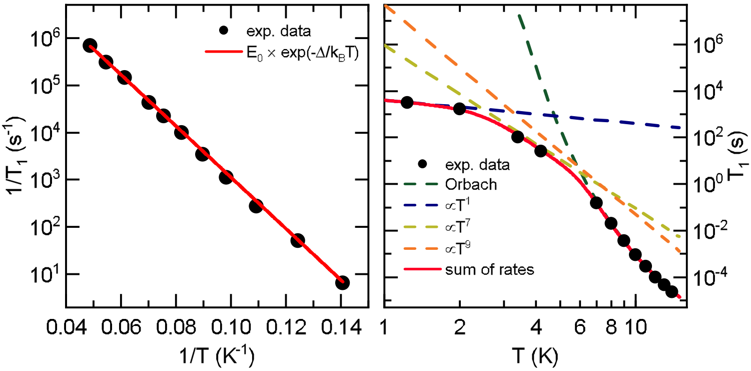

Figure 2.7: **(left)** Experimental spin relaxation data of donor electron spins in ^{28}Si. The red line is a fit which determines the Orbach constant E_0. Adapted from [17]. **(right)** Experimental spin relaxation data on a wider temperature scale. The red line denotes the sum of all relaxation processes. The different contributions (dashed lines) are explained in the main text. Adapted from [22].

This is shown in an Arrhenius plot in Fig. 2.7 (left) where the temperature range has been chosen such that the Orbach relaxation is the dominating mechanism. Therefore, an unambiguous value of $E_0 = 3 \times 10^8\,\mathrm{s}^{-1}$ can be extracted which should hold for all P doping concentrations $\leq 1 \times 10^{16}\,\mathrm{cm}^{-3}$ according to Ref. [17]. The right hand side of Fig. 2.7 shows experimental T_1 times [22] also for lower temperatures where the single phonon and Raman processes dominate. The red line is a cumulative fit to the experimental data containing the linear relaxation term, the T^7 and T^9 contribution as well as Orbach relaxation with the previously determined E_0. The dashed colored lines represent the individual contributions to the spin relaxation process.

Part II

EXPERIMENTAL METHODS

ABSTRACT PART II

This part describes the experimental setup used in this work and its most important components, i.e., the external cavity diode laser, the electro-optic modulator and the cryostat. The implementation of phase modulation absorption spectroscopy is the key methodology in this work. Quantitative calculations with respect to the modulation frequency show the advantages as well as the pitfalls of this method when a quantitative line shape analysis is desired. Furthermore, a home-built helium reservoir is introduced which allows for absolutely strain-free mounting of the sample while maintaining excellent thermal contact to the cold finger of the cryogen-free closed cycle refrigerator.

3

EXPERIMENTAL SETUP

3.1 IMPORTANT COMPONENTS

3.1.1 *External Cavity Diode Laser*

The working principle of a tunable external cavity diode laser (ECDL) is based on the interplay of two cavities. A very common geometry in this context is the Littrow configuration which is also applied in the lasers used in this work[1]. A schematic diagram of a Littrow laser is shown in Fig. 3.1 [40]. It consists of a laser diode where the inward facets exhibit a finite reflectivity R and act as the first (internal) cavity with the small length L_D. The emitted laser light is collimated by a lens and directed onto a diffraction grating where the angle Θ matches the angle of the first order reflected beam which is directed back into the laser diode. This forms the second cavity with the larger length L_{ext}. In this configuration, the wavelength selection is accomplished by a piezo actuator at the

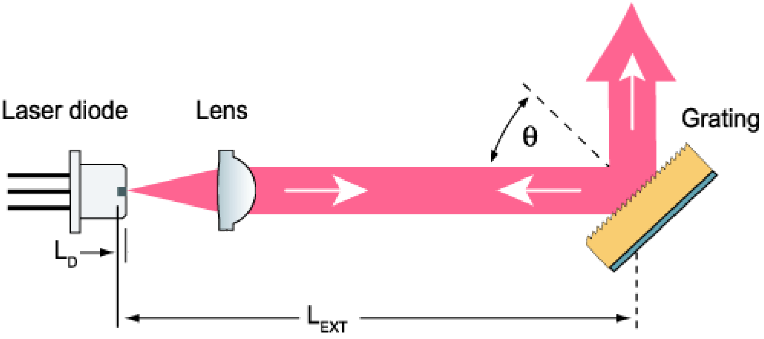

Figure 3.1: Schematic illustration of an external cavity diode laser in Littrow geometry. Adapted from [40].

---

[1] The second common geometry is termed Littmann geometry. Here, the first order diffracted beam is not directly reflected back into the diode but on a mirror instead. This offers wavelength selection by a rotation of the mirror instead of the grating with a slightly narrower linewidth but less output power when compared to the Littrow configuration.

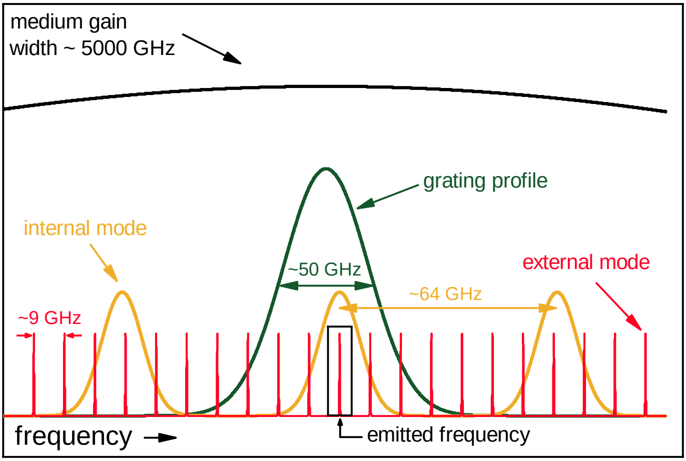

Figure 3.2: Illustration of the interplay between the different cavity modes in an ECDL. Adapted from [41].

back of the grating which changes Θ. From this simple geometry it is evident that in order to work properly the optical feedback from the grating into the laser diode has to be aligned perfectly. This can be done by setting the laser diode current just below the operation threshold where no lasing is observed. The position and angle of the grating is then adjusted until lasing sets on again and the output power is maximized. After that, the diode current is again reduced below the laser threshold and the procedure is repeated until no further reduction of the threshold current is possible. The benefit of relatively narrow laser linewidth ($\leq 1\,\mathrm{MHz}$) of these lasers stems from the interplay between the two cavities and the grating profile which is outlined in Fig. 3.2 for the commercial ECDL (Toptica DL 100) [41]. The cavity inside the laser diode with small length L_D and low reflectivity results in the orange spectrum with a certain width given by the reflectivity of the laser diode's facets and a spacing proportional to L_D^{-1}. On the other hand, the external cavity (red line) exhibits a narrowly spaced ($L_{ext} > L_D$) mode spectrum with sharp peaks. The key to stable operation lies in the mutual maximum overlap between the grating profile (green line), the internal mode, and one external mode which determines the emitted frequency (black box). Achieving the optimal overlap is impeded by the fact that the particular modes behave differently upon temperature and diode current, i.e., both will affect the laser power and laser frequency differently.

3.1.2 *Electro-Optic Modulator*

The electro-optic modulator (EOM) is one of the most frequently used devices in this work and plays a crucial role for laser stabilization via the Pound-Drever-Hall technique (compare chapter 5.5) and for the optical spectroscopy of donor bound excitons in $^{28}\mathrm{Si}:\mathrm{P}$ as presented in parts IV and V. The working principle of the EOM relies on the Pockels effect which describes the birefringence in a medium evoked by an electric field [42]. This work utilizes a fiber based EOM[2] (cf. Fig. 3.3) made from $\mathrm{LiNbO_3}$ designed for wavelengths of $\lambda = 1064(60)\,\mathrm{nm}$.
A common figure of merit is the half-wave voltage U_π, i.e., the voltage required to produce a phase shift of π. The half-wave voltage is given by [43]

$$U_\pi = -\frac{\lambda g}{n_3^3 r_{33} L \Gamma_{eff}}, \tag{3.1}$$

where r_{33} is the relevant entry of the electro-optic tensor, n_3 is the refractive index along the applied electric field, and Γ_{eff}

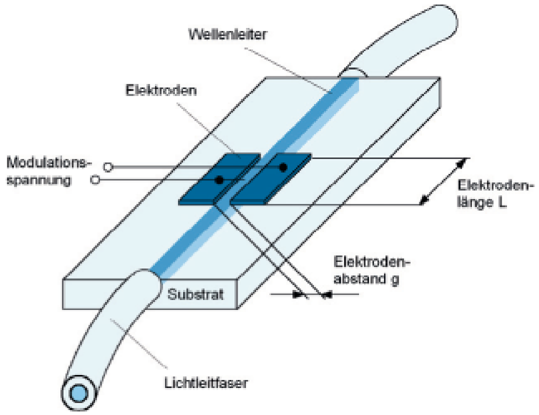

Figure 3.3: Schematic diagram of a fiber-based EOM. Taken from [43].

---

[2] JenOptik PM-1064

is the internal efficiency. The main advantage of a fiber-based EOM compared to a free space EOM is the small dimension of the electrode spacing g while maintaining a relatively long electrode length L. This results in $U_\pi \approx 10\,\mathrm{V}$ which is easily achievable without the need for a high voltage amplifier and thus entails fast modulation up to 5 GHz.

3.1.3 *Cryostat*

The cryostat used in this work is a cryogen-free, two stage pulse tube refrigerator from Oxford instruments (Triton 400) with an additional circuit for condensing and circulation of a ^{3}He/^{4}He mixture. The latter allows the system to reach a base temperature of $T < 50\,\mathrm{mK}$. The working principle of the pulse tube refrigeration is essentially the same as a (inverse) Sterling engine where the temperature difference between two connected gas reservoirs is used to do mechanical work by raising and lowering top-hats. Here, mechanical work is required to compress the working gas (helium) which is adiabatically expanded in the cold head of the cryostat. Further details on the working principle can be found in Refs. [44, 45]. Since this mechanism does not "consume" helium, it allows for continuous long term operation up to six month where a full cooldown takes ≈ 24 h and ends in this case in a temperature of ≈ 3.8 K. This mode of operation is sufficient for most of the experiments carried out in this work where the temperature can be stabilized with an accuracy of ±2 mK in a temperature window between 4 K and 6 K. If lower temperatures are desired (compare chapter 7.3), the ^{3}He/^{4}He mixture has to be condensed into the mixing chamber. Furthermore, the cryostat is equipped with three mutually orthogonal superconducting magnets in Helmholtz geometry providing 2 T in the direction of light propagation and 200 mT in each of the orthogonal directions.

3.2 OPTICAL SETUP

A block diagram of the optical setup is shown in Fig. 3.4 where the black solid lines represent electrical connections and the green solid lines stand for optical fibers. Furthermore, the setup can be divided into two parts. The first part is a classical phase modulation absorption spectroscopy setup (compare chapter 4) where an external cavity diode laser (Toptica DL 100) serves as excitation source (ECDL probe). The wavelength of the laser is stabilized and controlled by a high precision wavelength meter (HighFinesse WSU-2) which provides a relative accuracy of 500 kHz. In order to perform phase modulation spectroscopy, the laser is passed through

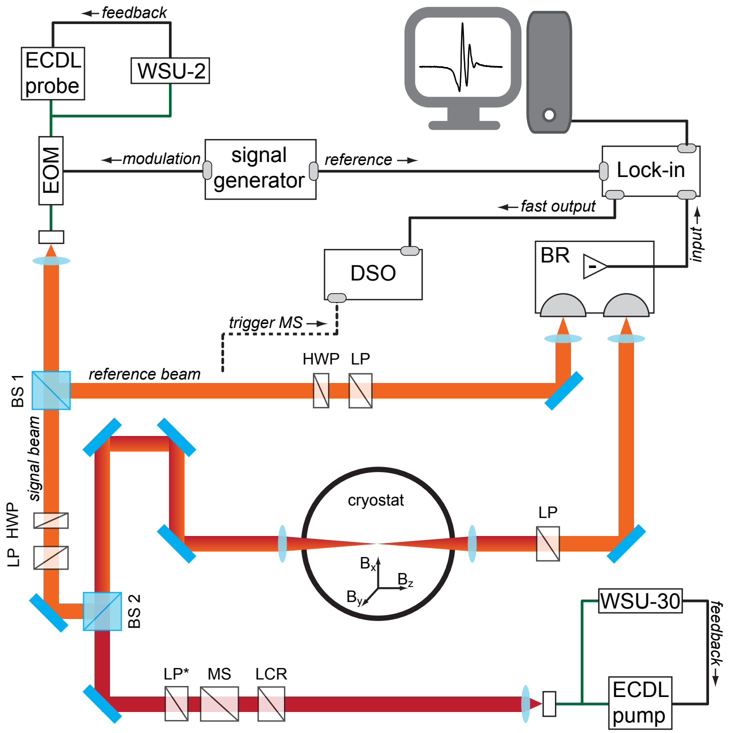
feedback
ECDL probe
WSU-2
EOM
modulation
signal generator
reference
Lock-in
fast output
input
DSO
BR
trigger MS
HWP
LP
reference beam
BS 1
signal beam
LP
HWP
cryostat
B_x
B_z
B_y
LP
BS 2
WSU-30
feedback
ECDL pump
LP*
MS
LCR

Figure 3.4: Block diagram of the optical setup. The acronyms are explained in the main text.

a fiber-based EOM (JenOptik PM-1064) which is usually[3] driven by a low frequency function generator (Agilent 33210A). After passing the EOM, the beam is split by a 50/50 beam splitter (BS1) into the signal beam which is focused onto the sample by a $f = 30\,\mathrm{cm}$ plano-convex lens and the reference beam which is used to compensate the DC part of the signal beam on the balanced photo receiver (BR - Femto OE300). The combination between the rotatable have-wave plate (HWP) and the linear polarizer (LP) is used to adjust the optical power. The output of the BR is fed into the lock-in amplifier (Stanford Research SR844) which derives its frequency reference from the signal generator. Data acquisition from the lock-in amplifier takes place via a personal computer.

The second part of the setup incorporates the use of a second ECDL (ECDL pump) which is stabilized by another wavelength meter (HighFinesse WSU-30) and serves as the pump laser for the experiments presented in chapter 10. The pump beam is passed through a liquid crystal retarder (Meadowlark LRC-200) which basically acts as a voltage controlled variable-wave plate. In the context of the experiments performed in this work[4] the LCR is used as a half-wave plate to rotate the polarization by 90° in order to coincide with the axis of the LP* which is orthogonal to all other LPs in the setup. The pump and the probe beam are brought together on BS2 and the LP after the cryostat blocks the pump beam. In order to employ time resolved spectroscopy, a mechanical shutter (MS - Thorlabs SH05/M) is placed in the pump beam's path. In this case, the signal is acquired by connecting the fast output of the lock-in amplifier to a digital storage oscilloscope (DSO) which is triggered by the same signal used to periodically switch the MS.

---

[3] The experiments at the beginning of chapter 9 are carried out with a high frequency function generator (Rhode Schwarz SML)

[4] In future experiments, the LCR may also be used to generate circularly polarized light in order to demonstrate optical spin injection (compare chapter 11.2). In this case, LP* has to be omitted.

3.3 HOME-BUILT HELIUM RESERVOIR

The use of a cryogen-free pulse tube refrigerator certainly yields the benefit of very long measurement times compared to, e.g., a helium bath cryostat where the measurement time is limited by the size of the liquid reservoir and the helium consumption. However, a bath cryostat provides excellent thermal coupling to the sample because it is directly immersed in liquid helium for $T \leq 4.2\,\mathrm{K}$ or surrounded by helium gas for $T > 4.2\,\mathrm{K}$. In a cryogen-free refrigerator, the coupling between the thermal reservoir and the sample is accomplished by contacting the sample to the cold finger of the cryostat which is usually made from gold-plated copper. This contact can either be made by the use of a low temperature contact agent such as silver paint or Apiezon N grease or mechanically by clamping the sample to the cold finger. Both methods will lead to inevitable internal strain in the sample due to the difference in the coefficients of thermal expansion of the materials which manifests itself during the cooldown. When dealing with donor bound excitons in GaAs this effect generally does not play a big role because the transition is inhomogeneously broadened with a spectral width of $\approx 50\,\mathrm{GHz}$ even for nominally undoped samples [46]. With their ultra narrow linewidth of $\approx 100\,\mathrm{MHz}$, donor bound exciton transitions in ^{28}Si are significantly more sensitive to strain. Yang et al. [47] have examined the optical properties of MBE grown ^{28}Si enriched to 99.9 % on natural silicon ^{nat}Si. They find a rather pronounced splitting in the spectrum of the D^0X transitions of $\approx 4.4\,\mathrm{GHz}$ which is related to the slight mismatch in the lattice constants a_{28} and a_{nat}. The fractional lattice parameter difference amounts to

$$\frac{\Delta a}{a} \equiv \left| \frac{a_{nat} - a_{28}}{a_{nat}} \right| \approx 2.8 \times 10^{-6}. \tag{3.2}$$

To put this number into context we consider the lattice parameters of GaAs and AlAs with $a_{GaAs} = 5.6533\,\text{Å}$ and $a_{AlAs} = 5.6611\,\text{Å}$ [48]. These two binary semiconductors are generally said to be lattice matched with

$$\left(\frac{\Delta a}{a}\right)_{GaAs,AlAs} \approx 1.4 \times 10^{-3}. \tag{3.3}$$

This is three orders of magnitude larger than the lattice mismatch causing the spectral shift observed in Ref. [47]. Therefore, it is evident that the unperturbed observation of D^0X transitions in ^{28}Si prohibits the use of a low temperature contact agent and any kind of clamping. To ensure strain-free mounting of the sample without the loss of thermal coupling to the cold finger of the cryostat, a sample rod with attachable helium reservoir with optical access has been designed. Fig. 3.5 (top) shows CAD drawings of the construction. The construction consists of a gold-plated copper rod (a) which can be mounted to the cold plate of the cryostat via the top plate (b). The drilling (c) provides access to the actual sample chamber (d) which is the heart of the construction. The bottom of Fig. 3.5 shows a close-up view of the sample chamber which is made from a beryllium-copper alloy[5]. The connection (e) between the sample rod and the chamber is properly sealed with indium wire and the construction is held together by brass screws inside the mounting holes (f). The choice of brass as material for the screws results from the fact that the coefficient of thermal expansion for brass is larger than for beryllium-copper. In this way the connection further tightens upon cooldown of the cryostat. The protrusion (g) serves as a holder for the optical windows (not shown) which are radially glued in by a two component epoxy[6]. The small thickness of the protrusion of only 100 µm reduces potential birefringence of the fused silica windows due to the different CTEs of the joint materials which is of high importance in polarization-sensitive experiments. The sample (i) itself resides absolutely strain-free in a basin made from Macor [7] which, in turn, resides in a bigger basin made from copper where the latter is connected to the sample rod by brass screws. It is of great importance that all connections are made with highest care because the helium molecule is prone to even the smallest leak. Therefore, the whole construction is put to extensive leakage tests prior to cool down. The leakage detector essentially consists of a vacuum pump attached to a mass spectrometer sensitive to helium. In order to check for leaks, the chamber is evacuated by the leakage tester and a hose with pressurized helium is manually placed at the delicate connections. The construction is defined to be tight when the reading of the leakage detector does not exceed its noise floor of $2 \times 10^{-9}\,\mathrm{mbar\,L\,s^{-1}}$. After that, the chamber is flooded with helium at room temperature and a pressure of 1.5 bar – 2 bar. This concept has proven to work extremely well if the cryostat temperature stays well above $T_\Lambda = 2.1\,\mathrm{K}$, i.e., the temperature at which the phase of ^4He changes from the liquid to the superfluid state. Especially the temperature of the phase transition seems very critical. At exactly T_λ, it has been observed several times that the helium instantly leaves the sample chamber which is accompanied by a drastic increase in the cryostat's outer vacuum chamber (OVC) reading. The origin of this behavior is not fully understood since the notion of superfluid leaks [44] is very vague.

---

[5] Also another chamber, built from titanium, have been fabricated. Although not used in this work, it provides interesting possibilities for measurements where the earth's magnetic field needs to be suppressed. This is possible because titanium becomes superconducting below $\approx 500\,\mathrm{mK}$.

[6] Araldite 2011

[7] machinable ceramic, developed by Corning Inc.

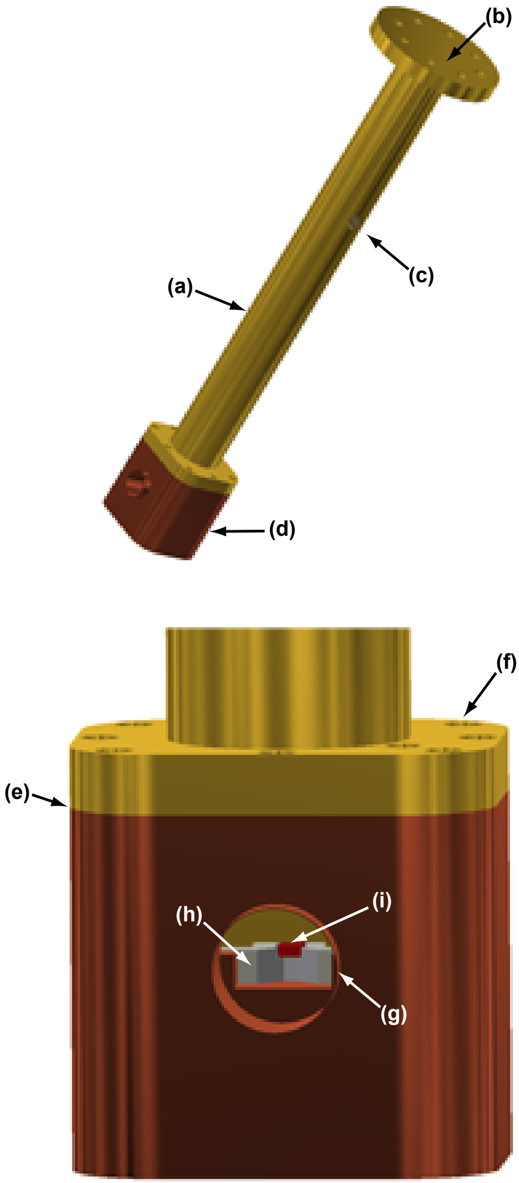

Figure 3.5: **(top)** CAD drawing of the fully assembled sample rod. **(bottom)** Close-up view of the sample chamber. For details, see main text.

4

PHASE MODULATION SPECTROSCOPY

Sophisticated modulation techniques can be employed to improve the signal to noise ratio of weak signals in an optical spectroscopy experiment [49, 50]. The laser light at frequency ω and phase ϕ is considered as a plane wave in the time domain

$$E(t) = E_0 \exp\left(i\left(\omega t + \phi\right)\right). \tag{4.1}$$

Here, the phase of the light is periodically modulated at frequency Ω by a fiber-based EOM which yields [51]

$$\begin{aligned} E(t) &= E_0 \exp\left[i\left(\omega t + M \sin\left(\Omega t\right)\right)\right] && (4.2) \\ &= E_0 \exp\left(i\omega t\right) \sum_{n=-\infty}^{+\infty} J_n(M) \exp\left(in\Omega t\right), && (4.3) \end{aligned}$$

where J_n is the nth order Bessel function and M is the modulation index which is proportional to both the imprinted phase shift and the applied modulation voltage at the EOM. The structure of Eq. 4.3 directly reveals that the laser light has acquired additional spectral components at $\omega \pm n\Omega$. These additional components are termed the nth sidebands and the original spectral component (n = 0) at ω is called the carrier. Fig. 4.1 displays the intensity $I \propto |E|^2$ of the modulated laser beam for $n = 0, 1, 2$ as a function of the phase shift. If the phase shift or modulation index is sufficiently small, the spectral components of the laser light mainly consist of the carrier and the first sideband which is illustrated in the inset of Fig. 4.1. The opposite vertical orientation of the negative and positive sidebands at $\omega \pm \Omega$ indicate a phase difference of π. In order to be useful for optical spectroscopy, the modulated laser has to interact with a sample containing an absorption line of spectral width Γ_0. This interaction is modeled by a complex transmission function

$$T(\omega_n) = \exp(-\delta_n - i\Phi_n), \tag{4.4}$$

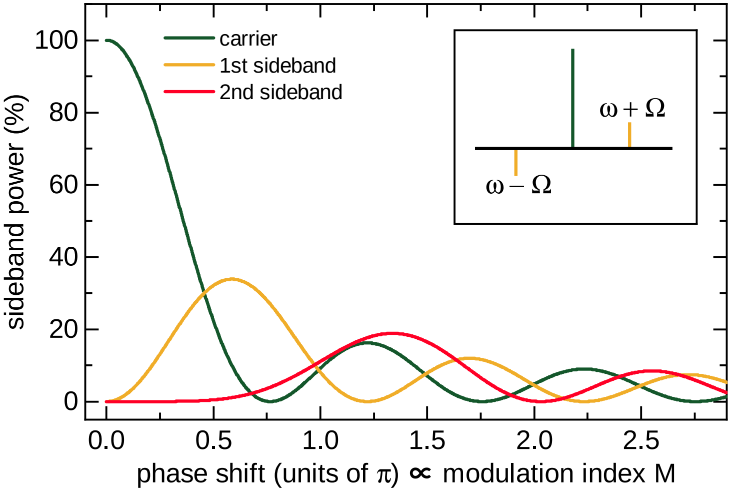

Figure 4.1: Sideband power of a phase modulated laser beam as a function of the phase shift. The inset shows the phase relation between the carrier and the first sidebands.

where ω_n denotes the optical frequency of the nth sideband, δ_n is the corresponding field amplitude attenuation, and Φ_n is the optical phase shift. The transmitted electric field $E_T(t)$ now reads

$$E_T(t) = E_0 \exp\left(i\omega t\right) \sum_{n=-\infty}^{+\infty} T(\omega_n) J_n(M) \exp\left(in\Omega t\right). \quad (4.5)$$

The sidebands of order $n > 1$ can be neglected in the present case of small M. Using $J_0(M) \approx 1$ and $J_1(M) \approx M/2$, the transmitted intensity I_T reads

$$I_T = \left|E^2(t)\right| \propto E_0^2 \exp(-2\delta_0)\left[1 + M\left(\delta_{-1} - \delta_1\right)\cos\left(\Omega t\right)\right], \quad (4.6)$$

where the terms containing the optical phase shift Φ_n have been neglected. An inspection of the terms oscillating at $\cos\left(\Omega t\right)$ reveals that the transmitted intensity contains the difference $\delta_{-1} - \delta_1$ which is nothing else but the absorption difference between the negative sideband at $\omega - \Omega$ and the positive sideband at $\omega + \Omega$. This difference signal is easily retrieved by standard lock-in detection at the modulation frequency Ω and yields in very good approximation the derivative of the spectral absorption profile provided the modulation frequency is small compared to the spectral width of the transition,

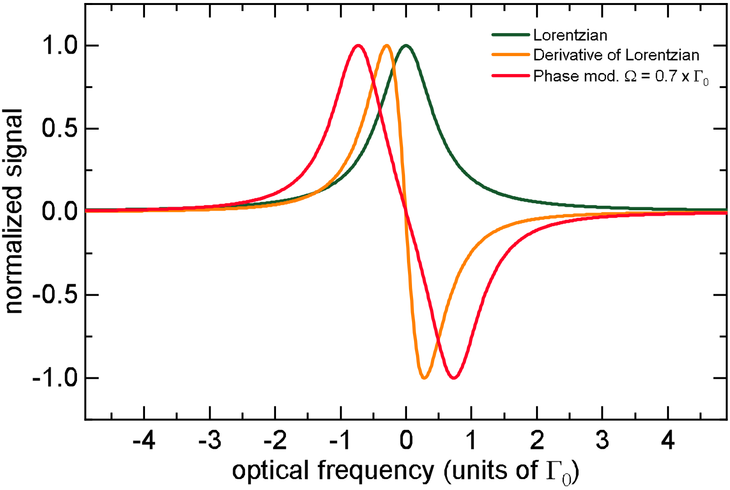

Figure 4.2: Illustration of the phase modulation technique depicting a Lorentzian absorption profile (dark green line) with an FWHM of Γ_0. The orange line is the derivative of the absorption profile and the red line is a simulated phase modulation signal with $\Omega = 0.7 \times \Gamma_0$.

i.e. $\Omega \ll \Gamma_0$. Figure 4.2 shows the output of such a phase-modulated scan across a Lorentzian transition (dark green line) with FHWM of Γ_0. In the case of $\Omega \ll \Gamma_0$, the shape of the phase modulation signal approaches the shape of the absorption profile derivative (orange line). However, if the modulation frequency is comparable to the linewidth the phase modulation signal considerably deviates from the derivative. This is demonstrated by the red line where $\Omega = 0.7 \times \Gamma_0$. In an experiment, it is highly desirable to keep the modulation frequency Ω well below the transition linewidth Γ_0 in order to measure an excellent approximation to the real derivative of the absorption profile. This bears the advantage that the acquired data can be integrated numerically in the post processing which yields the true absorption profile without the need of correcting for artifacts caused by large modulation frequencies. A first measure for the optimum value of Ω is the squared residuum χ^2 between

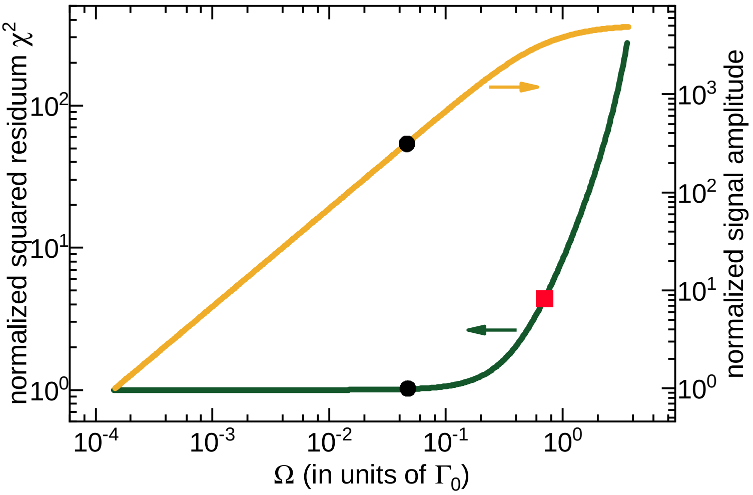

Figure 4.3: **(left - green line)** normalized squared residuum illustrating the influence of Ω on the lineshape of the phase modulation signal. **(right - orange line)** normalized signal amplitude illustrating the influence of Ω on the amplitude of the phase modulation signal.

the phase modulation signal and the actual derivative absorption profile. This is defined as:

$$\chi^2 = \sum_{\nu=-\infty}^{\infty} \left[S_L(\nu) - S_M(\nu, \Omega)\right]^2 , \tag{4.7}$$

where ν is the optical frequency, $S_L(\nu)$ is the derivative of the absorption line profile, and $S_M(\nu, \Omega)$ is the phase modulation signal. In Fig. 4.3, the normalized calculated values for χ^2 as a function of Ω is shown as green solid line. The normalization is such that $\chi^2 = 1$ results in perfect agreement between $S_L(\nu)$ and $S_M(\nu, \Omega)$. The red square indicates the residuum of the phase modulation signal in Fig. 4.2. As a rule of thumb we can derive that the modulation frequency Ω needs to be well below $0.1 \times \Gamma_0$ in order to extract the undisturbed lineshape. On the other hand, electric noise of, e.g., the photo detector, sets a certain lower boundary for Ω since the strength of the phase modulation signal is proportional to Ω [1].

---

[1] The proportionality is well defined for $\Omega \ll \Gamma_0$. For $\Omega \approx \Gamma_0$ the signal amplitude saturates

This is shown by the plot of the phase modulation signal amplitude (orange line) in Fig. 4.3 where the amplitude is normalized to the lowest considered value of Ω. This clearly demonstrates that the choice of Ω is a compromise between the need for sufficient signal strength and the desire of an unperturbed lineshape. If not stated differently, we use $\Omega = 0.045 \times \Gamma_0$ (black dots in Fig. 4.3) throughout this work.

Part III

A HIGH STABILITY DIODE LASER FOR SPECTROSCOPY OF ULTRA LOW DOPED SILICON

ABSTRACT PART III

The optical linewidth of defect-bound excitons in ultra low doped and isotopically enriched silicon approaches the natural transform limited linewidth of some 100 kHz. Here, external cavity diode lasers provide an ideal tool for studying these optical transitions. However, the inherent frequency fluctuations of the commercial Toptica diode laser range on the same scale like the optical linewidth and thus need to be reduced. In order to obtain unambiguous spectral resolution, we have designed a high finesse optical cavity made from ultra low expansion glass and thus suitable for frequency stabilization via Pound-Drever-Hall locking. A considerable part of information regarding the technical design of the cavity assembly and the temperature stability can be found in Ref. [52].
In this part, the focus lies on the extraction of important cavity parameters and especially on the system's effective zero crossing temperature T_0. Supported by detailed numerical simulations we experimentally determine $T_0 = 19(3)\,°\mathrm{C}$.

Furthermore, a frequency domain analysis of the Pound-Drever-Hall error signal shows that the laser noise power spectral density can be significantly reduced which yields a frequency stability of $\approx 4\,\mathrm{kHz}$ on a 1 s timescale. The table below shows a summary of important parameters of the self-built reference cavity.

PARAMETER	SYMBOL	VALUE
finesse	$\mathcal{F}$	$26(5) \times 10^3$
free spectral range	Δ_{FSR}	1.362 GHz
zero crossing temperature	T_0	19(3) °C
frequency stability	$\Delta\nu_{rms,\mathrm{LOCKED}}$	4 kHz

5

CAVITY FUNDAMENTALS AND DESIGN

5.1 THE FABRY PEROT CAVITY

A Fabry Perot cavity (FPC) consists of two partly reflecting mirrors with reflectivity R, which are separated by a spacer of length L. Due to the condition of constructive interference for the traveling light field inside the cavity, the optical frequencies are restricted to discrete values:

$$\nu_q = q\frac{c}{2nL} = q\Delta_{FSR} \qquad q = 1, 2, ..., \tag{5.1}$$

where n is the refractive index of the medium between the mirrors and Δ_{FSR} denotes the free spectral range of the cavity.

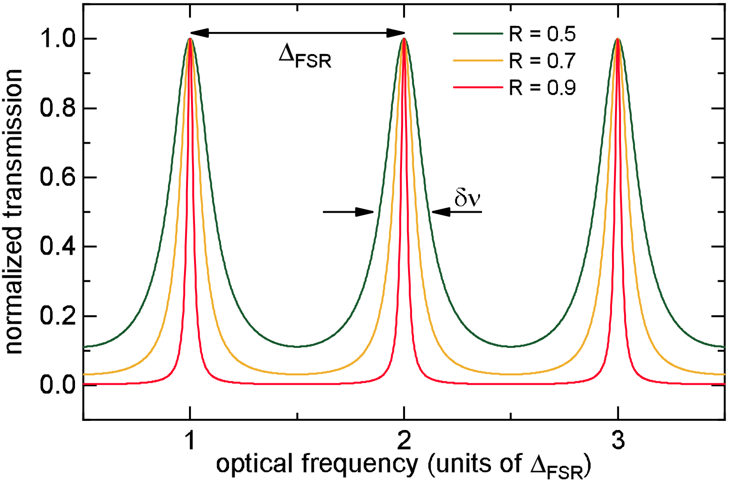

Figure 5.1: Normalized transmission spectrum of a Fabry Perot cavity for mirror reflectivities of 0.5 (green line), 0.7 (orange line) and 0.9 (red line). The frequency axis is normalized to the free spectral range (Δ_{FSR}).

Figure 5.1 illustrates, for different mirror reflectivities R, the transmission spectrum $I(\nu)$ of a FPC which is given by [53]

$$I(\nu) = \frac{(1-R^2)}{1+(2\mathcal{F}/\pi)^2\, sin^2\,(2\pi\nu nL/c)}, \tag{5.2}$$

where the Finesse $\mathcal{F}$ is defined as

$$\mathcal{F} = \frac{\pi\sqrt{R}}{1-R} = \frac{\delta\nu}{\Delta_{FSR}} \tag{5.3}$$

and $\delta\nu$ is the width of the transmission maximum.

5.2 CAVITY DESIGN CONSIDERATIONS

Laser frequency stabilization to a FPC relies on the insensibility of the resonator reference frequency to external perturbations such as temperature fluctuations. The relative change of the resonance frequency ν in a FPC is directly related to the spacer length L. From Eq. 5.1 it directly follows that

$$\frac{d\nu}{\nu} = -\frac{dL}{L}. \tag{5.4}$$

Therefore, the frequency stability of the laser is related to the thermal expansion

$$dL = L\alpha(T)dT \tag{5.5}$$

of the cavity spacer, where $\alpha(T)$ is the temperature dependent coefficient of thermal expansion (CTE). A desired absolute frequency stability of 1 kHz excludes all common, easily machinable materials for the cavity spacer, because the CTE of those materials is on the order of $10 \times 10^{-6}\,\mathrm{K}^{-1}$ and thus requires an absolute temperature stability below 1 µK which is a hardly achievable condition in an optical laboratory. This condition is relaxed by the beneficial properties of Ultra Low Expansion glass (ULE) manufactured by Corning. In the vicinity of the zero crossing temperature T_0, where the CTE vanishes, the thermal expansion coefficient can be expressed as [54]:

$$\alpha_{ULE} = a(T-T_0) \quad \text{with} \quad a = 2.4 \times 10^{-9}\,\mathrm{K}^{-2}. \tag{5.6}$$

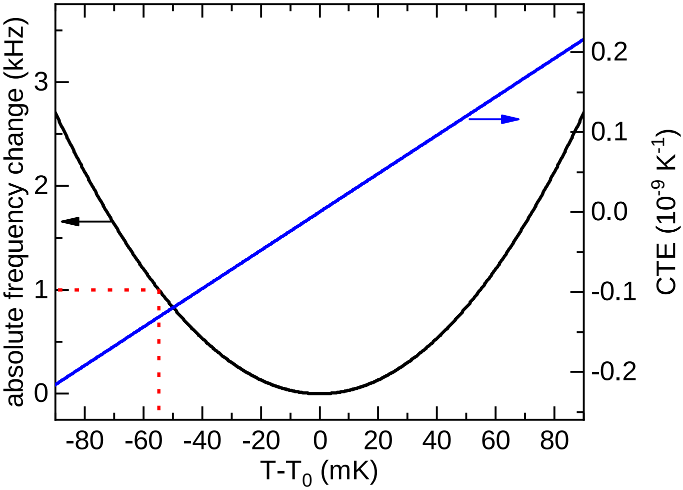

Figure 5.2: Calculated linear CTE of ULE (right axis) and the resulting quadratic frequency change according to Eq. 5.4/5.5 (left axis) as a function of detuning from the zero crossing temperature.

Figure 5.2 shows the calculated coefficient of thermal expansion for ULE as a function of temperature detuning away from T_0 (right axis - blue line) and the resulting quadratic dependence of absolute optical frequency change (left axis - black line). The previously demanded frequency stability of 1 kHz is now well within reach of laboratory temperature conditions as indicated by the dashed red line.

5.3 FEM SIMULATION

The zero crossing temperature T_0 of ULE is usually specified to lie in the temperature range between 20 °C and 30 °C. However, the relatively high CTE of the two, optically contacted, fused silica (FS) mirrors tend to shift the zero crossing temperature of the combined material cavity towards significantly lower temperatures. This problem has been addressed by Legero et al. [54]. They have shown by means of finite element simulations (FEM) and high precision measurements that the shift of the zero crossing temperature can be substantially reduced if an additional ring made from ULE is contacted on top of each FS mirror.

For a perfectly rigid optical contact, a small temperature change dT will only lead to a difference in radial expansion between the spacer and the mirror expressed by

$$dR = \left(\alpha_{FS} - \alpha_{ULE}\right) R\, dT, \tag{5.7}$$

where R is the radius of the mirror. A change of the cavity length is only caused by axial displacement dB which is related to the radial expansion by a dimensionless coupling coefficient δ such that $dB = \delta dR$. The effective CTE of the combined cavity can now be described in terms of the coupling coefficient δ, the mirror radius R, and the spacer length L such that $dL_{eff} = L_{eff}\alpha_{eff}dT$ with

$$\alpha_{eff}\left(T\right) = \alpha_{ULE}\left(T\right) + 2\delta\frac{R}{L}\left[\alpha_{FS}\left(T\right) - \alpha_{ULE}\left(T\right)\right]. \tag{5.8}$$

We use the commercial FEM package COMSOL Multiphysics installed on the local university computation facility to simulate the effective displacement of the inward mirror center point for different temperature steps away from the nominal zero crossing temperature.

The effect of the additional ULE ring is demonstrated in Fig. 5.3. The top left shows a magnified, color-coded plot of the axial displacement without an additional ULE ring for a temperature step of 1 K away from the nominal zero crossing temperature. The bulging of the FS mirror due to difference in radial expansion is clearly visible. Furthermore, the axial mirror displacement along the inward diameter (bottom left) shows a maximum axial displacement of ≈ 2.5 nm at the center of the mirror. This situation changes when an additional ULE ring is contacted on top of the FS mirror (Fig. 5.3 right side). Here, the bulging of the mirror is clearly reduced. Most importantly, the axial displacement at the center of the mirror is close to zero which indicates that the effective zero crossing temperature is close to the nominal ULE zero crossing temperature for this particular ring geometry (inner bore diameter 8 mm, thickness $h = 7$ mm).

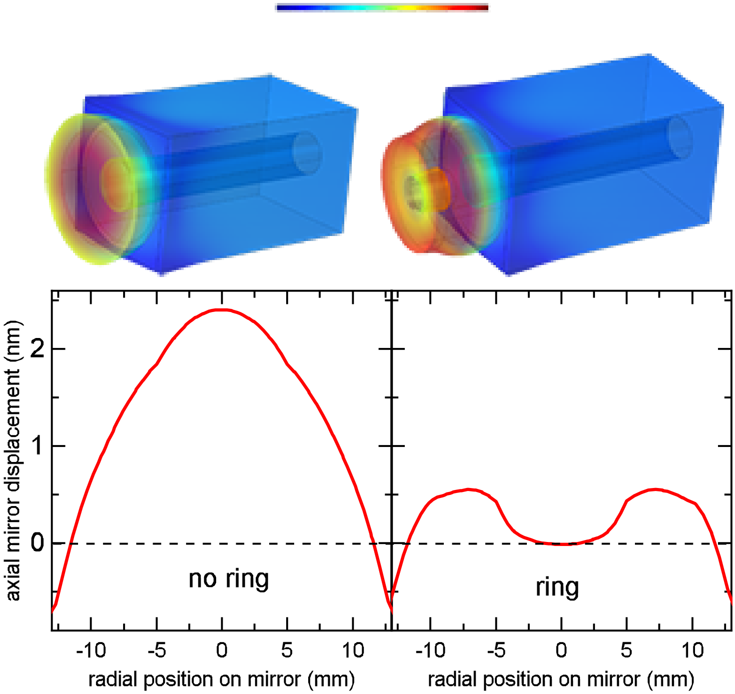

Figure 5.3: **(left)** FEM simulation results for a cavity without ULE ring. **(right)**FEM simulation results with an additional ULE ring (bore diameter = 8 mm, thickness $h = 7$ mm).

In order to find the optimal ring geometry for the present cavity design we have simulated all possible combinations of the ring's inner bore diameter and the ring thickness h for different temperature steps. For each configuration, the effective length change at the inward mirror center is extracted. A fit to the calculated length change with Eq. 5.8 reveals the coupling coefficient δ and thus the effective zero crossing temperature of the combined material cavity. An exemplary result is shown in Fig. 5.4. For a fixed inner bore diameter of 8 mm the ring thickness is varied and the coupling coefficient δ is extracted. The lowest value of δ is found for a ring thickness of 7 mm which results in a calculated shift of the zero crossing temperature of only -3 K. The practical importance of the additional ULE ring is clearly demonstrated for the case $h = 0$ mm

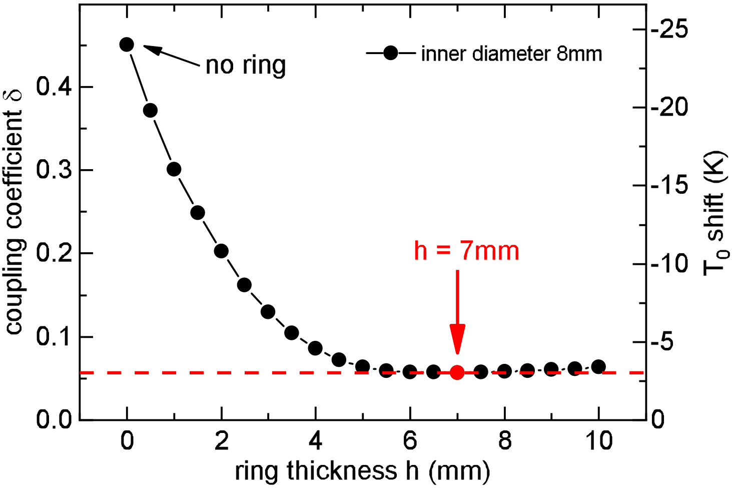

Figure 5.4: Calculated coupling coefficients δ for different ULE ring thickness. The corresponding zero crossing temperature shift is indicated on the right axis.

which corresponds to the "no ring case". Here, the extracted coupling coefficient $\delta \approx 0.45$ corresponds to a zero crossing temperature shift of $\approx -25\,\mathrm{K}$. In this case, an optimal working point of the cavity close to 0 °C would require sophisticated temperature control and isolation schemes apart from potential condensation at optical windows.

Following the above considerations, the ULE rings have been manufactured with a thickness of 7 mm and an inner bore diameter of 8 mm. The optical contacting of the FS mirrors and the ULE rings has been accomplished by Thomas Legero at the Physikalisch Technische Bundesanstalt (PTB) in Braunschweig.

5.4 CAVITY MOUNTING AND TEMPERATURE STABILIZATION

Figure 5.5 shows computer-aided design (CAD) graphics of the basic elements for isolation of the cavity from external temperature fluctuations. The cavity resides in a CF flange which is mounted to an optical bread board by aluminum holders. The whole construction is enclosed by aluminum walls of 10 mm thickness (not shown) and a thermal insulation made from Styrodur (not shown). On the bottom of the bread board five peltier elements are installed for PID temperature control of the system. The control sensor for temperature stabilization is a standard 10 kΩ NTC sensor placed on the bottom of the bread board and another sensor is attached to the CF flange. The temperature of the inner system can now be tuned from $\approx 10\,°\mathrm{C}$ to $\approx 40\,°\mathrm{C}$ with an accuracy of $\approx 1\,\mathrm{mK}$ measured at the control sensor.

The pressure inside the flange is reduced to $\approx 1 \times 10^{-6}\,\mathrm{mbar}$ by a vibration-less ion getter pump (IGP). In addition to a reduction of temperature fluctuations through convection the vacuum also ensures stability of the effective refractive index. The close up view of the cavity in Fig.5.5 (b) reveals further measures to decouple the cavity from the environment. We specially emphasizes the two-stage decoupling by minimizing the mechanical contact to the flange through the radial support surface of the black plastic spheres with low thermal conductivity. Furthermore, a gold-plated copper casing with low surface emissivity ϵ provides shielding from thermal radiation of the flange's inner surface.

To estimate the thermal low pass properties of the construction, we employ a time-resolved FEM analysis of the entire cavity assembly using the CAD model (cf. Fig 5.5 (a)). Here, we can only account for the heat transfer caused by thermal conduction because the available version of COMSOL Multiphysics installed on the LUIS cluster computing is lacking the necessary modules for convection and thermal radiation.

Figure 5.6 shows the result of the simulation (dashed lines) for an instantaneous temperature step at $t = 0$ from $20\,°\mathrm{C}$ to $30\,°\mathrm{C}$ induced at the position of the peltier elements. Comparing the results of the simulation with measured temperatures at the control sensor (solid dark green line) and the flange sensor (solid light green

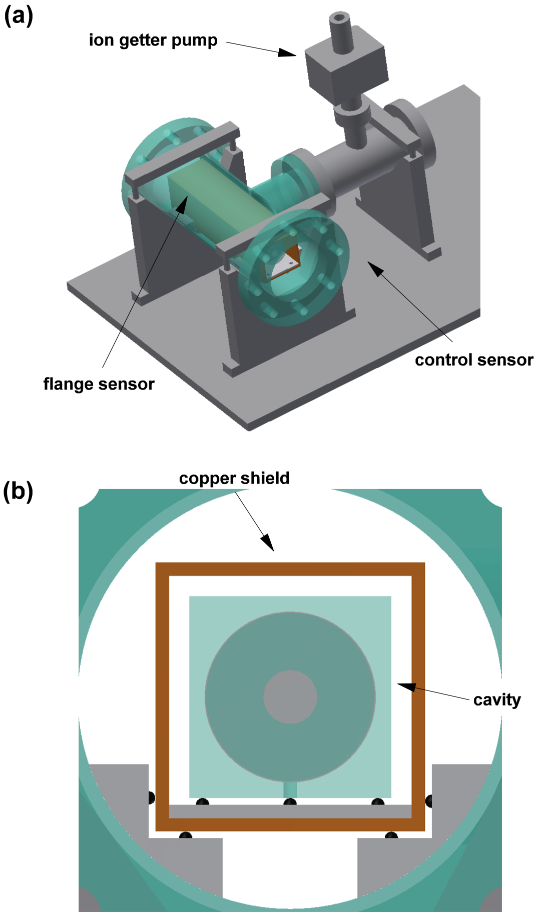
(a)
ion getter pump
flange sensor
control sensor
(b)
copper shield
cavity

Figure 5.5: **(a)** Overview of the cavity assembly. **(b)** Close up view of the cavity's three-point mounting and the gold-plated copper shield.

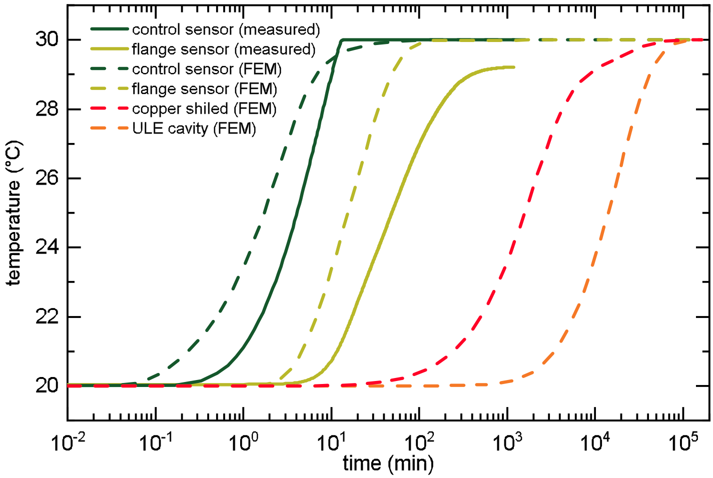

Figure 5.6: Measured (solid lines) and simulated (dashed lines) temperature response of different components of the cavity assembly.

line) reveals that in both cases the measured time constant[1] is a factor of ≈ 2.5 larger than the calculated time constant. However, this implies that the relative time scale between the temperature at the control sensor and the flange sensor is reproduced correctly by the model.

We further calculate the transient temperature at the copper (Cu) shield and at the cavity (cav) which amount to $\tau_{Cu} = 17.1\,\mathrm{h}$ and $\tau_{cav} = 165.9\,\mathrm{h}$.

---

[1] The time constant in this context is defined as $1/e$ rise time of the temperature.

5.5 THE POUND-DREVER-HALL TECHNIQUE

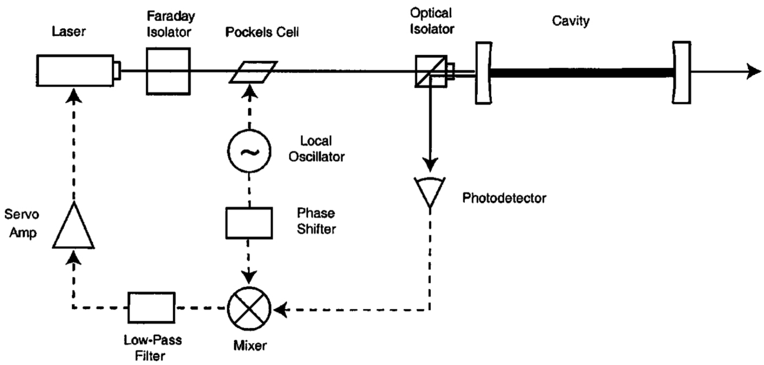

Figure 5.7: Schematic experimental setup for laser frequency stabilization with the Pound-Drever-Hall technique. Taken from Ref. [55].

In the experiment, frequency stabilization of the laser is realized by means of standard Pound-Drever-Hall (PDH) locking and we leave the description of the PDH technique to the experimental aspects as outlined in [55] which also provides a quantitative understanding of the technique. Figure 5.7 depicts the experimental setup for PDH locking.

First, the laser light is send trough a Faraday isolator[2] to prevent the light which is reflected from the cavity to re-enter the laser. The laser light with optical angular frequency ω (carrier) is phase modulated with the frequency Ω (compare Part 2) a fiber based EOM[3] leading to sidebands at the optical frequencies $\omega - \Omega$ and $\omega + \Omega$.

The optical isolator in front of the cavity consists of a polarizing beam splitter and a quarter-wave plate. The beam reflected from the cavity is detected by a photodetector where the reflected intensity P_{ref} is given by

$$P_{ref} = \left|E_{carrier} + E_{sidebands}\right|^2 . \tag{5.9}$$

---

[2] We use two Faraday isolators which add up to ≈ 60 dB of isolation. (30 dB internal isolator and 30 dB Thorlabs IO-2.5-1064-VLP)

[3] Instead of a Pockels cell.

Equation 5.9 approximates for the carrier frequency ω close to the cavity resonance to

$$P_{ref} \propto -\frac{\delta\omega}{\delta\nu} \sin\left(\Omega t\right), \tag{5.10}$$

where $\delta\omega$ is the deviation of the carrier from the cavity resonance and $\delta\nu$ is the width of the cavity resonance. Inspection of Eq. 5.10 shows that P_{ref} has the desired antisymmetric form[4] close to the resonance but oscillates with the modulation frequency Ω. Therefore, the signal of the photodetector is fed into an electrical mixer together with the local oscillator with frequency Ω_{LO}. The output of the mixer is given by

$$\sin\left(\Omega t\right) \sin\left(\Omega_{LO} t\right) = \frac{1}{2} \cos\left[\left(\Omega - \Omega_{LO}\right) t\right] - \frac{1}{2} \cos\left[\left(\Omega + \Omega_{LO}\right) t\right]. \tag{5.11}$$

The mixer output consists for $\Omega = \Omega_{L0}$ of a DC component and a signal proportional to 2Ω, which is blocked by a lowpass filter. The DC component is the characteristic PDH error signal depicted in Fig. 5.8 for a modulation frequency of $\Omega = 2\,\mathrm{MHz}$. The relatively large noise in the error signal is a typical indicator for a cavity with high finesse and reflects the laser frequency instability during the scan across the resonance.

Finally, the error signal is passed through a servo amplifier and directly fed into the tuning input of the laser. In the setup, the servo is a field programmable gate array (FPGA)-based unit[5] which allows for two independent PID loops with different bandwidths. The system is set such that the low frequency deviations ($\leq 100\,\mathrm{Hz}$) are mainly compensated by the piezo actuator which drives the optical grating in the ECDL. The high frequency components of the laser noise are reduced by feedback of the laser current.

---

[4] The antisymmetric form of the PDH error signal is one of the major advantages of this technique. It makes the quality of the lock independent on the laser intensity and directly dictates the direction of the feedback signal by its sign.

[5] Toptica Photonics DigiLock 110

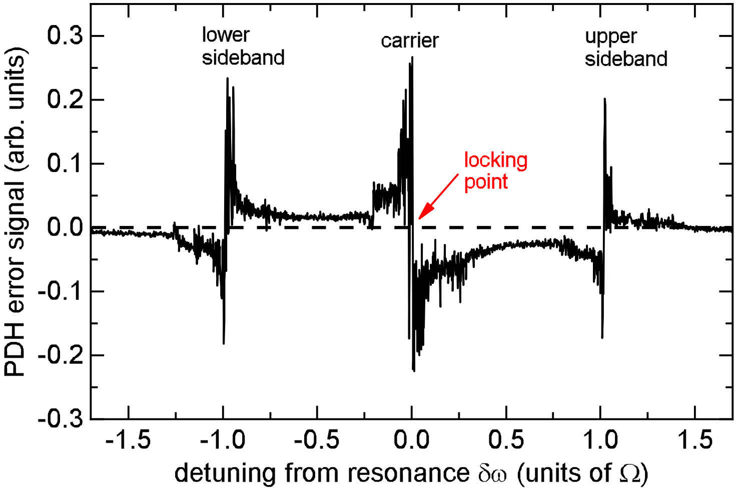

Figure 5.8: Measured PDH error signal as a function of the detuning from the resonance (in units of the modulation frequency Ω).

6

EVALUATION OF CAVITY PARAMETERS AND STABILITY

6.1 EVALUATION OF STABILITY AND CALIBRATION OF THE WAVEMETER

The evaluation of the frequency stability of a locked laser is usually measured against another laser with known stability [56] or in the best case by comparing the laser frequency against two other stable lasers in a three corner hat configuration. However, even without another stable laser, we still can give a quantitative estimate on the stability of the laser by measuring the power spectral density (PSD) $S_{\Delta\nu}(f)$ (in units of $\mathrm{Hz}^2\,\mathrm{Hz}^{-1}$) of the laser frequency noise. A real time Fourier analysis of the in-loop PDH error signal reveals the deviation of the error signal from its set point (e.g. 0 V) in the frequency domain. From the known amplitude and width of the error signal with respect to the optical frequency we can now compute $S_{\Delta\nu}(f)$ which is depicted in Fig. 6.1.

The graph shows the noise power spectral density for the free running laser (solid blue) and the locked laser (solid red). The gray line is the equivalent electrical noise of the photodetector which has been subtracted to obtain the locked spectrum. The low frequency PSD of the free running laser is governed by frequency flicker noise $S_{\Delta\nu}(f) \propto f^{-\alpha}$ [57] with $\alpha = 1.78$ and the flattening of the PSD at higher frequencies suggest white noise with a constant $S_{\Delta\nu}(f)$. On the other hand, the locked laser shows a significantly reduced PSD in a bandwidth of ≈ 100 kHz with the highest reduction of 14 orders of magnitude at the lowest frequency.
A more intuitive figure of merit is the laser rms linewidth $\Delta\nu_{rms}$ which coincides with the absolute frequency stability. It can be calculated from the PSD as [57]:

$$\Delta\nu_{rms}^2 = \int_0^\infty S_{\Delta\nu}(f)\mathtt{d}f. \tag{6.1}$$

The explicit evaluation of the infinite integral is limited due to finite measurement resolution. However, the integral can be evaluated numerically with the restriction that the result is valid for

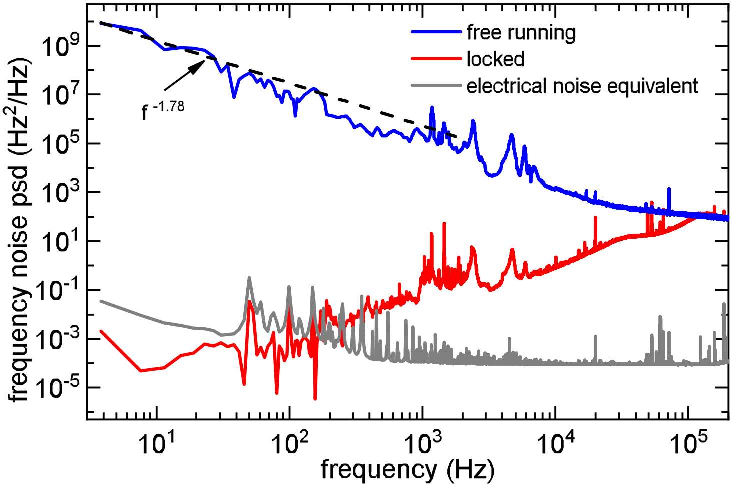

Figure 6.1: Frequency noise power spectral density for the free running (blue line) and the locked laser (red line). The gray line indicates the electrical noise of the detector.

a measurement time as long as the inverse of the lowest measured Fourier frequency $f_{min}^{-1} \approx 260\,\mathrm{ms}$. The results are:

$$\Delta\nu_{rms,\mathrm{FREE}} = 220\,\mathrm{kHz}$$
$$\Delta\nu_{rms,\mathrm{LOCKED}} = 4\,\mathrm{kHz}.$$

We expect the value for the locked laser also to be approximately valid at long times because the PSD is a strongly decreasing function of time. From the opposite argument, the value of the free running laser is strictly pinned to this measurement time. The order of magnitude of $\Delta\nu_{rms,\mathrm{FREE}}$ corresponds quite well to the frequency reading of a high resolution wavelength meter (WLM)[1] which fluctuates on the 1 MHz digit during 1 s. The uncertainty is caused by the specified measurement resolution of 500 kHz and an absolute accuracy of 2 MHz when calibrated every 2 min with a stable calibration source. This is necessary, because the WLM itself employs an interferometrically-based measurement and the parameters of the interferometer are expected to change under external perturbations such as temperature change or changes in the barometric pressure. Under these conditions, the cavity-stabilized

---

[1] HighFinesse WSU-2

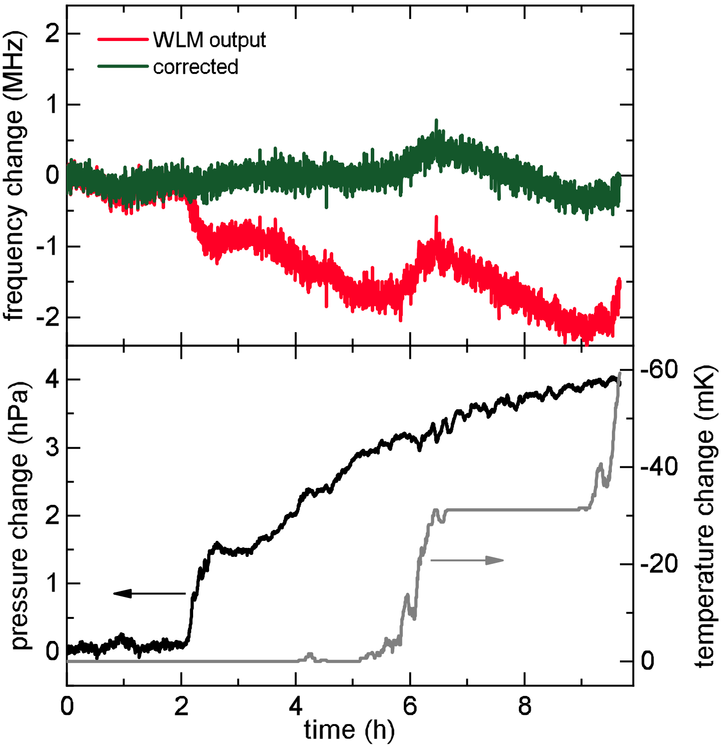

Figure 6.2: The upper panel shows the change in frequency output of the wavelength meter (red line). The green line shows the corrected values which are compensated for the pressure and temperature changes depicted in the lower panel.

laser itself is a tool to characterize the performance of the WLM. Therefore, we set the cavity to 20 °C and wait for several days to ensure a stable temperature at the cavity. Afterwards, the change of the frequency reading of the WLM is recorded for several hours which is displayed in the upper panel (red line) of Fig. 6.2. Meanwhile, we also monitor the change of the internal temperature sensor of the WLM (lower panel - gray line) and the change in barometric pressure (lower panel - black line) by an external pressure sensor. During the measurement time of $t_{meas} \approx 10\,\mathrm{h}$ the reading of the WLM decreases by $\approx 2\,\mathrm{MHz}$. Qualitatively, this can be explained by two distinct events. In the first event at $t \approx 2\,\mathrm{h}$ the ambient pressure increases quite strongly which is accompanied by a corre-

sponding decrease of the WLM reading. Afterwards the pressure continues to increase but with a reduced slope. This corresponds to the general decreasing trend of the WLM reading. In the second event at $t \approx 6\,\mathrm{h}$ the WLM reading increases against the pressure trend which is caused by the decreasing temperature.
For a quantitative analysis, a linear dependence between the frequency change Δf and the external parameters is assumed:

$$\Delta f = \alpha_p \Delta p + \beta_T \Delta T \tag{6.2}$$

where Δp (ΔT) is the pressure (temperature) change with respect to the value at $t = 0$. If we further require that the WLM reading should not change during t_{meas} the coefficients α_p and β_T can be extracted by a least square optimization. The corrected values for the WLM frequency reading is shown as the green line in the upper panel of Fig. 6.2 which has been calculated using the optimized coefficients:

$$\begin{aligned} \alpha_p &= \quad -576\,\mathrm{kHz\,hPa^{-1}} \\ \beta_T &= \quad -14\,\mathrm{kHz\,mK^{-1}}. \end{aligned}$$

Upon request, the manufacturer of the WLM specified the sensitivity of the device on pressures changes as $\approx 2\,\mathrm{fm\,hPa^{-1}}$ which corresponds to[2] $516\,\mathrm{kHz\,hPa^{-1}}$. This is in good agreement with the extracted value for α_p.

---

[2] at a wavelength of $\lambda \approx 1078\,\mathrm{nm}$

6.2 DETERMINATION OF THE ZERO CROSSING TEMPERATURE

The evident way to determine the zero crossing temperature of a ULE cavity is the stabilization of the assembly to different temperatures and measure the frequency change of the laser as a function of temperature. However, the time required to complete this procedure for several temperatures can be quite long (e.g., 30 days in Ref. [54]) because of the slow response time of the thermally decoupled cavity. Instead, we use a different approach which is less time consuming. The experimental protocol is illustrated in Fig. 6.3.

Starting from a constant temperature of $T_s = 22\,°\mathrm{C}$, the setpoint of the temperature control loop is modulated with an amplitude of 8 °C around T_s and a period of 6 h. After each period, T_s is increased by 2 °C (cf. Fig. 6.3 blue line). During the modulated ramping of the temperature we monitor the flange temperature sensor (orange line) and the frequency change of the locked laser

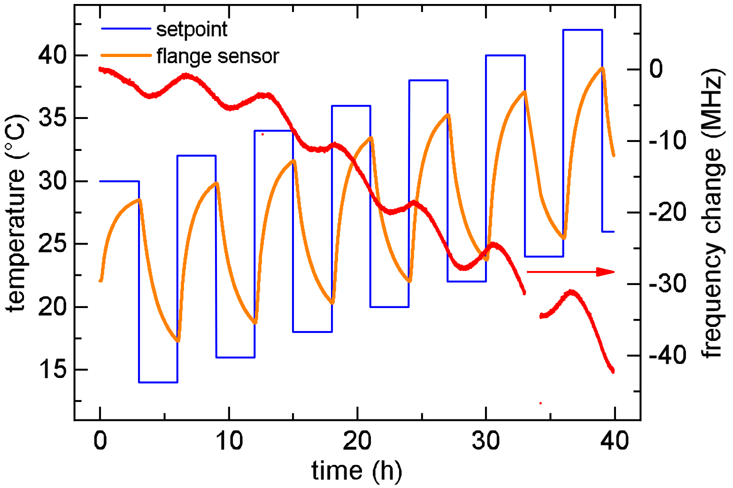

Figure 6.3: Modulated temperature ramping of the cavity assembly (blue line). The temperature response at the flange (orange line) is recorded as well as the change in optical frequency (red dots). Around $t = 33\,\mathrm{h}$ the laser temporarily lost the PDH lock.

through the corrected[3] WLM frequency readings (red dots).

A clear drawback of this method is that the measurement time can not directly be linked to the temperature of the resonator without knowledge of the temperature transfer function. As a first estimate, the last point of the measurement is considered, where the frequency has decreased by ≈ 42 MHz and the temperature at the flange has increased from 22 °C to 32 °C. Applying the cavity time constant $\tau_{cav} = 165.9\,\mathrm{h}$ from chapter 5.4 indicates that the cavity has not warmed up to more than 24 °C. We recall from the previous chapter that, around the zero crossing temperature T_0, the frequency change of the laser is given by

$$\Delta\nu = -\frac{a}{2} \cdot \nu_0 \cdot (T - T_0)^2. \tag{6.3}$$

A frequency shift of −42 MHz for a temperature step from 22 °C to 24 °C can only be realized if the zero crossing temperature is as low as $T_0 \approx -9\,°\mathrm{C}$ given that a stays in the range of reported values.

Such a low T_0 is not expected even in the absence of the compensating ULE rings (cf. ch. 5.3). Therefore, we conclude that the heat transfer from the vacuum flange to the cavity is neither governed by thermal conduction nor convection[4]. Consequently, the heat transfer has to be modeled by thermal radiation between the participating surfaces. The power P emitted by a gray body of surface area A and temperature T is given by

$$P = \epsilon \cdot \sigma \cdot A \cdot T^4, \tag{6.4}$$

where σ is the Stefan-Boltzmann constant and ϵ is the emissivity of the surface. Taking into account the different surface areas and emissivities we can set up the coupled differential equations for the heat transfer, where in the following the subscript s denotes the stainless steal flange, cu denotes the copper shield and u denotes the ULE cavity.

$$\begin{aligned}
\frac{dT_{cu}(t)}{dt} &= \frac{\epsilon_s \epsilon_{cu} \sigma A_s \left(T_s^4 - T_{cu}^4\right)}{C_{cu}\left(\epsilon_s + \epsilon_{cu} - \epsilon_s \epsilon_{cu}\right)} - \frac{\epsilon_u \epsilon_{cu} \sigma A_{cu} \left(T_{cu}^4 - T_u^4\right)}{C_u \left(\epsilon_u + \epsilon_{cu} - \epsilon_u \epsilon_{cu}\right)}, \\
\frac{dT_u(t)}{dt} &= \frac{\epsilon_u \epsilon_{cu} \sigma A_{cu} \left(T_{cu}^4 - T_u^4\right)}{C_u \left(\epsilon_u + \epsilon_{cu} - \epsilon_u \epsilon_{cu}\right)},
\end{aligned}$$

where C_i is the heat capacity of the respective component.

---

[3] see previous section

[4] The pressure inside the flange is $\approx 1 \times 10^{-6}$ mbar.

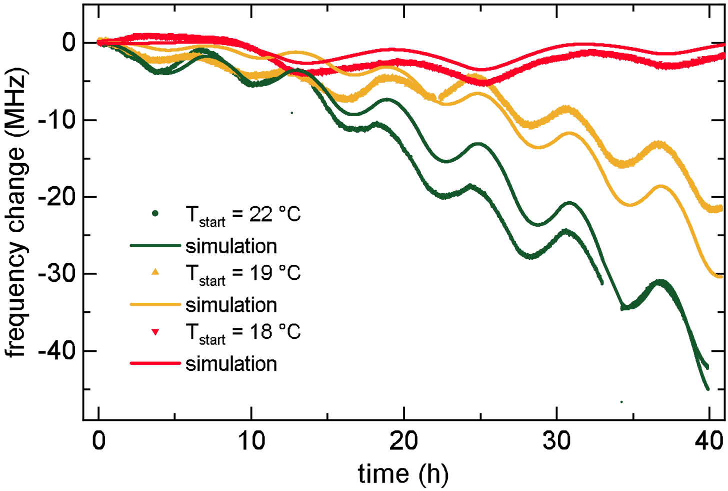

Figure 6.4: Time resolved laser frequency response to the modulated temperature ramping for different start temperatures (dots). The solid lines are the results of a simulation based on radiative heat transfer.

The transient frequency change of the cavity can now be evaluated by solving the differential equations and applying Eq. 6.2.
Figure 6.4 shows the result of this simulation for three different starting temperatures and the respective experimental data where we have used the measured temperature at the flange as input for $T_s(t)$.
The best agreement between the simulation and the data is obtained for $\epsilon_s = 0.3$, $\epsilon_c = 0.07$, $\epsilon_u = 0.8$, $a = 2 \times 10^{-9}\,\mathrm{K}^{-2}$ and $T_0 = 19\,\mathrm{K}$. We note that especially the literature values for the gold-plated copper shield are rather widely scattered which can be compensated by changing T_0. Therefore, the zero crossing temperature can only be specified in a confidence interval of $\pm 3\,\mathrm{K}$.

Most importantly, we have shown that the use of additional ULE rings on top of the FS mirror leads to an effective zero crossing temperature, which is conveniently realized in the laboratory. Even if detuned by 3 K from the zero crossing temperature, temperature fluctuations of 1 mK only affect the frequency stability by 1.7 kHz. This is still sufficient to unambiguously resolve the natural linewidth of an exciton bound to a boron acceptor which amounts to ≈ 150 kHz.

Part IV

ABSORPTION SPECTROSCOPY OF DONOR BOUND EXCITONS

ABSTRACT PART IV

This part addresses the fundamental properties of the phosphorus donor bound exciton transition under variation of external parameters such as temperature and magnetic field and lays the foundation for the advanced experiments presented in part V.
The maximum absorption coefficient of the inherently weak donor bound exciton transition is $\alpha_{max} = 0.142\,\mathrm{cm}^{-1}$ with an average optical linewidth of $\approx 70\,\mathrm{MHz}$ which is small enough to reveal the 117 MHz hyperfine coupling between the donor electron spin and the phosphorus nuclear spin. This extremely narrow linewidth enables us to examine the low temperature limit of the silicon bandgap energy where our analysis confirms the theoretical T^4 behavior. Moreover, the temperature-dependent width of the transition has been studied quantitatively and gives strong hints to elastic Raman scattering with phonons obeying a T^7 law.

The magnetic field dependence of the transition not only reveals the optical selection rules but also permits the extraction of the Landé g-factor for electrons and holes and an associated anisotropy with high accuracy. For a magnetic field applied along the [111] direction, we find

$$\begin{aligned} g_e &= 2.01(2), \\ g_{1/2} &= 1.42(1), \\ g_{3/2} &= 1.27(1). \end{aligned}$$

7

ABSORPTION WITHOUT MAGNETIC FIELD

7.1 ABSORPTION COEFFICIENT OF THE NO-PHONON LINE

Here, we show the basic properties of the zero field absorption spectrum of the phosphorus-bound D^0X transition located at $\approx 1078.263\,\mathrm{nm}$. The absolute frequency or wavelength depends strongly on the calibration of the WLM and is of minor interest in this context. Therefore, most of the presented spectra are plotted in relative frequency units.

Figure 7.1 (bottom left) shows the transmitted signal of a scan across the transition for a temperature of $T = 4.5\,\mathrm{K}$. After subtraction of a linear background due to increasing laser power with increasing wavelength, the absorption coefficient of the transition can be evaluated using Lambert-Beer's law:

$$I(z) = I_0 \exp\left(-\alpha \cdot z\right), \tag{7.1}$$

where $I(z)$ is the transmitted intensity after the laser beam has traveled the distance z inside the absorptive medium, I_0 is the incident intensity, and α is the absorption coefficient of the medium conveniently given in units of cm^{-1}.

With a sample length of $z = L = 0.4\,\mathrm{cm}$ and the values for I_0 and $I(z)$ indicated in Fig. 7.1 (bottom left), the maximum absorption coefficient can be determined as:

$$\alpha_{max} = 0.142\,\mathrm{cm}^{-1}.$$

Figure 7.1 (bottom right) shows differential phase modulation spectroscopy data of the same scan. Direct comparison of the collateral spectra clearly demonstrates the superior signal to noise ratio of the differential technique.

Integration of the latter leads to the absorption spectrum depicted in Fig. 7.1 (top), where the maximum is normalized to α_{max}.

The spectrum for ^{28}Si shows in contrast to the bound exciton spectrum of natural abundance silicon, which only contains a single line [58], two distinct maxima separated by $\approx 120\,\mathrm{MHz}$. This is

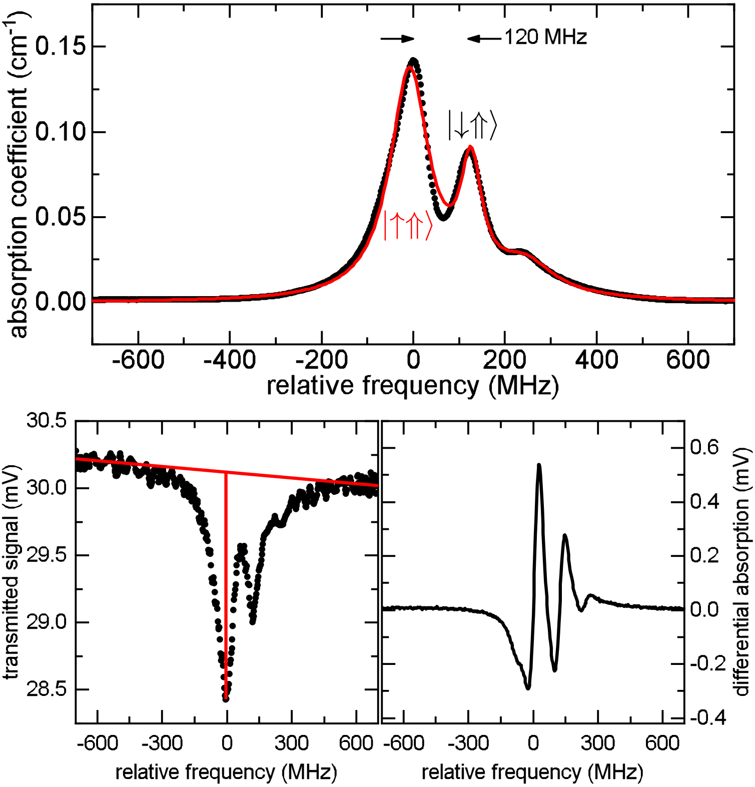

Figure 7.1: **(top)** D^{0}X absorption spectrum integrated from the differential spectrum shown on the bottom right. **(bottom left)** Unmodulated absorption scan of the D^{0}X transition.

in good agreement with the 117 MHz hyperfine splitting of the phosphorus neutral donor ground state [10]. Therefore, the low energy peak can be attributed to the three-fold degenerate triplet state of donor electron spin and phosphorus nuclear spin ($|\uparrow\Uparrow\rangle$) and the high energy peak corresponds to the anti-parallel singlet state ($|\downarrow\Uparrow\rangle$).

The intensity ratio, extracted from a Lorentzian line shape analysis (red line), of the two peaks amounts to 3.5 : 1 which confirms this picture. The average linewidth of the transition is $\Delta\nu \approx 81$ MHz. The value of α_{max} can be compared to the value found by Dean [59].

Taking his value of the oscillator strength $f = 1.8 \times 10^{-6}$ for the no phonon transition of the bound exciton, α_{max} may be estimated as

$$\alpha_{max} = \frac{n_d \cdot f}{0.97 \times 10^{16} \cdot n \cdot \Delta\nu_{eV}} = 0.2\,\mathrm{cm}^{-1}, \tag{7.2}$$

where n_d is the donor density (in cm^{-3}), n is the refractive index of silicon and $\Delta\nu_{eV}$ is the linewidth in eV.

7.2 CONSIDERATIONS ON SPECTRAL WIDTH AND LINESHAPE

The presence of ionized acceptors A^- will lead to an effective Stark shift which manifests itself in the $\mathrm{D}^0\mathrm{X}$ spectra by a broadening of the low energy tail [60]. The Stark shift can be accounted for by fitting the differential[1] spectrum in Fig. 7.1 (bottom right) with a skewed Lorentzian of the form

$$L(x) = \begin{cases} \frac{1}{1+\left(\beta\frac{(x-x_0)}{\gamma}\right)^2} & \text{for } x < x_0 \\ \frac{1}{1+\left(\frac{(x-x_0)}{\gamma}\right)^2} & \text{for } x \geq x_0 \end{cases} \tag{7.3}$$

where x_0 is the center of the transition, γ is the half width at half maximum (HWHM) of the high energy side and γ/β is the HWHM of the low energy side. Figure 7.2 illustrates on the left hand side the standard derivative Lorentzian ($\beta = 1$) depicted by the green line, and the red line denotes the fit according to Eq. 7.3 which significantly improves the agreement with the experimental data, especially at the low energy tail of the $F = 1$ transition. The mean FWHM linewidth $\Gamma = 2 \cdot \gamma$ is reduced to 72 MHz which is still approximately two order of magnitude larger than the lifetime limited linewidth [26], a fact has been addressed in Ref. [61]. On the basis of high resolution spectroscopy on samples with different isotopical purity ϵ they argue that the linewidth Γ varies as

$$\Gamma(\epsilon) = \alpha_\Gamma \sqrt{(1-\epsilon)}. \tag{7.4}$$

This is illustrated as black line in Fig. 7.2 (right) together with experimental data from Ref. [61] (green dots). The constant $\alpha_\Gamma =$

---

[1] Here, the differential form is chosen because the deviations between the skewed Lorentzian and the standard Lorentzian are clearly visible.

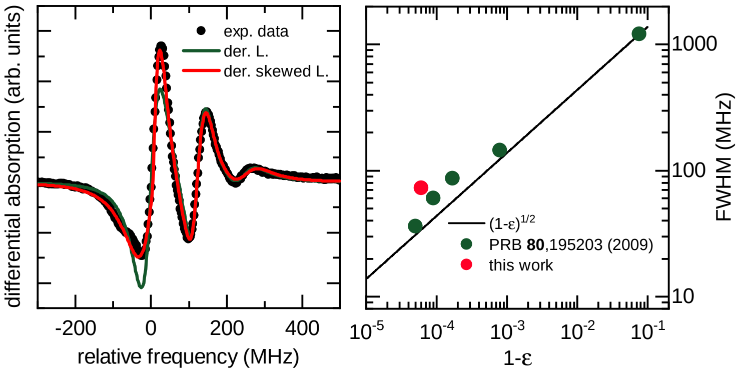

Figure 7.2: **(left)**Differential D^0X absorption spectrum (black dots) and line shape fits with a skewed differential Lorentzian (see Eq. 7.3) (red line) and a standard differential Lorentzian (green line). **(right)** Evolution of the D^0X spectral width as a function of the isotopical purity ϵ. The green dots represent experimental data from Ref. [61].

4366 MHz has been chosen to account for the 1.2 GHz linewidth in $^{\text{nat}}$Si with $\epsilon = 0.9233$. The red dot denotes the FWHM obtained in this work and exhibits a value which is approximately two times larger than expected from Eq. 7.4. However, the doping densities in Ref. [61] are on the order of $1 \times 10^{13}\,\text{cm}^{-3}$ while the doping density in the sample under investigation in this work is $n_d = 1.2 \times 10^{15}\,\text{cm}^{-3}$. Therefore, the inter donor spacing is in our sample significantly lower which leads to an enhanced probability of nearest neighbor interaction. A semi-quantitative estimate of this effect can be given by considering the wave function overlap of the ground states for two neighboring donors

$$S(R(n_d)) = \langle \Psi(r, R = 0) | \Psi(r, R = R_{NN}(n_d) \rangle \,, \tag{7.5}$$

where $\Psi(r, R)) \propto \exp(-(r - R)/a_{B,D})$ is the donor ground state wave function at the lattice site R and $R_{NN}(n_d) = 0.54 n_d^{-1/3}$ is the most probable nearest neighbor distance assuming the donor distribution obeys Poisson statistics [62].

Therefore, the fraction

$$\frac{S\left(R\left(n_d = 1 \times 10^{15}\,\mathrm{cm}^{-3}\right)\right)}{S\left(R\left(n_d = 1 \times 10^{13}\,\mathrm{cm}^{-3}\right)\right)} = \frac{10^{-8}}{10^{-48}} \tag{7.6}$$

reveals a huge increase in the overlap when increasing the doping density from $1 \times 10^{13}\,\mathrm{cm}^{-3}$ to $1 \times 10^{15}\,\mathrm{cm}^{-3}$ which may be responsible for the larger linewidth found in this work.

7.3 TEMPERATURE DEPENDENT SPECTROSCOPY

The ultra-narrow linewidth of the D^0X transition promises to be an excellent marker for temperature related phenomena such as phonon mediated broadening of spectral lines and the shift of the silicon bandgap. In Fig.7.3 we exemplary show differential absorption spectra for different temperatures ranging from 1 K (green line) to 9 K (red line).

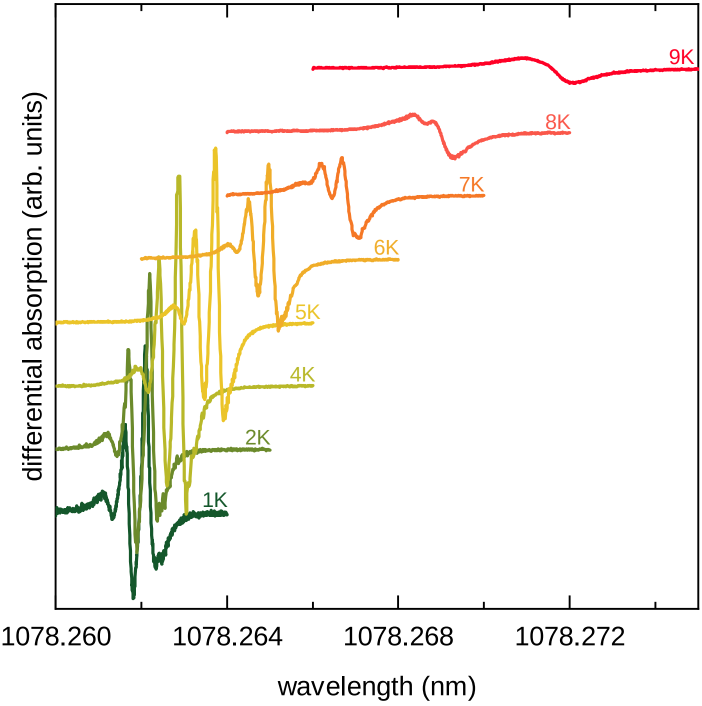

Figure 7.3: Differential D^0X absorption data for different temperatures, as indicated next to the respective line. The spectra are vertically offset for clarity.

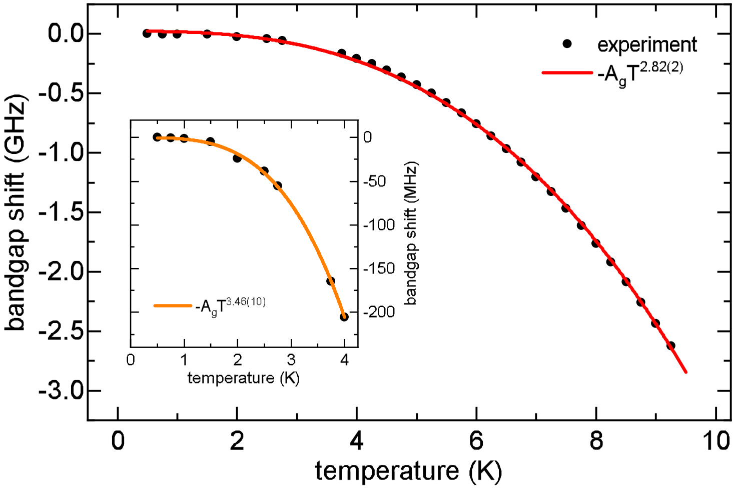

Figure 7.4: Experimental temperature dependence of the silicon bandgap (black dots) fitted by a power law (red line). The inset shows a close up view of the low temperature limit. The exponent of the fit favors the theoretical T^4 dependence (see main text).

Three major observations are evident:
First, the position of the peak shifts to longer wavelength (lower energy) with increasing temperature. Figure 7.4 depicts the relative shift of the center of the D^0X transition (black dots) as extracted from a Lorentzian line shape analysis over the whole range of measured temperatures. A fit to the data (red line) with a power law of the form $\Delta E_{gap} = -A_g \cdot T^p$ shows satisfactory agreement for $p = 2.82(2)$.
In Ref. [63], Cardona et al. pointed out that the often used empirical Varshni formula [64]

$$E_{gap} = E\left(T=0\right) - \frac{\alpha T^2}{T+\beta} \tag{7.7}$$

can not account correctly for the temperature dependence of a semiconductor's bandgap in the low temperature limit[2]. Instead, they argue that in the low temperature limit the bandgap energy should behave like T^4. Utilizing high precision spectroscopy on

---

[2] This also holds for our data. The deviations are pronounced to such an extend that a plot of Eq. 7.7 in Fig. 7.4 would almost completely vanish underneath the inset and is therefore omitted.

donor bound excitons in isotopically enriched silicon they are able to extract an exponent between $p = 3.6$ and $p = 3.9$ depending on the highest temperature used for the fitting procedure. Considering the same range of temperatures (see inset of Fig. 7.4) we can extract an exponent of $p = 3.46(10)$ which is close to the lowest value reported in Ref. [63].
A crucial physical aspect in the extraction of the bandgap shift is to avoid laser heating of the lattice, which is expected to play an important role at very low temperatures, because the thermal conductivity κ of silicon decreases with T^{-3} for $T < 20\,\mathrm{K}$ [65]. This effect is demonstrated in Fig. 7.5 where we plot the measured temperature change of the silicon lattice (colored dots) as a function of absorbed laser power at the maximum of the transition. For a nominal temperature of 500 mK and an absorbed power of $\approx 500\,\mathrm{nW}$ the temperature change is as high as 2.2 K[3] which corresponds to a frequency shift of $\approx 19\,\mathrm{MHz}$. Such a large shift would clearly distort an exact determination of the temperature dependent bandgap energy. Therefore, we have ensured that the experiments at very low temperatures are conducted with appropriately low laser power.

Further insight into the laser-induced heating of the silicon lattice can be gained by FEM simulations where the sample geometry as well as the geometry of the heat source can be taken into account properly. Using suitable low temperature values for the thermal conductivity of silicon and helium, a maximum temperature change of $\approx 11\,\mathrm{mK}$ is obtained which is in striking contrast to the experimentally determined value. This contradiction can be resolved by considering a thermal boundary resistance (Kapitza resistance) R_K [44] between the helium reservoir and the bulk silicon sample. This thermal boundary resistance can be explained qualitatively by an acoustic mismatch between the silicon sample and the helium reservoir which prohibits effective phonon transfer across the sample boundary. As an estimate, the thermal contact between the helium reservoir and the sample is modified by the Kapitza resistance between helium and silicon at $\approx 1\,\mathrm{K}$ [66]. The result of this estimation is depicted in Fig. 7.5 as solid lines for different temperatures and is in surprisingly good agreement with the experimental findings

---

[3] The temperature change is evaluated from the respective measured frequency change of the D^0X transition by using the T^4 dependence of the bandgap shift.

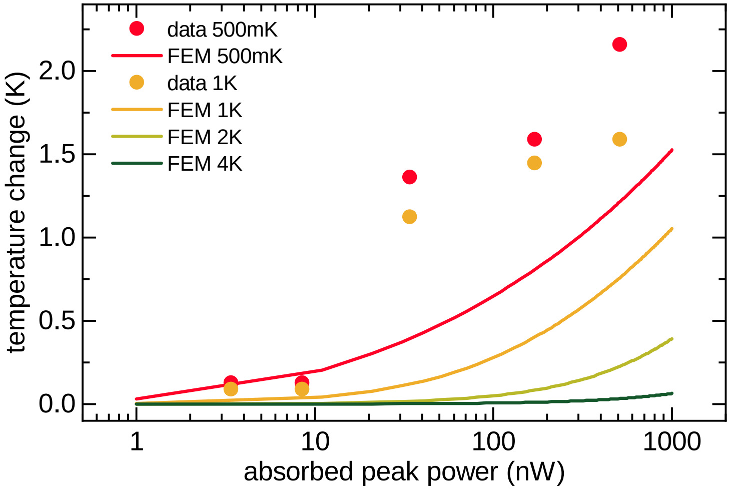

Figure 7.5: Experimentally determined temperature change of the silicon lattice as function of absorbed laser power (colored dots). The solid lines are FEM simulations taking thermal boundary resistance into account.

given the simplicity of the estimate.

The second observation in Fig.7.3 is that the width of the transition increases between 6 K and 9 K drastically until the hyperfine splitting is not resolved anymore at 9 K. Figure 7.6 (left) shows the extracted linewidth Γ as a function of temperature. The linewidth stays approximately constant at 70(3) MHz for temperatures up to ≈ 4.5 K and increases up to ≈ 550 MHz at 9 K. The solid red line is a fit to the linewidth $\Gamma(T)$ with [67]

$$\Gamma(T) = \Gamma_0 + a \times T^7. \tag{7.8}$$

Such a T^7 dependence has been observed before, e.g., in rare earth doped ceramics [68] and in rubidium [67] and has been attributed to elastic Raman scattering with phonons.
Thirdly, the temperature dependent absolute strength of the D^0X is displayed on the right side of Fig. 7.6 as Arrhenius plot. For the linear fit (red line) only inverse temperature vales up to $0.16\,\mathrm{K}^{-1}$ are considered. The slope yields a temperature of 20.4 K which corresponds to an activation energy of $E_a = 1.76\,\mathrm{meV}$. This value is lower than the expected value of one tenth of the donor ground

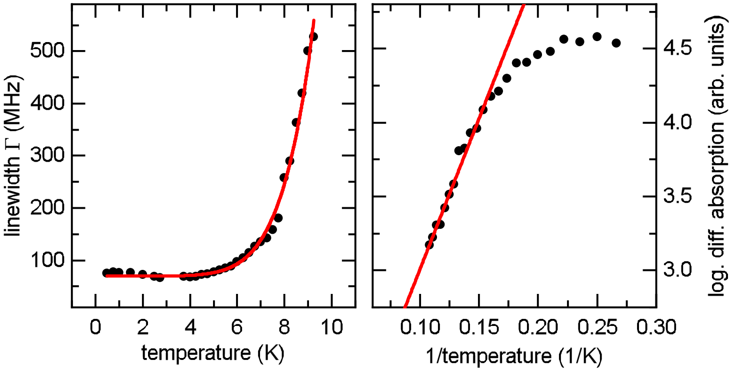

Figure 7.6: **(left)** D^0X linewidth for increasing temperature. **(right)** Arrhenius plot of the D^0X maximum intensity.

state binding energy $E_B = 45.3\,\text{meV}$ according to Haynes' rule [37]. The only other known energy value in the vicinity of E_a is the ionization energy of the positively charged boron acceptor [69]. The related competing electron capture mechanism leads to a decrease of the D^0X intensity for p-type silicon as described by Yang [60] which, however, does not apply to the present n-type sample. Thermal excitation of the excited D^0X state can also be ruled out because the associated energy difference amounts to $\approx 4.3\,\text{meV}$ [70].

8

ABSORPTION WITH MAGNETIC FIELD

8.1 OPTICAL SELECTION RULES

When an external magnetic field is applied, the ground state degeneracy of the F=1 state is lifted and the energy of the hyperfine-coupled donor electron evolves according to the Breit-Rabi equation (cf. chapter 2.2). The Zeeman shift of the D^0X is governed by the respective quantum number for the hole spin which leads to the twelve dipole-allowed transitions depicted in Fig. 2.6. Figure 8.1 shows absorption spectra for an external magnetic field of 50 mT applied in longitudinal direction z, i.e., the direction of light propagation. When the excitation laser is right-handed circularly polarized (σ^- - red line) only the lines 1-4 are visible in accordance with the optical selection rules.[1] Consequently, left-handed circularly polarized light

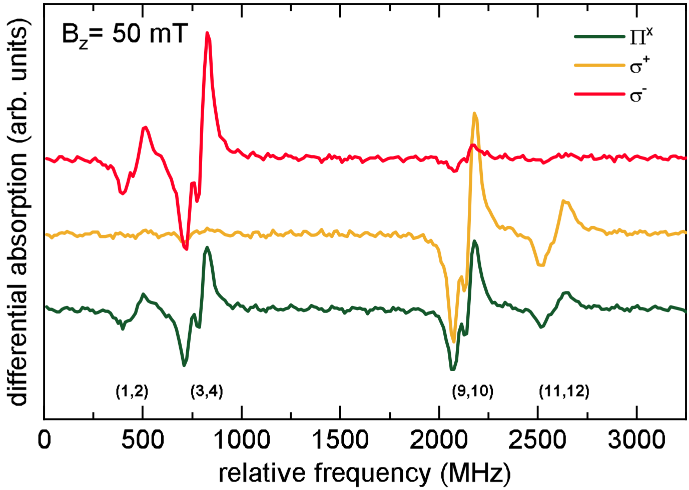

Figure 8.1: Experimental verification of the circularly polarized D^0X transitions.

---

[1] The residual intensity at the position of line (9,10) might be due to slight misalignment of the quarter-wave plate.

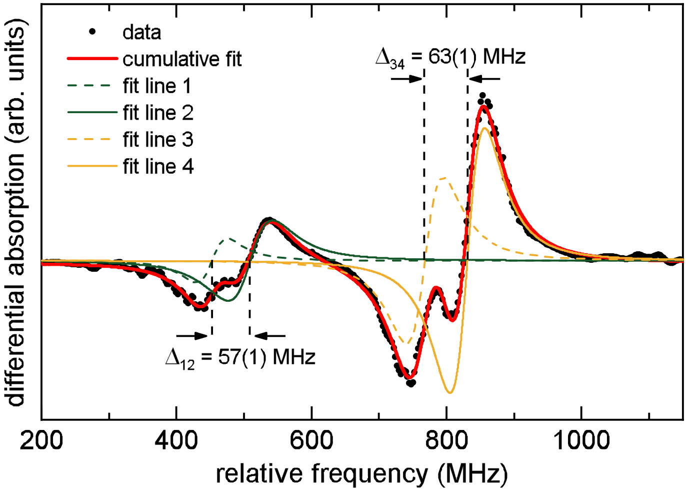

Figure 8.2: High resolution scan revealing the hyperfine splitting in an external magnetic field $B_z = 50\,\mathrm{mT}$

(σ^+ - orange line) can only excite lines 9-12. Finally, a scan with linearly polarized light (Π^x - green line) addresses all of the aforementioned lines with half intensity, because the linearly polarized light can be regarded as a combination of σ^- and σ^+. A closer inspection of the line structure in Fig. 8.1 shows a substructure near the zero crossing of each peak which corresponds to the maximum of the integrated spectrum. This is further investigated by the high resolution scan depicted in Fig. 8.2 for σ^- excitation.

The peak structure is fitted with a cumulative four Lorentzian derivative function (red line) which yields excellent agreement with the data, confirming the homogeneously broadened nature of the transitions. The respective single contributions to the lineshape are also indicated. This allows to determine the magnitude of the doublet splitting and we obtain a splitting of $\Delta_{12} = 57(1)\,\mathrm{MHz}$ for the doublet (1,2) and $\Delta_{34} = 63(1)\,\mathrm{MHz}$ for the doublet (3,4). Both values are in good agreement with the solution of the Breit-Rabi equation (compare Eq. 2.10) for 50 mT which yields $\Delta_{12} = 56.3\,\mathrm{MHz}$ and $\Delta_{34} = 61.2\,\mathrm{MHz}$.

The remaining linearly polarized transitions (lines 5-8), which have not yet been discussed, are visible when the linear laser polarization

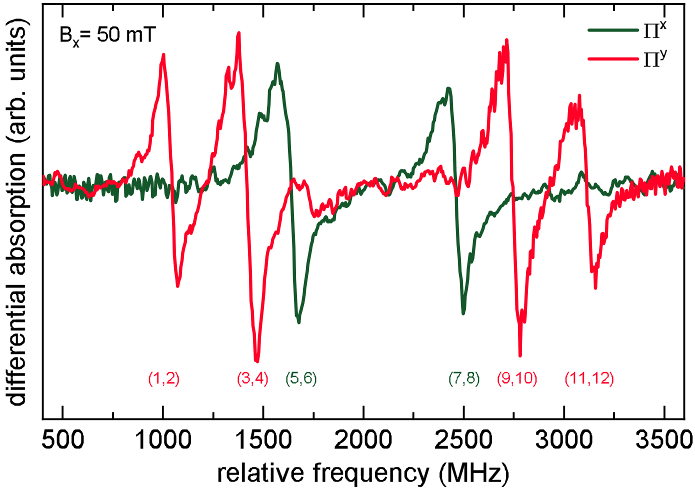

Figure 8.3: Experimental verification of the linearly polarized D^{0}X transitions.

is parallel to the external magnetic field as depicted by the green line in Fig. 8.3 for both, the laser polarization and the external magnetic field in x direction. Changing the laser polarization to Π^y, the linear components vanish and the circular components are excited by half of their magnitude. These findings bear important consequences for part V of this work. In the framework of pump-probe experiments, it is often cumbersome to filter the usually much stronger pump laser while detecting the weaker probe laser. Here, the optical selection rules are in favor of such experiments because it is possible to pump, for example, the doublet (3,4) with Π^y polarization and probe the doublets (5,6) and (7,8) with Π^x polarization. Hence, a linear polarizer in x-direction in the detection path will suppress the cross-polarized pump beam efficiently.

8.2 DETERMINATION OF THE LANDÉ G-FACTORS

The narrow linewidth of the D^0X transition allows for the determination of the incorporated Landé g-factors at moderate magnetic fields up to $B \approx 100\,\mathrm{mT}$, in contrast to previous studies on ^{nat}Si [71] with magnetic fields up to 5.5 T. The main advantage of low magnetic fields is that the line splitting is mainly governed by the linear Zeeman energy and the diamagnetic shift of the D^0X complex, which is quadratic in B, can be neglected. In order to observe all six magnetic doublets, the magnetic field is applied at the x and the z coil with $B_x = B_z$. Figure 8.4 shows differential absorption spectra for the highest magnetic field employed ($B_x = B_z = 70\,\mathrm{mT}$ - red line) and for the lowest magnetic field ($B_x = B_z = 20\,\mathrm{mT}$ - green line).

Below 20 mT at each coil, the spectra can not be fitted with six individual Lorentzians. Therefore, our study is limited to the case $\mu_B \cdot B > A$, where μ_B is the Bohr magneton. Figure 8.5 (left) shows the frequency shift of the spectral lines (colored dots) as extracted from Lorentzian lineshape fits as a function of the total magnetic field magnitude $B = \sqrt{B_x^2 + B_z^2}$. The solid lines connecting the dots are linear fits.

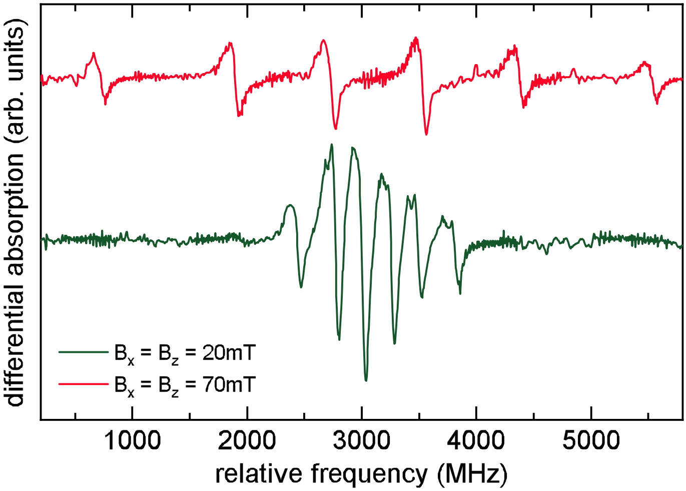

Figure 8.4: Exemplary differential absorption spectra for g-factor determination.

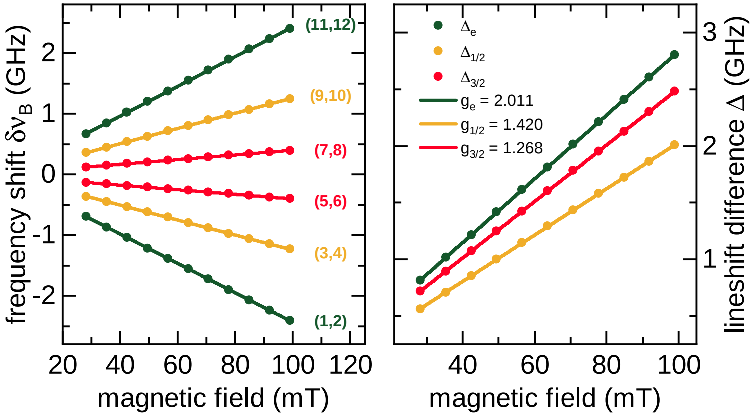

Figure 8.5: **(left)** Color-coded frequency shifts of the six D^0X doublets in an external magnetic field. **(right)** lineshift difference used to extract the Landé g-factors (see main text).

The individual g-factors can be obtained by subtraction of two different lines. In the following, g_e denotes the g-factor of the donor bound electron and $g_{1/2}$ and $g_{3/2}$ are the g-factors of the light and heavy holes, respectively. For the case of g_e, the difference Δ_e between the doublets (7,8) and (1,2) reads

$$\begin{aligned}\Delta_e\,(B) &= \delta\nu_{B(7,8)} - \delta\nu_{B(1,2)} \\ &= \frac{1}{2}g_e\mu_B B - \frac{1}{2}g_{1/2}\mu_B B - \left(-\frac{1}{2}g_e\mu_B B - \frac{1}{2}g_{1/2}\mu_B B\right) \\ &= g_e\mu_B B.\end{aligned}$$

For $g_{1/2}$ we have

$$\begin{aligned}\Delta_{1/2}\,(B) &= \delta\nu_{B(5,6)} - \delta\nu_{B(1,2)} \\ &= g_{1/2}\mu_B B.\end{aligned}$$

The determination of $g_{3/2}$ can be done in a similar way. However, there is no possible combination which allows to express a line shift difference as a function of $g_{3/2}$ alone. With prior knowledge of g_e, $g_{3/2}$ can be evaluated as

$$\begin{aligned}\Delta_{3/2}\,(B) &= \delta\nu_{B(9,10)} - \delta\nu_{B(3,4)} \\ &= (3g_{3/2} - g_e)\,\mu_B B.\end{aligned}$$

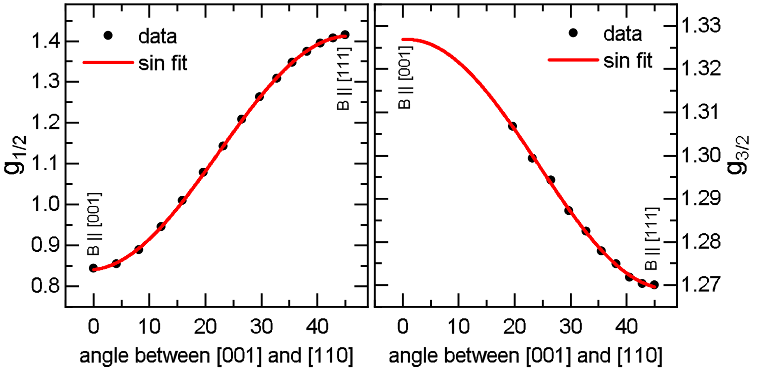

Figure 8.6: **(left)** Experimental anisotropy of the light hole g-factor (black dots). The red line is a fit to the data with a sine function. **(right)** Anisotropy of the heavy hole g-factor.

The three differences $\Delta_i(B)$ are plotted on the right side of Fig. 8.5. From the slope of the respective linear fit, the g-factors are determined and yield

$$\begin{aligned} g_e &= 2.01(2) \\ g_{1/2} &= 1.42(1) \\ g_{3/2} &= 1.27(1). \end{aligned}$$

Furthermore, on the basis of symmetry considerations it is expected, that the g-factors of the light hole and the heavy hole should differ significantly if the external magnetic field is either applied parallel to the [001] or parallel to the [111] crystallographic axis [71], i.e., the hole g-factors are anisotropic. This is demonstrated in Fig. 8.6. The direction of the effective magnetic field is altered by keeping the field of the coil oriented in [001] direction constant while ramping up the magnetic field of the [110]-oriented coil. When the two coils are operated at the same field, the resulting magnetic field is oriented parallel to the [111] direction. The most pronounced anisotropy is observed for the light hole ($g_{1/2}$ (left)) where the value changes from 0.84(1) for $B \parallel [001]$ to 1.42(1) for $B \parallel [111]$ in good agreement with previous studies [71]. Moreover, the anisotropy is extremely well characterized by a sine function (red line), enabling full understanding of the Zeeman splitting of D^0X transitions in an arbitrarily oriented magnetic field. For the heavy hole g-factor, it was not possible to extract reliable values for angles $< 20^\circ$ because the necessary lines vanish due to the D^0X optical selection rules. Instead, the value for the g-factor along the [001] axis is extracted from the sine fit and is in very good agreement with the value reported in Ref. [72].

Part V

OPTICAL SPIN PUMPING OF DONOR BOUND ELECTRONS

ABSTRACT PART V

This part addresses the effect of optical spin pumping of donor bound electrons by resonant excitation of donor bound exciton transitions. First, the conceptual mechanism of spin pumping is established in chapter 9 by continuous wave spectroscopy which builds the basis for the time-resolved two-color experiments presented in chapter 10 allowing for a direct observation of the donor electron polarization dynamics. Supported by detailed numerical simulations, we are able to show quantitatively that inelastic collisions between hot Auger electrons and donor bound electrons lead to an Orbach-type spin relaxation mechanism which strongly depends on the number of free electrons and thus the laser intensity. As a key parameter we extract $\zeta = 3.2$, i.e., the number of inelastic collisions a single hot Auger electron undergoes during its energy relaxation towards the band minimum. Furthermore, we find a universal expression for the dependence of the spin relaxation time on the density of conduction band electrons which only consists of sample-specific constants such as doping density, free electron capture time, and excited donor state lifetime.

9

CONCEPTUAL IDEA AND MECHANISM

The feasibility of donor electron polarization by optical pumping of donor bound exciton transitions at moderate magnetic fields relies on the individual addressability of a specific electron spin state at each of the dipole allowed doublets and thus on the narrow linewidths of the D^0X transitions. Table 9.1 summarizes the essential properties of the six dipole allowed doublets.

The doublets (5,6) and (7,8) have identical oscillator strength but different electron spin. Therefore, these transitions are ideally suited to monitor the donor electron spin polarization ρ. Throughout this work, the polarization is obtained by the integrated intensity I of the respective line by means of a Lorentzian line shape fit and the polarization is evaluated as:

$$\rho = \frac{I(5+6) - I(7+8)}{I(5+6) + I(7+8)}. \tag{9.1}$$

As a primary attempt to achieve donor electron spin polarization a pump-probe scheme based on the broadband fiber-based EOM is employed. In this scheme, the carrier at frequency ω serves as the pump beam while the positive side band $\omega + \Omega$ is scanned across the D^0X transitions by increasing the modulation frequency Ω. The signal-to-noise ratio is substantially increased by amplitude

doublet	electron spin	rel. oscillator strength
(1,2)	$\lvert\uparrow\rangle$	1/6
(3,4)	$\lvert\downarrow\rangle$	1/2
(5,6)	$\lvert\uparrow\rangle$	2/3
(7,8)	$\lvert\downarrow\rangle$	2/3
(9,10)	$\lvert\uparrow\rangle$	1/2
(11,12)	$\lvert\downarrow\rangle$	1/6

Table 9.1: Summary of the direction of electron spin and relative oscillator strength associated with the six dipole allowed doublets.

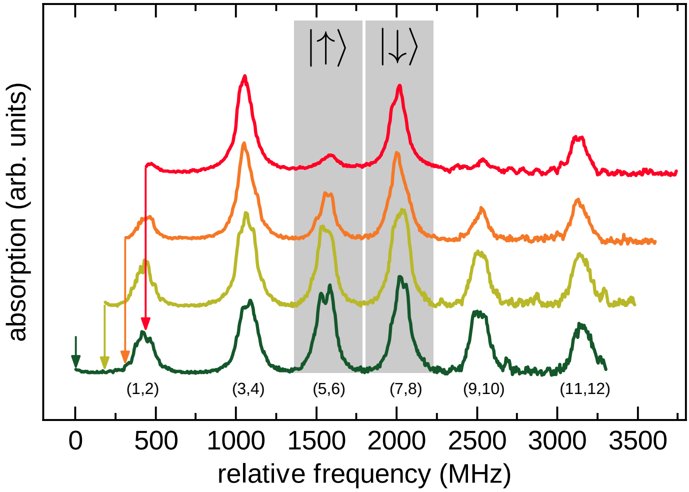

Figure 9.1: Exemplary D^0X spectra illustrating the electron spin polarization by optical pumping. The vertical arrows indicate the spectral position of the carrier (pump). The spectra are vertically offset for clarity.

modulation of the EOM driving voltage (at frequency Ω) by $f_{mod} = 50\,\text{kHz}$ and subsequent lock-in detection at f_{mod}.

Figure 9.1 shows D^0X probe spectra for different detunings of the carrier from the doublet (1,2) which is indicated by the vertical arrows. Starting at a large detuning of $\Delta_P = -400\,\text{MHz}$ for the pump (dark green line), the probe spectrum shows the equilibrium situation with $\rho = -2(2)\,\%$. When the pump detuning Δ_P is decreased the polarization builds up gradually and reaches its maximum value of $\rho = -68(2)\,\%$ (red line) when the carrier ω is quasi resonant with the doublet (1,2). The basic mechanism of the polarization process is outlined in Fig. 9.2.

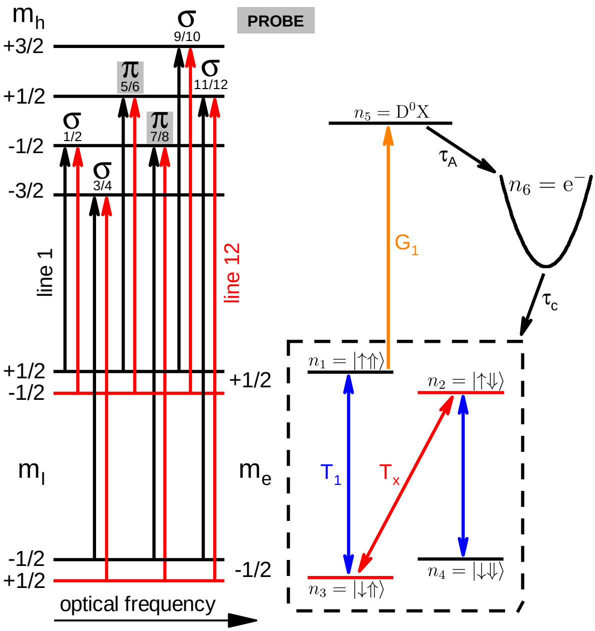
m_h
+3/2
+1/2
-1/2
-3/2
σ 9/10
PROBE
π 5/6
σ 11/12
σ 1/2
π 7/8
σ 3/4
line 1
line 12
+1/2
-1/2
+1/2
m_l
m_e
-1/2
+1/2
-1/2
optical frequency
$n_5 = \mathrm{D}^0\mathrm{X}$
τ_A
$n_6 = \mathrm{e}^-$
G_1
τ_c
$n_1 = |\uparrow\Uparrow\rangle$
$n_2 = |\uparrow\Downarrow\rangle$
T_1
T_x
$n_3 = |\downarrow\Uparrow\rangle$
$n_4 = |\downarrow\Downarrow\rangle$

Figure 9.2: **(left)** Dipole allowed $\mathrm{D}^0\mathrm{X}$ transitions. **(right)** Excitation scheme for optical spin pumping of donor electrons.

In the quasi resonant case, donor bound excitons are created from the state $n_1 = |\uparrow\Uparrow\rangle$ by resonant laser excitation with the rate G_1 (orange arrow) which depends on the laser intensity and the absorption coefficient of the respective line. The $\mathrm{D}^0\mathrm{X}$ subsequently decays with high probability via Auger recombination with the characteristic time $\tau_A = 272\,\mathrm{ns}$ [26] and promotes the donor-bound electron into the conduction band. At this particular time, the electron has lost its spin information resulting in an unpolarized free electron ensemble n_6. After the electron has relaxed its excess energy to the lattice (compare chapter 10.2) it is captured back into an ionized donor within the capture time τ_C. The number of ionized donors in thermal equilibrium in the sample is $n_{d,io} = 1 \times 10^{14}\,\mathrm{cm}^{-3}$ having equally distributed nuclear spins $|\Uparrow\rangle$ and $|\Downarrow\rangle$. Therefore, a high chance exists that the free electron is captured with equal probability into one of the donor states $n_1 - n_4$. While n_1 is constantly pumped, longitudinal spin relaxation denoted by the time T_1 (blue arrows) and the cross relaxation denoted by the time T_X (red arrow) distribute the population such that it mainly builds up in the states n_3 and n_4. This redistribution leads to an effective electron spin polarization of the donor ensemble. The cross relaxation time T_X traces back to the fact that $n_2 = |\uparrow\Downarrow\rangle$ and $n_3 = |\downarrow\Uparrow\rangle$ are not exact eigenstates of the donor system's Hamiltonian. Therefore, each ionization event provides a small probability of a spin flip with the relaxation time

$$T_X^{-1} = \sin\left(\Theta/2\right)^2 \times \left(G_2 + G_3\right), \tag{9.2}$$

where $\Theta = \arctan\left(A/(\gamma^+ B)\right)$ and γ^+ is the sum of the electron and nuclear gyromagnetic ratios [73].

In order to study this effect quantitatively, we have set up the corresponding coupled differential equations for the population of the donor states ($n_1 - n_4$), the D^{0}X (n_5), and the free electrons (n_6).

$$\begin{aligned}
\frac{d}{dt}n_1(t) &= -G_1 \cdot n_1(t) + \frac{n_6(t)}{4\cdot\tau_C} - \frac{n_1(t) - n_3(t)}{2\cdot T_1}, \\
\frac{d}{dt}n_2(t) &= -G_2 \cdot n_2(t) + \frac{n_6(t)}{4\cdot\tau_C} - \frac{n_2(t) - n_4(t)}{2\cdot T_1} - \frac{n_2(t) - n_3(t)}{2\cdot T_\mathrm{x}}, \\
\frac{d}{dt}n_3(t) &= -G_3 \cdot n_3(t) + \frac{n_6(t)}{4\cdot\tau_C} - \frac{n_3(t) - n_1(t)}{2\cdot T_1} - \frac{n_3(t) - n_2(t)}{2\cdot T_\mathrm{x}}, \\
\frac{d}{dt}n_4(t) &= -G_4 \cdot n_4(t) + \frac{n_6(t)}{4\cdot\tau_C} - \frac{n_4(t) - n_2(t)}{2\cdot T_1}, \\
\frac{d}{dt}n_5(t) &= G_1 \cdot n_1(t) + G_2 \cdot n_2(t) + G_3 \cdot n_3(t) + G_4 \cdot n_4(t) - \frac{n_5(t)}{\tau_A}, \\
\frac{d}{dt}n_6(t) &= \frac{n_5(t)}{\tau_A} - \frac{n_6(t)}{\tau_C}.
\end{aligned}$$

An exemplary solution to the coupled rate equations is depicted in Fig. 9.3 when the system is driven at the rates G_2 and $G_1 = 0.1 \times G_2$. This takes into account that even under resonant excitation conditions on n_2 there is still some residual absorption of n_1 due to the finite spectral width of the D^{0}X transition.

Figure 9.3 (a) illustrates the calculated steady-state polarization in a color-coded plot as a function of the two most important parameters, i.e., the longitudinal spin relaxation and the laser power[1] used to drive the system. The drastic change in polarization

---

[1] A laser spot radius of 225 µm is used for the calculation (see next chapter).

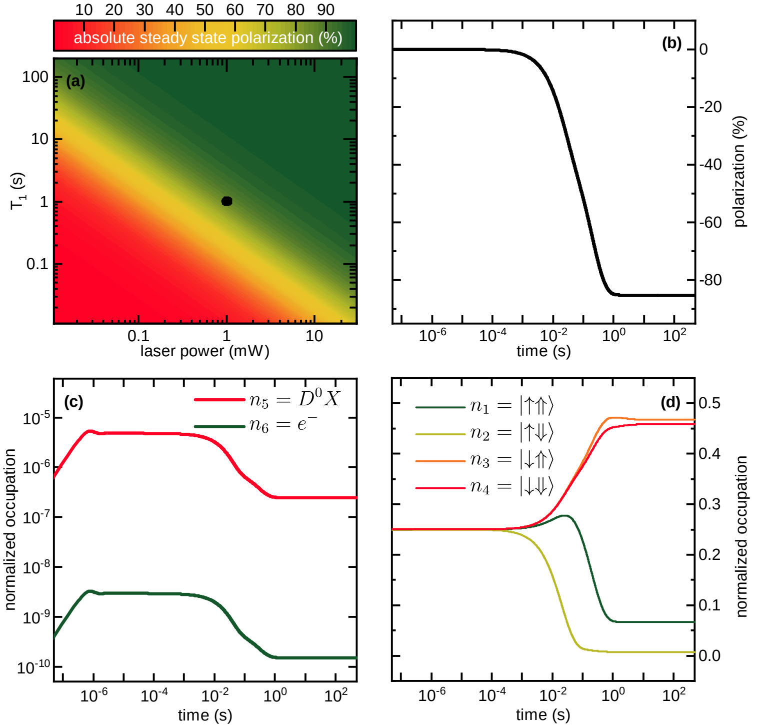

Figure 9.3: **(a)** Color-coded steady-state polarization as a function of spin relaxation time and laser power. **(b)** Transient build-up of donor polarization. **(c)** Transient occupation of D^0X (red line) and free electrons (green line). **(d)** Transient occupation of the four hyperfine-coupled donor states. The occupation in **(c)** and **(d)** is normalized to one donor.

inside the spanned parameter space confirms the importance of these two quantities and further suggests the extraction of the T_1 time from the steady-state polarization if the excitation conditions are exactly known.

Figure 9.3 (b) shows for a laser power of 1 mW and $T_1 = 1\,\mathrm{s}$ (black dot in (a)) the time evolution of the polarization which is calculated from the evolution of the donor states $n_1 - n_4$ depicted in Fig. 9.3 (d). Furthermore, the model grants access to the population of the D^0X state (n_5) and to the number of free Auger electrons (n_6) (cf. Fig. 9.3 (c)). Even though the steady-state number of free electrons normalized to one donor seems very low $\approx 1 \times 10^{-10}$, the resulting electron density of $\approx 1 \times 10^{5}\,\mathrm{cm}^{-3}$ is comparable to the density reported by Feher and Gere [11]. In their seminal publication they find that in a sample with donor doping density of $7 \times 10^{15}\,\mathrm{cm}^{-3}$ a free electron density of $5 \times 10^{5}\,\mathrm{cm}^{-3}$ reduces the spin relaxation time almost by a factor of ten.

10

TIME RESOLVED POLARIZATION DECAY

10.1 EXPERIMENTAL POLARIZATION DYNAMICS

In order to unambiguously study the effect of free electrons on the spin relaxation, we employ a two-color time-resolved pump-probe technique with two ECDLs. In contrast to sideband pump-probe spectroscopy, this allows for independent adjustment of the laser polarizations and enables time resolution by, e.g., amplitude modulation of the pump laser. Commonly, in two-color pump-probe spectroscopy, the area of the focused pump laser is larger than the area of the focused probe laser which allows to monitor a signal even if the two lasers are slightly offset or tilted towards each other. For the purpose of quantitative modeling, the beam parameters and their relative orientation must be known precisely. Therefore, a horizontal knife edge scan at the focal plane is performed for both lasers. The derivative of the result is depicted in Fig. 10.1 for the pump laser (left) and the probe laser (right). The red line is a Gaussian fit to the intensity profiles yielding a $1/e^2$ radius of 225(5) µm for the pump laser and 86(3) µm for the probe laser, respectively.
Optimal spatial overlap of the two lasers is achieved by establishing a common path on the optical table. The optical axes of the two lasers are then coarsely brought to coincidence with the aid of adjustable iris blinds. Fine tuning of the overlap is accomplished by maximizing the probe induced signal on the lock-in amplifier by slight adjustment of the pump path. When repeated iteratively, this procedure guarantees excellent spatial overlap between the focused probe and pump spot.

Furthermore, the probe laser is sideband modulated and detected by a fast lock-in amplifier which enables the superior signal-to-noise ratio of the derivative spectroscopy technique. An example of such a spectrum is shown in Fig. 10.2 for the pump laser fixed to the center of the doublet 9/10. The probe laser is scanned across the doublets 5/6 and 7/8 which are ideally suited to monitor the donor electron polarization due to the identical oscillator strength of the doublets.

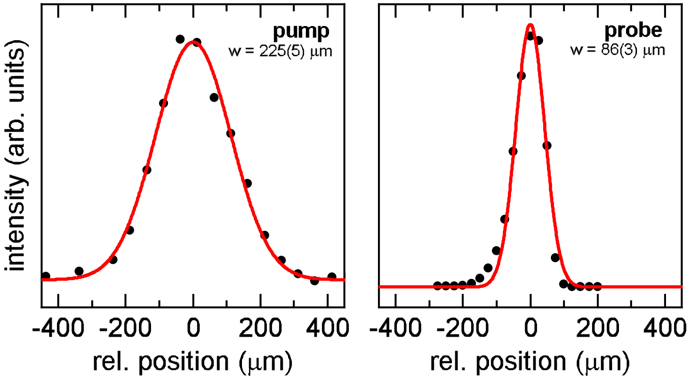

Figure 10.1: **(left)** Integrated horizontal knife edge scan of the pump laser. **(right)** Integrated horizontal knife edge scan of the probe laser. The red lines are Gaussian fits with w being the $1/e^2$ radius.

The red line is a cumulative fit to the data with a four Lorentzian line shape function and the extracted degree of polarization is $-68(1)\,\%$. The same degree of polarization is obtained if the polarization is just evaluated by the depicted differential absorption local extreme points α_5 to α_8. In the next step, the donor ensemble is prepared with the maximum degree of polarization and then the pump laser is shut off with a fast mechanical shutter (orange line in Fig. 10.3) which defines $t = 0$. With the continuously present probe laser, the time evolution of the polarization is now determined by measuring the time-resolved transient of one of the spectral positions α_i by the fast lock-in amplifier with a time resolution of $\approx 1.5\,\text{ms}$. If this procedure is repeated sufficiently often for all α_i, the donor electron polarization ρ_{exp} is calculated as

$$\rho_{exp} = \frac{(\alpha_5 + \alpha_6) - (\alpha_7 + \alpha_8)}{\sum_{i=5}^{8} \alpha_i}. \tag{10.1}$$

An example of such a time-resolved polarization decay is depicted in Fig. 10.3 as black dots. This clearly demonstrates that the steady-state polarization of $-68\,\%$ is reproduced for $t < 0\,\text{s}$ and $t > 100\,\text{s}$, i.e., when the pump laser is active. For $0\,\text{s} \leq t \leq 100\,\text{s}$, the time constant of the polarization decay is extracted by an exponential

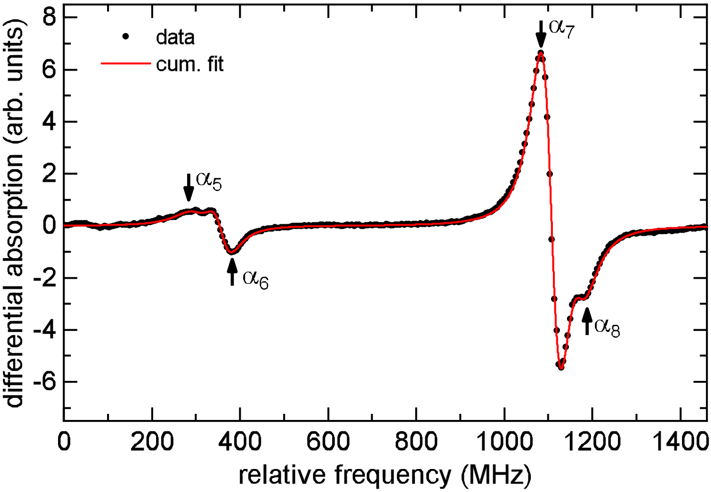

Figure 10.2: Typical differential probe absorption spectrum of the D^0X transitions 5 to 8. The black dots are measured and the red line is the corresponding line shape fit with four differential Lorentzians.

fit (red line) yielding excellent agreement.

In every optical pump-probe spectroscopy scheme, the optical power of the probe laser can have a detrimental impact on the measurement result. Therefore, we have investigated the time-dependent polarization decay for a variety of probe intensities ranging over three orders of magnitude. The extracted decay constants are shown in Fig. 10.4 as black dots. It is evident that for higher intensity, the probe laser itself depopulates the donor state of the corresponding transitions α_i which leads to a pronounced shortening of the polarization decay time. For decreasing intensity of the probe laser however, the polarization decay time rises and approaches its equilibrium value of 14 s which is the value for the longitudinal spin relaxation time T_1 at 4.5 K [22].
The dashed gray line is a simulation based on the rate equations with a constant spin relaxation time $T_1 = 14\,\mathrm{s}$. The calculation fully takes into account the measured absorption coefficients for the different spectral lines, the measured radii of the pump and probe laser at the focal plane and, most importantly, the experimental protocol used to obtain the experimental polarization time traces. Qualitatively,

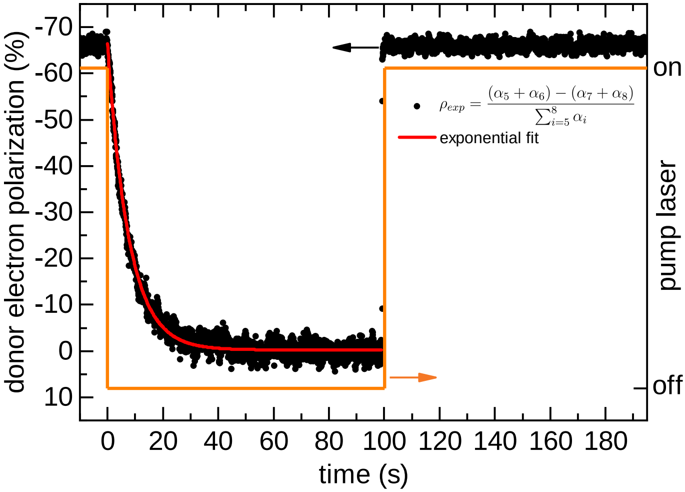

Figure 10.3: Time-resolved polarization decay of the donor ensemble (black dots). The decay constant is extracted by an exponential fit (red line) and the orange line illustrates the state of the pump laser.

the simulation reproduces the general trend of decreasing decay time with increasing probe power. Quantitatively however, the simulation systematically overestimates the decay time which is most pronounced for high probe power. Furthermore, the steady-state polarization calculated by the numerical model is around $-90\,\%$ throughout the whole range of applied probe intensities whereas the experimentally determined degree of polarization never exceeds $\approx -70\,\%$.

An inspection of the color-coded plot in Fig. 9.3 (a) reveals that for constant probe power the only possibility of reducing the steady-state polarization as well as the polarization decay time, is a shortening of the spin lattice relaxation time T_1. As already stated earlier, such a shortening can be caused by the interaction of donor electrons with free electrons which stem, in the current case, from the Auger recombination of the D^0X.

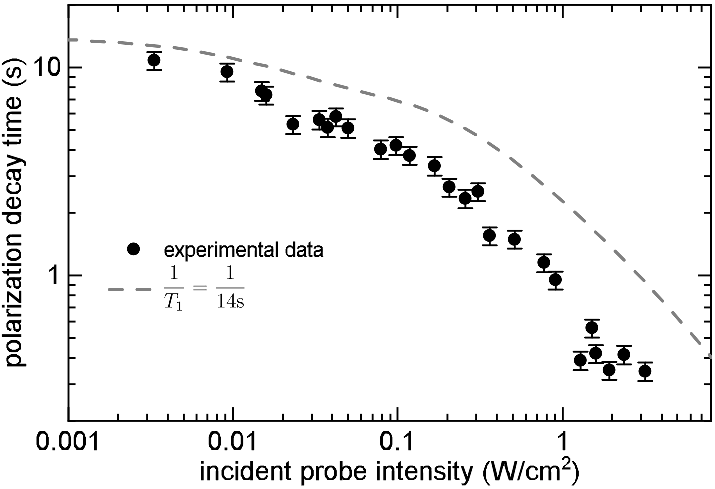

Figure 10.4: Measured polarization decay time in dependence on optical probe intensity (black symbols). The dashed gray line is a simulation based on the numerical model with $T_1 = 14\,\mathrm{s}$.

10.2 A MICROSCOPIC PICTURE

The Auger electrons from the D^0X recombination start upon excitation with an initial excess energy of about 1.10(1) eV with respect to the conduction band minimum. The main idea for the shortening of the spin lattice relaxation time mediated by free electrons is that these high energy Auger electrons collide inelastically with donor bound electrons in the 1S-A_1 ground state and promote the bound electrons to the excited donor 1S-T_2 state. As outlined in chapter 2.4, the thermal population of the spin-mixed T_2 state is the cause for the Orbach spin lattice relaxation which decreases the spin lattice relaxation time exponentially with increasing temperature. Since the temperature stays constant throughout our experiments, the proposed mechanism can be thought of as an Orbach-type relaxation mechanism which causes an increase in the relative T_2/A_1 population not by temperature but rather by inelastic collisions with free, hot conduction band electrons.

However, inelastic scattering between free and bound electrons is not the only way for hot electrons to relax their excess energy towards the band minimum. Interaction with the lattice via phonons has also to be taken properly into account in order to determine if inelastic scattering is an efficient energy relaxation channel. The electron density in the conduction band, n_6, resulting from the D^{0}X Auger recombination depends on the laser intensity and the capture time τ_c and ranges in the current case between $n_6 \approx 3 \times 10^3\,\mathrm{cm}^{-3}$ and $n_6 \approx 1 \times 10^5\,\mathrm{cm}^{-3}$. The corresponding electron-electron scattering rates can be roughly approximated by $10^{-5}\,\mathrm{cm}^{-3}\,\mathrm{s}^{-1} \times n_6$ [74] and are therefore negligible in comparison to all other relevant scattering rates, i.e., the conduction band electrons do not thermalize by electron-electron scattering. On the one hand, energy relaxation of hot conduction band electrons is governed by $g-$ and $f-$type scattering by TO, LO, and LA phonons which can be calculated for low lattice temperatures by [74]

$$\left(\frac{dE}{dt}\right)_{inter} = \frac{Z_i (D_t K)_i^2 m_e^{3/2}}{\sqrt{2}\pi\hbar^2\rho} \tilde{N}_q \sqrt{E-\epsilon_i}, \tag{10.2}$$

where $(D_t K)_i$ is the interband deformation potential for the phonon type i with energy ϵ_i, $\tilde{N}_q = N_q + 1$ is the phonon occupation number, and ρ is the density of the crystal. The factor Z_i is either 1 for $g-$type scattering or 4 for $f-$type scattering. The emission of optical phonons takes place on a sub 100 fs timescale and is completed after about 2 ps. We further include first order scattering by so called 190 K acoustic phonons with $\epsilon_1 = k_B 190\,K$ [75] by the energy relaxation rate

$$\left(\frac{dE}{dt}\right)_{inter,1} = \frac{\Xi_1^2\,(2 \cdot m_e)^{5/2}}{2\pi\hbar^4\rho} \tilde{N}_q \sqrt{E-\epsilon_1} \cdot \left(E - \frac{\epsilon_1}{2}\right). \tag{10.3}$$

After about 2 ps the energy loss is governed by two concurring processes. The first one is intravalley scattering with acoustic phonons with the corresponding rate

$$\left(\frac{dE}{dt}\right)_{intra} = \frac{\Xi_0^2\,(2 \cdot m_e)^{5/2}}{2\pi\hbar^4\rho} \cdot E^{3/2}, \tag{10.4}$$

where Ξ is the intraband acoustic deformation potential. The second mechanism is inelastic scattering of the electrons with neutral impurities where the conduction band electrons excite the D^0 1S-A$_1$ to T$_2$ transition. This is the relevant transition for the Orbach-type process. The energy relaxation rate due to collisions can be approximated by

$$\left(\frac{dE}{dt}\right)_{coll} = -\frac{\Delta}{\tau_{coll}(t)}, \tag{10.5}$$

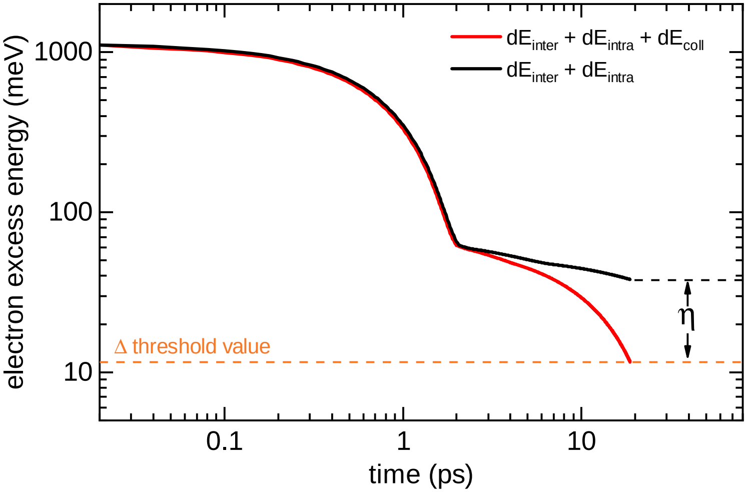

Figure 10.5: Calculated dynamics of the hot Auger electrons after excitation into the conduction band. The D^0X Auger recombination defines $t = 0$. The red line depicts the calculated cooling dynamics including all relevant cooling mechanism. The black line shows the same but without inelastic D^0 scattering.

for $E \geq \Delta$ and zero otherwise. Here, Δ is the D^0 1S-A$_1$ to T$_2$ transition energy. The collision rate $\tau_{coll}^{-1}(t)$ is defined as

$$\frac{1}{\tau_{coll}(t)} = \sigma_{coll} \cdot v(E) \cdot n_d, \tag{10.6}$$

where $\sigma_{coll} = 8 \times 10^{-12}$ cm^2 is the collision cross section between free electrons and neutral P-donors [76] and $v(E)$ is the energy-dependent velocity of the conduction band electrons calculated by the parabolic band approximation. The red line in Fig.10.5 shows the energy relaxation dynamics including intravalley scattering, intervalley scattering, and inelastic collisions with donors. After about 19 ps, the energy of the Auger electrons falls below the transition energy Δ, i.e., the energy of the conduction band electrons is not sufficient anymore for inelastic scattering with localized donor electrons involving the 1S-A$_1$ to 1S-T$_2$ transition. At this particular time, the energy fraction lost by the electron from its initial excess energy by inelastic collisions with donors amounts to $\eta = 26.4$ meV, i.e., each Auger electron excites according to this unpretentious

$(D_tK)_{g,LO}$	$11 \times 10^8\,\mathrm{eV\,cm^{-1}}$	[77]
ϵ_{LO}	$62.0\,\mathrm{meV}$	[77]
$(D_tK)_{g,LA}$	$2 \times 10^8\,\mathrm{eV\,cm^{-1}}$	[77]
ϵ_{LA}	$47.4\,\mathrm{meV}$	[77]
$(D_tK)_{f,T0}$	$2 \times 10^8\,\mathrm{eV\,cm^{-1}}$	[77]
ϵ_{TO}	$59.0\,\mathrm{meV}$	[77]
Ξ_0^2	$9\,\mathrm{eV}$	[77]
Ξ_1^2	$5.6\,\mathrm{eV}$	[75]
n_d	$1.2 \times 10^{15}\,\mathrm{cm^{-3}}$	
$n_{d,i}$	$1 \times 10^{14}\,\mathrm{cm^{-3}}$	

Table 10.1: Parameters for the calculation of the Auger electron cooling dynamics.

calculation on average $\zeta = \eta/\Delta = 2.3$ 1S-A$_1$ to 1S-T$_2$ donor transitions. The constants used to calculate the electron energy loss dynamics are summarized in table 10.1.

After having established that inelastic scattering between free and bound electrons is an effective energy relaxation channel, we consider next the transition from the 1S-A$_1$ to 1S-T$_2$ donor state as an ideal two-level system. Let n_{T_2} be the population of the excited state and n_{A_1} the population of the ground state. From a thermodynamic point of view, the relative population of the two states is given by

$$\frac{n_{T_2}}{n_{A_1}} = \exp\left(-\frac{\Delta}{k_B T}\right). \tag{10.7}$$

On the other hand, the relative population can also be expressed in terms of the Orbach-type process which is illustrated in Fig.10.6 (left). From the numerical model, the electron rate falling back to one donor from the conduction band is given by $\frac{n_6}{\tau_c n_d}$. This quantity has to be multiplied by ζ, i.e., the number of inelastic collisions one electron undergoes. This comprises the complete excitation rate from the ground state to the excited state. Unfortunately, the downwards relaxation time is not known which is owed to the fact that the 1S-A$_1$ to 1S-T$_2$ transition is not optically active. A solution to this problem has already been given by Castner in his

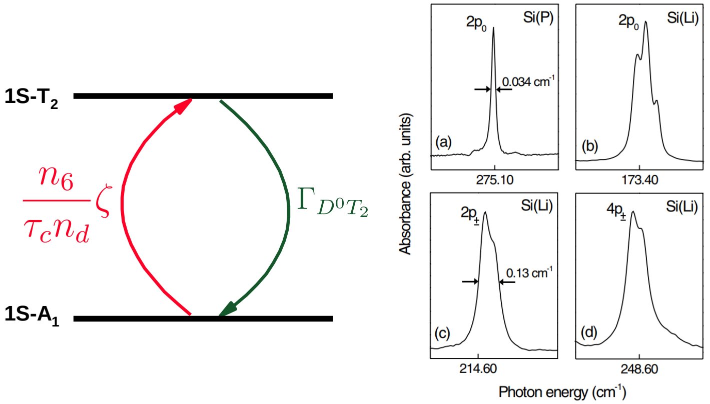

Figure 10.6: **(left)** Two-level scheme of the excitation and relaxation processes responsible for the Orbach-type spin relaxation. **(right)** Absorption spectra of exited donor states. Taken from Ref. [78].

original publication on spin relaxation of bound electrons [31]. As an estimate for the decay rate of the 1S-T$_2$ he uses the spectral width extracted from the dipole allowed 2P$_0$ to 1S-A$_1$ transition. The corresponding data for isotopically enriched silicon have been obtained by Karaiskaj et. al. [78] and is depicted in Fig.10.6 (right a). When the homogeneous linewidth of $0.034\,\mathrm{cm}^{-1}$ is expressed in frequency units, we arrive at the quantity for the 1S-T$_2$ decay rate which amounts to $\Gamma_{D^0T_2} = 1.02\,\mathrm{GHz}$. The expression for the T$_2$/A$_1$ population then reads

$$\frac{n_{T_2}}{n_{A_1}} = \frac{n_6}{\Gamma_{D^0T_2}\tau_c n_d}\zeta. \tag{10.8}$$

Comparing Eqs. 10.7 and 10.8 with Castner's formula for the Orbach spin lattice relaxation

$$\frac{1}{T_1} = E_0 \times \exp\left(-\frac{\Delta}{k_B T}\right), \tag{10.9}$$

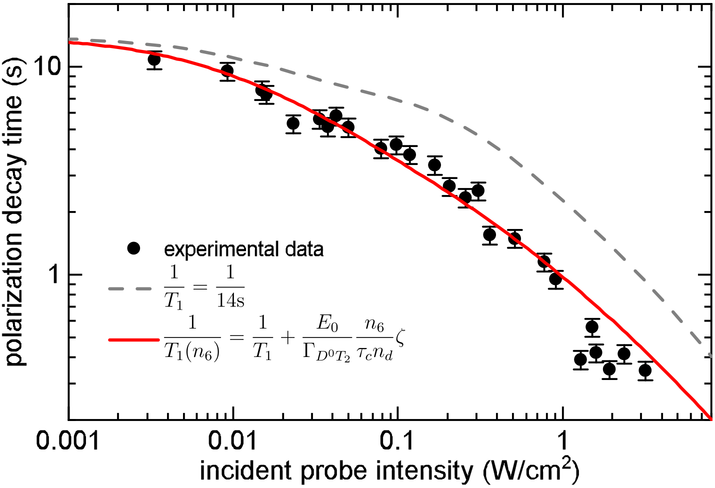

Figure 10.7: Measured polarization decay time in dependence on optical probe intensity (black symbols). The dashed gray line is a simulation based on the numerical model with $T_1 = 14\,\mathrm{s}$. The solid red line is calculated including the Orbach-type process due to hot Auger electrons (see Eq. 10.11).

we immediately find a universal expression for the Orbach spin lattice relaxation as a function of temperature T and conduction band electron density n_6

$$\frac{1}{T_1\left(T, n_6\right)} = E_0\left(\exp\left(-\frac{\Delta}{k_B T}\right) + \frac{n_6}{\Gamma_{D^0T_2}\tau_c n_d}\zeta\right). \tag{10.10}$$

For a constant temperature, Eq. 10.10 reduces to

$$\frac{1}{T_1\left(n_6\right)} = \frac{1}{T_1} + \frac{E_0}{\Gamma_{D^0T_2}}\frac{n_6}{\tau_c n_d}\zeta, \tag{10.11}$$

where T_1 is just the intrinsic spin relaxation time at a given temperature.

Figure 10.7 shows a reexamination of the polarization decay times as function of the incident probe intensity. For comparison, the dashed gray line is again the solution to the numerical model with $T_1 = 14\,\mathrm{s}$. The solid red line is a fit to the data with the spin lattice relaxation depending on n_6 according to Eq. 10.11 which yields $\zeta = 3.2$ as the only free fit parameter. This value is in surprisingly good agreement with the value of $\zeta = 2.3$ estimated from the

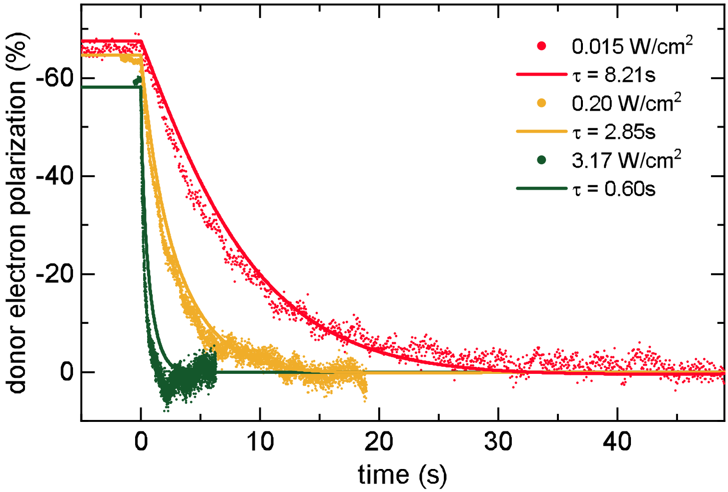

Figure 10.8: Temporal change of the initial D^0 polarization after the pump laser is turned off at $t = 0\,\mathrm{s}$ for different probe intensities (colored dots). The corresponding solid lines are the results of the numerical model including the dependence of T_1 on excitation density.

electron cooling dynamics. Furthermore, our model does not only calculate the correct polarization decay times but also reproduces the steady-state polarization quite accurately which is shown in Fig. 10.8. Here, we show as colored dots three exemplary experimental polarization decays representing the whole range of measured probe intensities. The solid lines are the corresponding solution of the numerical model with $\zeta = 3.2$. At this point it is worth emphasizing that no other adjustable parameters are needed to account for the polarization dynamics.

The parameter ζ, i.e., the number of 1S-A_1 to 1S-T_2 donor transitions excited by a single Auger electron, is expected to be universally valid for P-donors in n-type silicon for doping densities well below the metal-to-insulator transition. Deviations are expected for p-type samples because our model does not account for electron energy relaxation via scattering with acceptors.

Part VI

OUTLOOK AND SUMMARY

ABSTRACT PART VI

This final part lays the foundation for practicable future experiments on donor bound excitons in ^{28}Si. It is quantitatively shown that the inherent weakness of the D^0X absorption represents a major challenge for the detection of optical spin noise in this system which may be overcome by application of an optical cavity in order to enhance the spin noise signal.

On the basis of the dynamics of the optically driven donor system presented in part V, a simple detection scheme for optically injected, spin-polarized conduction band electrons based on the high spin selectivity of the D^0X transition is introduced. Unlike other detection schemes such as Hanle depolarization of photoluminescence, the proposed experiment is capable of detecting the instantaneously induced spin polarization in the conduction band since it relies on the fast capture of polarized electrons into ionized donor states which takes place on the ps timescale for moderately doped p-type samples.

11

OUTLOOK

11.1 SPIN AND OCCUPATION NOISE SPECTROSCOPY

Spin Noise Spectroscopy (SNS) is an effective tool for probing the spin dynamics of the underlying system in thermal equilibrium. It does not rely on the generation of a non-equilibrium spin distribution (compare, e.g., Refs. [79, 80]) but rather monitors the inherent spin fluctuations of the system which carriers the same information as if the system was externally perturbed [81]. After being established in solid state systems in 2005 [82] the sensitivity of the technique has rapidly improved which allowed for SNS in low dimensional systems such as semiconductor quantum wells [83] and the ultimate limit of a single hole spin located in a (InGa)As quantum dot (QD) [84]. However, all of these experiments were performed on direct gap semiconductors and a demonstration of SNS in an indirect semiconductor such as silicon is still lacking.

The general idea of SNS is straightforward as outlined in Ref. [85] and illustrated in Fig. 11.1. Linearly polarized light is transmitted through the sample where the optical frequency of the laser is adjusted such that it only weakly interacts with the resonance under

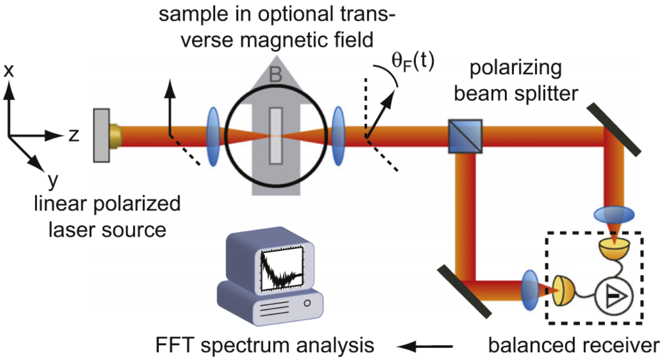
sample in optional trans-
verse magnetic field
B
$\theta_F(t)$
polarizing
beam splitter
x
z
y
linear polarized
laser source
FFT spectrum analysis
balanced receiver

Figure 11.1: Schematic experimental setup for spin noise spectroscopy. Taken from Ref. [85].

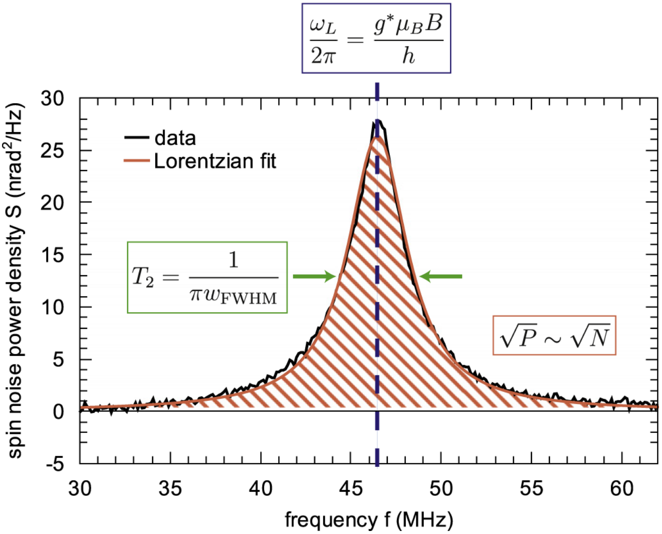

Figure 11.2: Exemplary spin noise spectrum of conduction band electrons in GaAs. Taken from Ref. [85].

investigation. Since the probed spin ensemble has a finite size, the average spin polarization m_z vanishes but the standard deviation is non-zero with

$$\sigma_{m_z} = \sqrt{N}/N, \tag{11.1}$$

where N is the number of probed states, i.e., the number of probed donor electrons in this case. This momentary spin imbalance leads to a difference in absorption for σ^+ and σ^- light and thus, via the Kramers-Kronig relations [86], translates into a difference of the dispersive part of the respective refractive indices. This effectively leads to a Faraday rotation [42] of the linearly polarized probe laser which is resolved via a polarization bridge and detected by a balanced photo receiver in the time domain. A spectral analysis of the fluctuating Faraday rotation signal reveals the spin noise spectrum which is shown in Fig. 11.2 for free electrons in bulk GaAs. The key to obtain such a spin noise spectrum lies in the efficient averaging of other noise sources, i.e., photon shot noise and electrical noise of the detector, which might be orders of magnitude larger than the spin noise signal. This can be achieved by subtracting two different spectra, one without magnetic field and one with a finite magnetic field which causes the electrons to precess with the Lamor frequency

ω_L. This difference spectrum exhibits a Lorentzian shape centered around ω_L where the FWHM is inversely proportional to the spin decoherence(dephasing) time T_2 of the system.
In order to examine the feasibility of SNS in silicon the $\mathrm{D}^0\mathrm{X}$ resonance is represented by the Drudel-Lorentz model [50]. In the framework of this model, the dissipative part of the refractive index, and thus the absorption coefficient α is given by

$$\alpha = \kappa \frac{2\omega}{c_0} = \frac{e^2 f n_D}{8m\epsilon_0\omega_x\sqrt{\epsilon_B}} \frac{\Gamma_0}{(\omega-\omega_x)^2+\Gamma_0^2/4} \frac{2\omega}{c_0}, \tag{11.2}$$

where f is the oscillator strength of the transition, ω_x is the resonance frequency of the $\mathrm{D}^0\mathrm{X}$ and Γ_0 is the width of the transition. The respective dispersive part of the refractive index n reads

$$n = n_B + \widetilde{n} = \sqrt{\epsilon_B} - \frac{e^2 f n_D}{8m\epsilon_0\omega_x\sqrt{\epsilon_B}} \frac{\omega-\omega_x}{(\omega-\omega_x)^2+\Gamma_0^2/4}, \tag{11.3}$$

where $n_B = \sqrt{\epsilon_B}$ arises from the static dielectric background. At this point it is very important to restate that a spin noise signal can only occur if there exists a finite circular dichroism, i.e.,

$$\Delta\alpha = \alpha^+ - \alpha^- \neq 0 \tag{11.4}$$

and a finite circular birefringence

$$\Delta n = n^+ - n^- \neq 0 \tag{11.5}$$

which can cause a non-zero Faraday angle

$$\Theta_F = \frac{\pi\Delta n\cdot l}{\lambda_0}, \tag{11.6}$$

where l is the thickness of the sample along the propagation of light. Together with Eq. 11.1 this leads to an expression for the squared fluctuation of the Faraday rotation angle which is more conveniently termed the integrated spin noise power P:

$$P = \sigma^2_{\Theta_F} = \frac{\pi^2\Delta n^2 l}{\lambda_0^2 n_D A}, \tag{11.7}$$

where $A = \pi w_0^2$ is the area of the focused probe laser. In $^{28}\mathrm{Si}:\mathrm{P}$ the criteria for circular dichroism/birefringence are more complicated due to the $\mathrm{D}^0\mathrm{X}$ narrow linewidth and the $\mathrm{D}^0\mathrm{X}$ optical selection rules (compare Fig. 2.6). The only possibility to meet these criteria is the

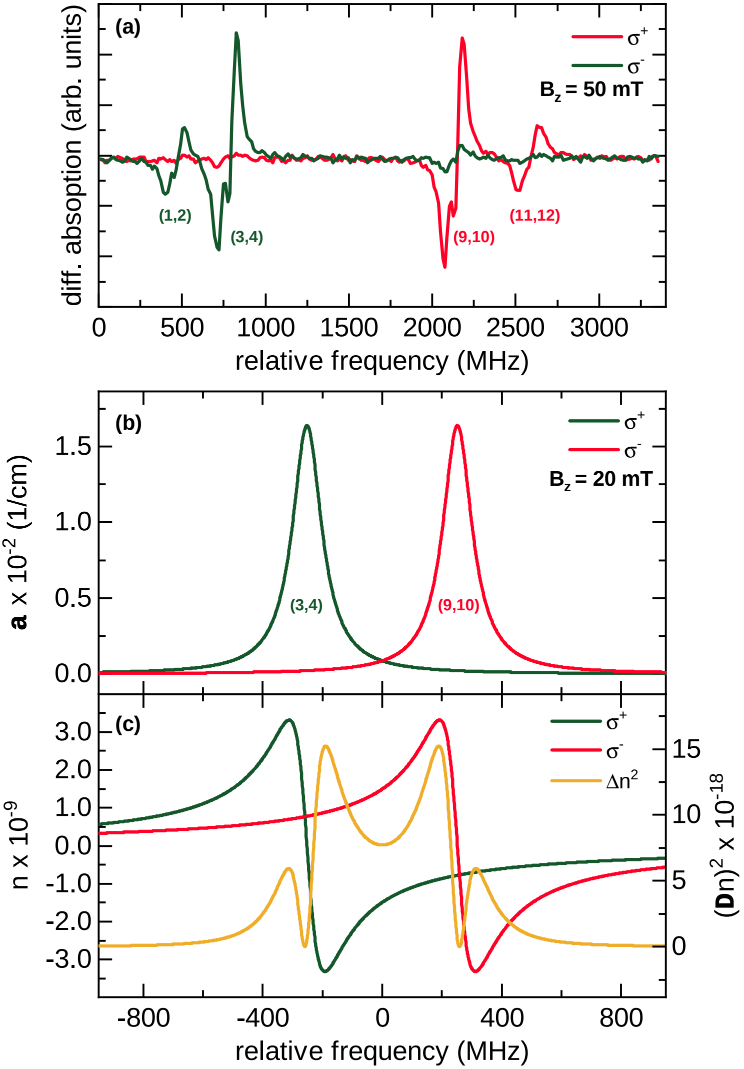

Figure 11.3: **(a)** Experimental illustration of circular dichroism of the D^0X transition in a longitudinal magnetic field. **(b)** Dissipative part of the refractive index for doublets $(3, 4)$ and $(9, 10)$. **(c)** Dispersive part of the refractive index for the same doublets as in (b) together with the squared differences (orange line).

application of a magnetic field parallel to the propagation of light, i.e., the z-direction. Fig. 11.3 (a) demonstrates the circular dichroism for a magnetic field of $B_z = 50\,\mathrm{mT}$ where the dark green line denotes σ^- transitions and the red line denotes σ^+ transitions. In order give a quantitative estimate of the spin noise power we consider only the doublets (3,4) and (9,10) and model the absorption coefficient according to Eq. 11.2 where each doublet is represented by a single resonance with a slightly larger FWHM. The Zeeman shift of the respective transitions is properly taken into account by using the Landé factors found in chapter 8.2 and the oscillator strength f is adjusted to match experimentally determined absorption coefficient. This leads to the spectrum depicted in Fig. 11.3 (b) for a magnetic field of 20 mT. The dispersive part of the refractive index is easily calculated using Eq. 11.3 which is displayed in Fig. 11.3 (c - left axis). The orange line shows the squared difference of the latter which amounts to

$$\Delta n^2 = \left(n^+ - n^-\right)^2 \approx 8 \times 10^{-18} \tag{11.8}$$

at zero relative frequency. Inserting this into Eq. 11.7 yields

$$P \approx 1 \times 10^{-20}\,\mathrm{rad}^2. \tag{11.9}$$

In order to be useful for comparison with other experiments, the signal strength η has been introduced which is the nothing else but the peak of the integrated spin noise power density divided by the photon shot noise and is defined as [85]

$$\eta = \frac{P T_2 P_{laser}}{\hbar\omega_{laser}}, \tag{11.10}$$

where P_{laser} is the incident laser power and $\hbar\omega_{laser}$ the photon energy of the laser. Assuming $P_{laser} = 1\,\mathrm{mW}$ and $T_2 = 100\,\mathrm{ms}$ [1] yields for the signal strength of donor bound electrons in $^{28}\mathrm{Si}$

$$\eta_{Si} \approx 3.3 \times 10^{-5}. \tag{11.11}$$

This quantity can directly be compared to the data on SNS of a single hole spin in a QD. From Ref. [87], the relevant parameters can be extracted which gives an estimate for the signal strength. With $P_{laser} \approx 1\,\mu\mathrm{W}$, $T_1 \approx 3.3\,\mu\mathrm{s}$ and $P \approx 9 \times 10^{-10}$ we have

$$\eta_{QD} \approx 2 \times 10^{-2}. \tag{11.12}$$

---

[1] This value is an upper estimate for spin decoherence time. Unavoidable inhomogeneities in the external magnetic field give rise to a much shorter inhomogeneous spin dephasing time T_2^*.

This comparison clearly demonstrates that SNS in silicon is by no means an easy task if the weak signal strength can not be improved. A first approach to this may be placing the sample inside a cavity since the number of photon round trips N_r will directly increase the effective sample length $l_{eff} = lN_r$. An "external" cavity at the position of the focusing/collimating lenses is not an option because the accumulated reflection loses of the cryostat windows prohibit an efficient power buildup. Another possibility is a distributed Bragg reflector (DBR) grown on the sample surface. However, from a basic estimate of the cavity parameters, the following problem arises[2]. A cavity length of $l = 4\,\mathrm{mm}$ in a dielectric environment of $n_B = \sqrt{\epsilon_B} \approx 3.42$ exhibits a FSR of

$$\Delta_{FSR} = \frac{c}{2n_B l} \approx 10.9\,\mathrm{GHz}. \tag{11.13}$$

On the other hand, the number of round trips should be as high as possible in order to increase the spin noise power. This poses another difficulty since N_r is inversely proportional to the transition width $\delta\nu$ of the cavity. For $N_r = 100$, $\delta\nu$ only amounts to $\approx 35\,\mathrm{MHz}$ which corresponds to a finesse of $\mathcal{F} \approx 311$. This means that without precise knowledge of the cavity length, there is a chance of $\approx (1 - 1/\mathcal{F})$ that the desired probe frequency for SNS is not transmitting. The only remaining possibility is the implementation of a scanning Fabry Perot Cavity inside the cryostat where one of the mirrors can be displaced by a piezo actuator. Therefore the experiment has to be moved to a bath cryostat because the rigid construction of the home-built helium reservoir for the closed cycle refrigerator does not allow for moving parts (compare chapter 3.3). As a practical constraint to the cavity parameter, we advise that the width of the cavity resonance δ_ν should be on the order of $5\,\mathrm{MHz}$ which still allows phase modulation spectroscopy with $\Omega \approx 2\,\mathrm{MHz}$. This pins the mirror reflectivities to $R = 99.8\,\%$ for a conveniently chosen cavity length $l_{cav} = 20\,\mathrm{mm}$[3]. Furthermore, the sample surface has to be anti-reflection coated to at least $99.5\,\%$ in order to keep the intra-cavity losses Z_{intra} as small as possible. This yields the following cavity parameters

---

[2] Other difficulties can arise from strain inside the sample induced by the DBR growth process.

[3] Scanning of the $\mathrm{D^0X}$ in this case needs to be performed such that the carrier frequency is always located at the maximum transmission of the sample cavity. This can be achieved by either performing a PDH lock of the laser to the sample cavity or by carefully calibrating the voltages used to drive the laser frequency and the cavity piezo.

$$\begin{aligned} \Delta_{FSR} &\approx 2.2\,\text{GHz} && (11.14)\\ \delta_{\nu} &\approx 5\,\text{MHz} && (11.15)\\ N_r &\approx 330. && (11.16) \end{aligned}$$

This is a very promising estimate because a cavity with the above parameters would boost the spin noise signal strength to

$$\eta_{Si,cavity} \approx 1.1 \times 10^{-2}, \tag{11.17}$$

which is the same magnitude as the signal from a single QD.

Besides the detection of optical spin noise, which might be feasible in the near future, the uniquely narrow optical linewidth of the D^0X in isotopically enriched silicon offers the possibility to gain insight into the underlying spin dynamics of the system by monitoring the statistical fluctuation in the occupation of a distinct donor level, i.e., occupation noise. This is illustrated in Fig. 11.4 where the doublets $(1,2)$ and $(11,12)$ are shown for a magnetic field of $B_z = 20\,\text{mT}$. If the doublet $(1,2)$ is addressed with σ^+ light at the position indicated by the dashed line, there will be a non-zero absorption signal a^+ which is proportional to the occupation of the $|\uparrow\rangle$ donor state. The fluctuation of this signal σ_{a^+} is determined by the photon shot noise of the laser, the electrical noise of the photo detector and the occupation noise of the respective donor level. The latter consists of a contribution related to photon shot noise because the probed donor level is depopulated by the incident laser and another contribution which is related to internal processes such as longitudinal spin relaxation. In order to unambiguously identify the noise contribution belonging to T_1 spin relaxation, it is not sufficient to solely probe the $|\uparrow\rangle$ state via the doublet $(1,2)$. Instead, a two-color experiment is proposed where also the opposite spin state $|\downarrow\rangle$ with absorption signal a^- is probed via the doublet $(11,12)$ (red line in Fig. 11.4). Since the number of donor electrons in the sample is constant, the occupation of $|\uparrow\rangle$ and $|\downarrow\rangle$ are linked by the correlator

$$\langle a^+(t)a^-(t)\rangle \neq 0. \tag{11.18}$$

The recommendation for the detection setup and the measurement protocol is as follows: The two exiting beams from the sample are first subjected to a quarter wave plate which transforms the two

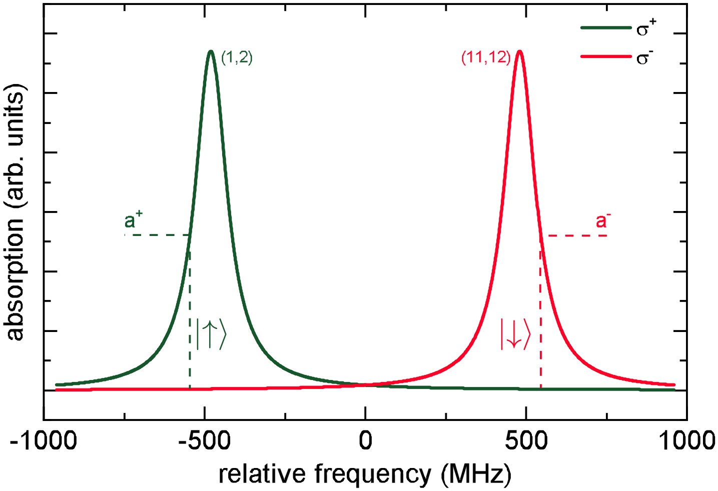

Figure 11.4: Calculated absorption spectra of D^0X for doublets $(1, 2)$ and $(11, 12)$. The dashed lines indicate a potential spectral probe positions for correlation spectroscopy where the amplitude $a^+(a^-)$ corresponds to $|\uparrow\rangle$ $(|\downarrow\rangle)$.

circular components into two orthogonal linearly polarized components which are spatially separated by a polarizing beam splitter and directed onto the two photo diodes of a balanced photo receiver. The elimination of the spurious noise contributions may be achieved by subtracting two noise spectra where the power of the two lasers is sufficiently higher for one of the spectra which leads to a pronounced shortening of the T_1 relaxation which was demonstrated in chapter 10. Therefore, the FFT difference signal from such an experiment consists of the difference of two Lorentzians centered around zero frequency with different widths.

The inherently long spin relaxation time in silicon at low temperatures pins the width of the noise spectra and the absolute frequency to the sub-kHz regime. In this regime, laser frequency noise is very pronounced (compare chapter 6) and the ultra narrow linewidth of the D^0X may translate this frequency noise into amplitude noise which represents another spurious noise contribution. This is quantified by a simple experiment which is outlined by the D^0X absorption spectrum at zero magnetic field in Fig. 11.5 (a). The absorption signal for different detunings of the D^0X transition is measured in a homodyne configuration where the beam that passes through

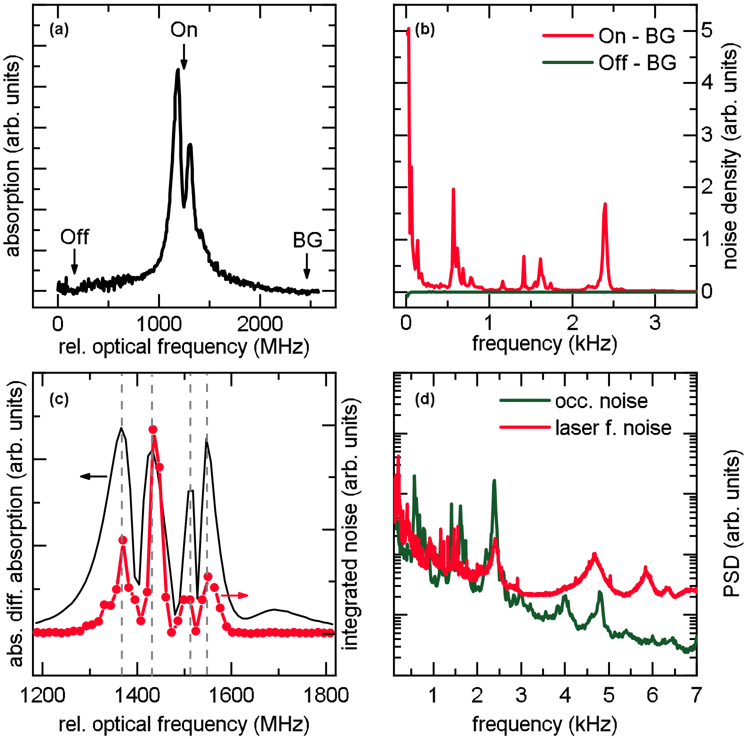

Figure 11.5: **(a)** Zero field D^0X spectrum with indicated positions for off resonant (Off), on resonant (On), and background (BG) spectral positions. **(b)** Low frequency difference spectrum for On-BG (red line) and Off-BG (green line). **(c)** Comparison between the absolute value of the differential absorption (black line) and the integrated noise power (red dotted line). The gray dashed lines indicate the maxima of the differential absorption. **(d)** Comparison between occupation noise (green line) and laser frequency noise power spectrum (red line).

the sample is compared against a reference beam (compare Fig. 3.4). For every detuning a background spectrum (BG) is subtracted which is taken at a far detuned spectral position. Consequently, the difference between an off-resonant spectrum (Off) and the background yields a perfect baseline as evidenced by the green line in Fig. 11.5 (b). The red line in (b) shows a typical spectrum on resonance which exhibits pronounced and spectrally narrow peaks. A straightforward way to clarify whether these peaks are footprints of the underlying donor system or measurement artifacts due to laser frequency fluctuation is to consider the integrated noise for different detunings. This is depicted in Fig. 11.5 (c) as red dots (right axis). The black line (left axis) shows the absolute value of the derivative of the absorption lineshape. Clearly, the position of the maxima and minima coincide quite well which favors the interpretation of laser frequency noise mediated by the dissipative medium. [4] Furthermore, Fig. 11.5 (d) also supports this conclusion where a typical on-resonance noise spectrum (green line) is compared against the frequency noise spectrum of the laser as determined in chapter 3.4. From the above considerations it follows that an occupation noise signal with a spectral width $< 1\,\mathrm{kHz}$ centered around the frequency origin, i.e, $0\,\mathrm{Hz}$ would be highly masked by this effect. This suggests that any experiment regarding the occupation noise of a certain donor level has to be carried out with the laser locked to the high finesse optical cavity presented in part III of this work where the laser frequency noise PSD[5] is suppressed by up to 14 orders of magnitude.

---

[4] Any signal which monitors the occupation of a donor level has to be proportional to the absorption. On the other hand, laser frequency noise is most pronounced where the change of the absorption spectrum is biggest, i.e., the maximum of the derivative.

[5] in $\mathrm{Hz}^2\,\mathrm{Hz}^{-1}$

11.2 OPTICAL SPIN INJECTION AND DETECTION

Optical spin injection in semiconductors denotes the creation of a finite electron spin polarization in the conduction band by exploiting the optical selection rules and is a key concept in spintronics [3]. The relatively simple optical selection rules for direct gap semiconductors such as *GaAs* render optical spin injection in those materials a routine task. The same holds for the detection of the spin polarization where important parameters such as the spin dephasing or the spin relaxation rate can be extracted by means of, e.g., Hanle depolarization of photoluminescence in an external magnetic field [88].

In silicon however, the optical selection rules for spin injection via the indirect bandgap are non-trivial. They have been calculated by Cheng. et al. [89] by *using an empirical pseudopotential description for the electron states and an adiabatic bond charge model for phonon states.* Fig. 11.6 shows as red dots the main result of this calculation, i.e., the degree of spin polarization (DSP) in the silicon conduction band caused by excitation with σ^- light[6] as a function of the excitation wavelength. The peculiar, non-monotonic dependence of the DSP is a result of the different phonon contributions and demonstrates that a DSP of $\approx -25\,\%$ is possible at a excitation wavelength of $\lambda_{max} \approx 1044\,\mathrm{nm}$. However, the efficiency of spin injection this close to the bandgap is not very large due to the decreasing absorption coefficient which has been measured by McFarlane et. al. [90] (green dots in Fig. 11.6). Despite the fact that the first demonstration of optical orientation in semiconductors has been achieved in silicon [79], the detection of the DSP is difficult due to the very weak photoluminescence signal which causes extremely long integration times in Hanle depolarization experiments [91, 92] and until now, we are not aware of any experimental study confirming the depicted theoretical dependence of the DSP. In this context, the $\mathrm{D^0X}$ transitions in $^{28}\mathrm{Si:P}$ may provide a unique optical spin detector. The mechanism for detection relies upon the capture of polarized free electrons into the donor states which is elucidated by the following three gedankenexperiments:

1 In a two-color experiment where one laser is used to produce the DSP at λ_{max} and the other laser, with vanishing intensity, is used to probe the $\mathrm{D^0X}$ transition the detected polarization

---

[6] For excitation with σ^+ light the sign is reversed.

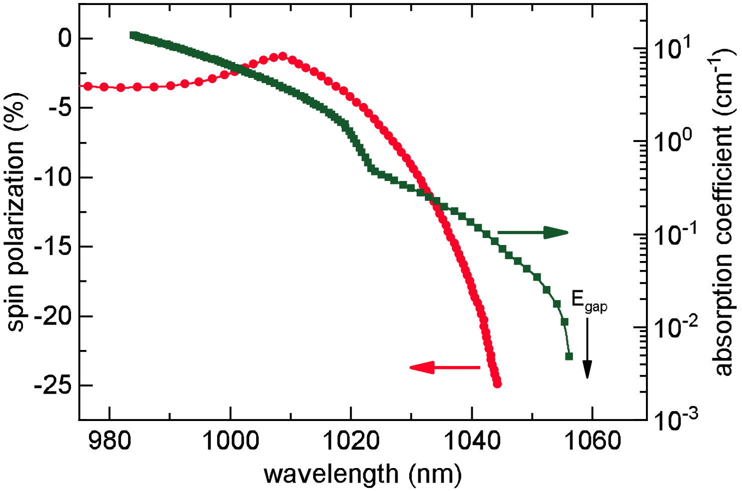

Figure 11.6: **(red)** Theoretical degree of spin polarization in silicon for excitation with σ^- light. Adapted from [89]. **(green)** Experimental absorption coefficient. Adapted from [90].

of the donor ensemble will still be $\rho = 0$ because the donors are fully occupied and no polarized conduction band electrons can be captured.

2 In a three-color experiment, two lasers are used to polarize the donor ensemble to $\rho = +\rho_0$ according to the spin pumping mechanism discussed in part V. The third laser at λ_{max} excites spin polarized electrons with a polarization $\pm\rho_1$ if the helicity of the laser is altered. Due to the spin pumping of the donors, the donor levels are not fully occupied at a given time and polarized electrons may be captured which should change the resulting donor polarization to $\rho = \rho_0 \pm \rho_1$. Two limiting cases can be distinguished. First, the intensity of the laser used for the free electron DSP is much weaker than the donor pump laser. In this case, the change in donor polarization due to the capture of polarized electrons is too weak to be detected. Second, the two laser intensities are of the same order of magnitude and the resulting number of polarized free electrons is large. In this case the huge number of free electrons will dramatically shorten the donor electron spin relaxation time T_1 via the Orbach-type relaxation which

results in a vanishing donor electron polarization. Both cases have been verified by numerical calculations throughout the whole parameters space of reasonable laser intensities which excludes the proposed three-color experiment for the detection of optical spin injection.

3 As a consequence of the first two points it seems likely that the donor states have to be unoccupied while the total number of conduction band electrons stays low. This is the case in a p-type or fully compensated sample where there are no neutral donors in thermal equilibrium. The spin polarized conduction band electrons are therefore captured rather quickly into the ionized donor states with density $n_{d,i}$ since the capture rate $\tau_c^{-1} \propto n_{d,i}$. For the sake of comparability we choose the number of (ionized) donors to be $n_{d,i} = 1.2 \times 10^{15}\,\mathrm{cm}^{-3}$ which results in $\tau_c \approx 14\,\mathrm{ps}$. This means that the polarized conduction band electrons are captured quasi-instantly onto the ionized donors on the timescale of the radiative decay and the conduction band spin lifetime where both quantities are typically $> 100\,\mathrm{ns}$ at cryogenic temperatures [2].

In order to quantify the last statement, the set of differential equations used for the spin pumping experiments in chapter 9 need to be modified which reads

$$\begin{aligned}
\frac{d}{dt}n_1(t) &= \frac{n_6(t)}{4\cdot\tau_C} - \frac{n_1(t)-n_3(t)}{2\cdot T_1} - \frac{n_1(t)}{\tau_{DAP}},\\
\frac{d}{dt}n_2(t) &= \frac{n_6(t)}{4\cdot\tau_C} - \frac{n_2(t)-n_4(t)}{2\cdot T_1} - \frac{n_2(t)-n_3(t)}{2\cdot T_\mathrm{x}} - \frac{n_2(t)}{\tau_{DAP}},\\
\frac{d}{dt}n_3(t) &= \frac{n_7(t)}{4\cdot\tau_C} - \frac{n_3(t)-n_1(t)}{2\cdot T_1} - \frac{n_3(t)-n_2(t)}{2\cdot T_\mathrm{x}} - \frac{n_3(t)}{\tau_{DAP}},\\
\frac{d}{dt}n_4(t) &= \frac{n_7(t)}{4\cdot\tau_C} - \frac{n_4(t)-n_2(t)}{2\cdot T_1} - \frac{n_4(t)}{\tau_{DAP}},\\
\frac{d}{dt}n_5(t) &= -\frac{n_5(t)}{\tau_A},\\
\frac{d}{dt}n_6(t) &= \frac{n_5(t)}{2\cdot\tau_A} - \frac{n_6(t)}{2\cdot\tau_C} + (1+\Xi)G_p - \frac{n_6(t)}{\tau_{band}} - \frac{n_6(t)-n_7(t)}{2\cdot\tau_s},\\
\frac{d}{dt}n_7(t) &= \frac{n_5(t)}{2\cdot\tau_A} - \frac{n_7(t)}{2\cdot\tau_C} + (1-\Xi)G_p - \frac{n_7(t)}{\tau_{band}} - \frac{n_7(t)-n_6(t)}{2\cdot\tau_s}.
\end{aligned}$$

Here, n_1-n_4 again denote the donor states. In the presence of both neutral donors and acceptors, an additional depletion channel for the donor electrons has to be assumed which is the well-known donor-acceptor pair recombination with a decay time of $\tau_{DAP} = 100\,\mu\mathrm{s}$ [93]. The state n_5 denotes the donor bound excitons. This state is only shown for the sake of completeness, since it will negligible for vanishing probe intensities. The states $n_6(n_7)$ reflect the occupation of the conduction band with spin up(down) where $\tau_s = 300\,\mathrm{ns}$ [2] is the spin lifetime in the conduction band and $\tau_{band} = 100\,\mathrm{ns}$[2] is the radiative band-to-band decay time. The symbol $\Xi = 0.25$ at λ_{max} represents the degree of spin polarization and G_p denotes the overall generation rate of conduction band electrons which is calculated assuming a spot radius of $225\,\mu\mathrm{m}$ and an absorption coefficient of $\alpha = 8.3 \times 10^{-2}\,\mathrm{cm}^{-1}$ for λ_{max} according to Fig. 11.6 (green squares). The set of differential equations is solved for the steady-state for different pump intensities, i.e., different G_p. The resulting donor electron polarization ρ is depicted in Fig. 11.7 (a). For low pump powers $< 1\,\mathrm{mW}$ the donor system nicely reflects the theoretically expected value. This is a huge advantage compared to other methods such as Hanle depolarization which usually measure the steady-state DSP Ξ_{ss} in the conduction band which is given by

$$\Xi_{ss} = \Xi \cdot \left(1 + \frac{\tau_{band}}{\tau_s}\right)^{-1} . \tag{11.20}$$

In this case however, the electrons are captured prior to spin relaxation or radiative decay into the ionized donor and the $\mathrm{D}^0\mathrm{X}$ absorption spectrum reflects the true spin polarization as long as $\tau_c \ll \tau_s$ and $\tau_c \ll \tau_{band}$. For increasing pump intensities the donor electron polarization ρ decreases which is due to the Orbach-type spin relaxation mediated by the increasing number of free electrons (cf. Fig. 11.7 (d)). This decrease of ρ continues until the donors are completely occupied (cf. Fig.11.7 (c)) and the polarization drops to zero which is marked by the red circle in each plot. In order to find a suitable operating point (green circle) for an experiment the normalized signal quality Q is depicted in Fig. 11.7 (b). This is defined as the product between the normalized donor occupation and the donor electron polarization and $Q = 1$ represents the signal to noise ratio of a typical $\mathrm{D}^0\mathrm{X}$ spectrum (compare Fig. 10.2). It is highly desirable to operate in a regime where the donor polarization is still constant and the donors are at least moderately occupied. In this example a pump power of $500\,\mu\mathrm{W}$ is chosen which results in $Q \approx 0.05$.

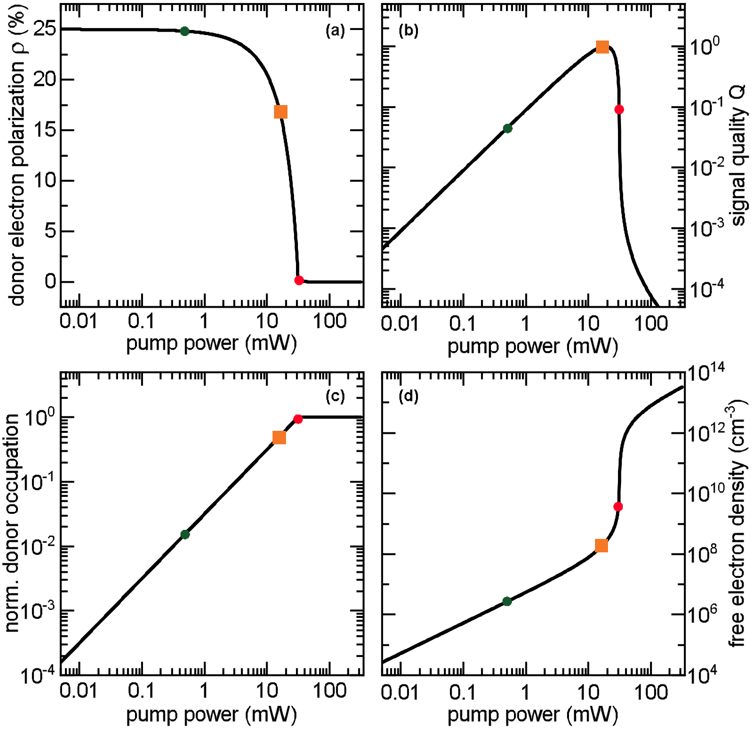

Figure 11.7: **(a)** Calculated steady-state donor polarization for different pump intensities. **(b)** Calculated signal quality Q for the detection of optical spin injection. **(c)** Calculated normalized donor occupation. **(d)** Calculated free electron density. In all panels the red dot denotes the pump power where the donor states are fully occupied, the orange square denotes the approximate validity of the calculation (see main text) and the green dot represents the suggested working point.

A COMMENT ON THE ORBACH-TYPE SPIN RELAXATION

According to the results of chapter 10.2 the donor electron spin relaxation rate due to the Orbach-type process reads

$$\frac{1}{T_1\left(n_6\right)}=\frac{1}{T_1}+\frac{E_0}{\Gamma_{D^0 T_2}}\frac{n_6}{\tau_c n_d}\zeta. \tag{11.21}$$

We recall that Eq. 11.21 has been formulated for a n-type sample where the density of Auger electrons $n_6 << n_d$ and therefore, $n_d = const$. In the present case of a p-type sample and polarized above bandgap excitation the Auger electron density has to be replaced by the number of photo excited electrons, i.e., $n_6 + n_7$. Furthermore, an increasing pump power results in an increasing free carrier density and a decreasing number of ionized donors. This, in turn causes the capture time $\tau_c \propto n_{d,i}^{-1}$ to diverge as $n_{d,i} \to 0$. Together with the increasing number of free carriers, this results in a constant T_1 time which would clearly contradict the mechanism of the Orbach-type process which dictates that the polarization and the T_1 time should approach zero as the free carrier density is increased. In order to account for this discrepancy the above calculation has been carried out with a constant capture time of $\tau_c = 27.8\,\mathrm{ps}$ which corresponds to $n_{d,i} = n_d/2$. Therefore, the above calculations are an excellent approximation for a relative donor occupation < 0.5. This is marked in each panel with an orange square.

12

SUMMARY

This thesis unambiguously clarified the microscopic origin of the enhanced donor electron spin relaxation rate caused by optical excitation. To this end, the complete dynamics of the optically driven donor system has been studied theoretically and experimentally. The experimental studies comprise a two-color absorption spectroscopy experiment for optical spin pumping exploiting the individual optical addressability of a specific electron spin state which originates from the magnetic-field induced splitting of the ultra-narrow D^0X transitions. In the case of continuous wave excitation, the spin pumping protocol resulted in a steady-state polarization of the donor spins of $\approx 70\,\%$ where the magnitude of the steady-state polarization is mainly governed by the optical excitation rate and the longitudinal spin lattice relaxation time T_1. In order to extract the T_1 time, time-resolved two-color absorption experiments have been performed which revealed a very pronounced correlation between the optical intensity and the transient spin polarization decay of the previously pumped donor electron system. This is intuitive to some extent since higher optical intensity leads to faster depopulation of the donor states and thus to a faster polarization decay. However, it has been shown that in order to quantitatively explain the degree of steady-state polarization and the polarization decay time simultaneously also a shortening of the T_1 time with increasing optical intensity is required. This shortening traces back to an Orbach-type relaxation mechanism where the hot Auger electrons from the D^0X recombination excite the donor 1S-A_1 to 1S-T_2 transition responsible for the thermal Orbach process. In fact, each Auger electron has enough excess energy to excite approximately thirty 1S-A_1 to 1S-T_2 transitions which would render optical spin pumping inefficient. However, an unpretentious calculation of the transient cooling dynamics of the Auger electrons by emission of optical and acoustic phonons showed that each Auger electron can excite on average only $\zeta \approx 2.3$ 1S-A_1 to 1S-T_2 transitions which is in remarkable agreement with the slightly larger value of $\zeta = 3.2$ found in the analysis of the transient polarization decay.

These findings bear consequences for optical initialization and manipulation of donor electron spins as a potential source for solid state qubits. The interplay between optically excited Auger electrons, the degree of spin polarization and T_1 relaxation entails that a high degree of spin polarization by optical pumping or any kind of optical manipulation comes at the cost of a reduced spin relaxation time T_1. This may also affect the spin dephasing time T_2 when the optically enhanced spin relaxation rate is larger than the intrinsic spin dephasing rate.

Furthermore, the extremely narrow linewidth enabled the test of fundamental semiconductor physics like the low temperature behavior of the silicon bandgap. Here, temperature dependent spectroscopy between 0.5 K and 9 K confirmed prior studies and the theoretical T^4 behavior. Moreover, the temperature dependent width of the transition was studied quantitatively in this temperature regime which revealed a pronounced broadening of the transition with a T^7 dependence attributed to elastic Raman scattering with phonons. While the optical linewidth in the sample under investigation is still resolved by an external cavity diode laser which is frequency stabilized by a high precision wavelength meter, this may not be possible in future studies on samples with lower doping concentration and potentially higher isotopical enrichment where the $\mathrm{D}^0\mathrm{X}$ linewidth should approach the natural linewidth which is below 1 MHz. Therefore, a laser stabilization scheme based on a high finesse optical cavity has been designed and characterized which provides sufficient frequency stability to unambiguously reveal the natural linewidth of any $\mathrm{D}^0\mathrm{X}$ transition in $^{28}\mathrm{Si}$.

Further insight into the electronic structure of the D^0 system was gained with the aid of magnetic field dependent absorption spectroscopy. This confirmed that in the presence of an external magnetic field the coupled system between donor spin and nuclear spin splits according to the Breit-Rabi equation for two spin $\frac{1}{2}$-particles resulting in six dipole allowed doublet transitions for the $\mathrm{D}^0\mathrm{X}$. Besides the confirmation of the optical selection rules of the $\mathrm{D}^0\mathrm{X}$ transition, the Landé g-factors of the electron, the light hole and the heavy hole have been determined with high accuracy. In addition, a pronounced anisotropy of the g-factors of the light hole and the heavy hole has been found and continuously determined for magnetic fields applied in between the [001] and [111] direction.

Finally, the combined insight into the electronic structure and spin dynamics of the D^0 system has lead to the proposal of further experiments. It has been shown that, despite the very small absorption coefficient of the D^0X transition, spin noise and occupation noise spectroscopy is feasible but represents a challenging task. Finally, we have outlined that the fast capture of conduction band electrons into ionized donor states in p-type silicon poses an elegant and efficient tool for the detection of optical spin injection in silicon.

Part VII

APPENDIX

ABSTRACT

This time-resolved photoluminescence study unambiguously reveals the microscopic origin of the slow photoluminescence rise time of the free exciton emission in bulk Gallium Arsenide (GaAs) at low temperatures. The ultra-pure GaAs sample under investigation allows to monitor the second LO-phonon replica of the free exciton transition which grants access to the exciton cooling dynamics and the population dynamics of the entire exciton ensemble. It is shown that the slow PL rise time is not solely governed by momentum relaxation of hot excitons towards the zone center but rather by the thermodynamic quasiequilibrium between free excitons and the uncorrelated electron hole plasma as expressed by the Saha equation.

This work was a collaboration with Dr. Steffen Bieker from the Julius-Maximilians Universität Würzburg and the presented results have already been published in Ref. [94].

A

EXCITON FORMATION IN GALLIUM ARSENIDE

It is well established that the onset of the free exciton photoluminescence (PL) in time-resolved studies at low temperatures can show a pronounced delay with respect to the excitation pulse [95, 96, 97, 98, 99]. Due to momentum conservation during the recombination process, only the fraction of the entire free exciton population $n_X(t)$ which is near the Brillouin zone center can be observed in experiments monitoring the free exciton zero-phonon line (FX) [100]. Therefore, an unambiguous interpretation of the complete free exciton dynamics requires experimental access to the entire free exciton population. This can be achieved by monitoring the free exciton second LO-phonon replica $(FX) - 2\hbar\Omega_{LO}$ where the K vector selection rules of the FX recombination are fully relaxed due to the flat dispersion of optical phonons [101].

The sample under investigation is a nominally undoped, 1.5 µm-thick epilayer of (001)-oriented MBE-grown GaAs where the low temperature PL spectrum depicted in Fig. A.1 is dominated by FX emission. The inherent weakness of the defect bound excitons, i.e., A^0X and D^0X suggest a residual impurity density $\leq 1 \times 10^{12}\,\mathrm{cm}^{-3}$ [98, 102].

Time resolution is achieved by optical excitation above the bandgap ($\lambda_{exc} = 780\,\mathrm{nm}$) by a pulsed Ti:sapphire laser with a pulse width of $\approx 2\,\mathrm{ps}$ and a repetition rate of 4 MHz[1] and the time-resolved PL is dispersed in a 250 mm focal length spectrometer with a $1200\,\mathrm{mm}^{-1}$ grating and detected by a streak camera.

Above bandgap excitation at low temperatures usually leads to the case where the optically induced carriers can be characterized by an effective temperature which is considerably larger than the lattice temperature [103, 104]. In the present case, pulsed excitation and subsequent cooling of the hot exciton ensemble leads to the transient cooling behavior depicted in Fig. A.2. The exciton temperature T_X is determined by a time-resolved Maxwellian lineshape analysis of the $(FX) - 2\hbar\Omega_{LO}$ line [105]. An exemplary spectrum of such a

---

[1] This repetition rate is accomplished by a dual pulse picker with an extinction ratio $< 1:1500$.

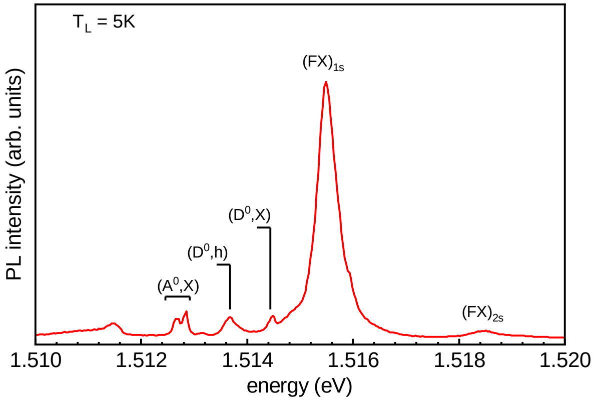

Figure A.1: Continuous wave PL spectrum of the investigated bulk GaAs sample at 5 K.

lineshape analysis is shown in the inset of Fig. A.2.

The temporal dynamics of T_X can be well described (red line in Fig. A.2) by

$$\frac{d}{dt}T_X = -\kappa(T_X - T_0), \tag{A.1}$$

with $\kappa = (0.9\,\mathrm{ns})^{-1}$ and the final exciton temperature $T_0 = 9\,\mathrm{K}$ which is higher than the lattice temperature $T_L = 5\,\mathrm{K}$. The latter may be explained by the fact that out of the thermalized exciton distribution only the low energy fraction, i.e., $K \approx 0$ recombine radiatively. Therefore, cold excitons are constantly removed from the ensemble giving rise to "recombination heating" [106]. Fig. A.3 (a) depicts time-resolved spectra of the spectrally integrated $(FX) - 2\hbar\Omega_{LO}$ transition for different excitation powers P_{exc} which clearly shows the delayed onset of the $(FX) - 2\hbar\Omega_{LO}$ PL and that the maximum of the PL timetrace gradually shifts to longer delays for decreasing P_{exc}. This result already indicates that the slow PL rise is not mainly governed by relaxation of large wavevector excitons towards the zone center since the $(FX) - 2\hbar\Omega_{LO}$ replica monitors the entire exciton density $n_X(t)$.

The population balance between the uncorrelated electron-hole

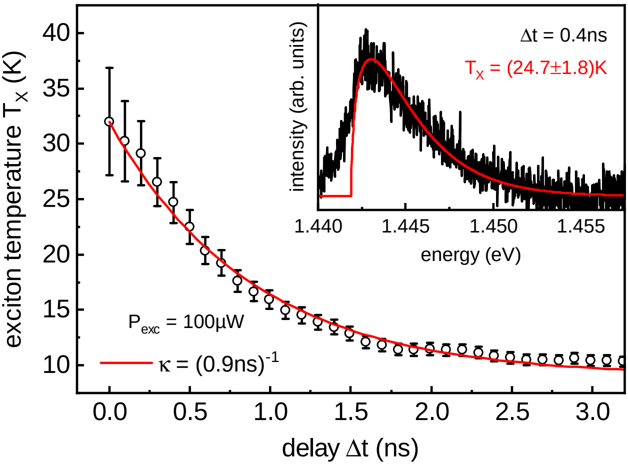

Figure A.2: Time-resolved cooling of the exciton ensemble. The solid red line indicates a cooling according to E. A.2 with $\kappa = (0.9\,\mathrm{ns})^{-1}$. The exciton temperature is extracted by a Maxwellian lineshape analysis which is exemplary shown in the inset.

plasma (EHP) and the free excitons is given by the Saha equation [107]

$$\frac{n_e n_h}{n_X} = \left(\frac{k_B T_X}{2\pi\hbar^2}\right)^{3/2} \left(\frac{m_e m_h}{m_X}\right)^{3/2} \exp\left(-\frac{E_B}{k_B T_X}\right), \tag{A.2}$$

where n_e, n_h and n_X represent the electron, hole and free exciton densities, m_i is the effective mass corresponding to $i = e, h, X$ and $E_B = 4.2\,\mathrm{meV}$ is the bulk exciton binding energy in GaAs [108]. With the substitution $n_e = n_h = (1 - f_X)n_0$ and $n_x = f_X n_0$, Eq. A.2 allows for the determination of the relative exciton fraction f_X from the total induced pair density n_0. An instinctive understanding of Eq. A.2, i.e., the population balanced between free carriers and excitons is given in Fig. A.4 where the exciton fraction f_X is shown in a color-coded plot as function of the exciton temperature T_X and the total pair density n_0.

For a constant exciton temperature T_X, an increase in the pair density n_0 leads to an increase in the exciton fraction f_X. This is caused by the decreasing spatial distance between electron and hole which favors exciton formation via Coulomb interaction. On

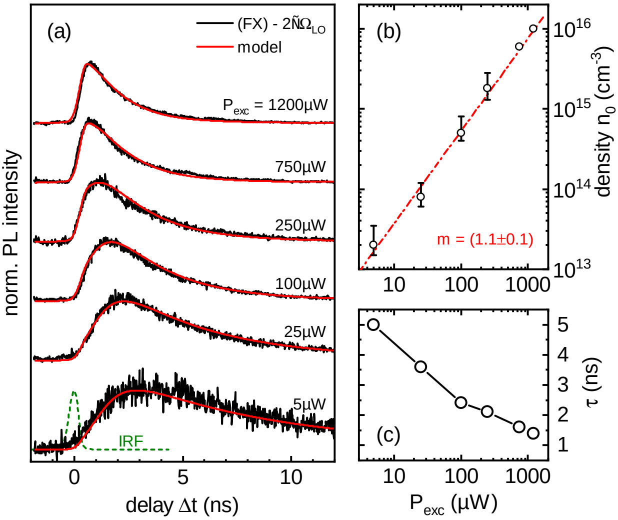

Figure A.3: **(a)** Excitation power dependence of the PL rise time detected on the $(FX) - 2\hbar\Omega_{LO}$ transition. The red solid lines are the results of the numerical model. **(b)** photocarrier density n_0 resulting from a single excitation pulse as extracted from the numerical model. **(c)** Decay constants τ used in the model.

the other hand, an increasing exciton temperature at constant pair density leads to thermal dissociation of excitons and thus a reduced exciton fraction f_X.

In the next step, a conceptual model for the temporal evolution of free exciton ensemble $n_X(t)$ after pulsed excitation is introduced which accounts for the transient cooling of the exciton ensemble via Eq. A.1 and the interplay between the exciton temperature and the free exciton density, i.e., the Saha equilibrium (Eq. A.2). It is further assumed that the photocarrier pair density $n_0(t)$ decays exclusively via the dominant channel of free exciton recombination neglecting the weak recombination from the EHP [99, 109]. Therefore, the time evolution of the pair density is given by

$$\frac{d}{dt} n_0 = -\frac{n_0 \times f_X(n_0, T_X)}{\tau}, \tag{A.3}$$

where τ denotes the ensemble lifetime. The time evolution of the free exciton ensemble is related to $n_0(t)$ through the Saha equation and reads

$$n_X(t) = n_0(t) \times f_X(n_0, T_X). \tag{A.4}$$

For each applied excitation power P_{exc} equations A.1-A.4 are solved numerically and the result convoluted is with the instruments response function (IRF) of the detector (green dashed line in Fig. A.3 (a)) where the ensemble lifetimes τ depicted in Fig. A.3(c) have been used. The respective results of the model are shown as red lines in Fig. A.3 (a) and exhibit extremely good agreement with the experimental data. As expected, the initial pair density $n_0(t = 0)$ found in the model calculation is proportional to the excitation power (compare Fig. A.3(c)).

Finally, an intuitive picture of the PL rise time and the gradual shift of the PL maximum can be gained by considering the trajectories, i.e., the model results of the PL rise time in Fig. A.4 (dash-dotted lines). At high excitation power, and thus high photocarrier density n_0, the formation of excitons is thermodynamically favored despite the high carrier temperature which leads to an early onset of the (FX) PL emission. At low excitation power however, the high initial temperature and the low carrier density lead to a substantially reduced exciton population at early delays which gradually builds up as the carriers relax their energy towards the zone center.

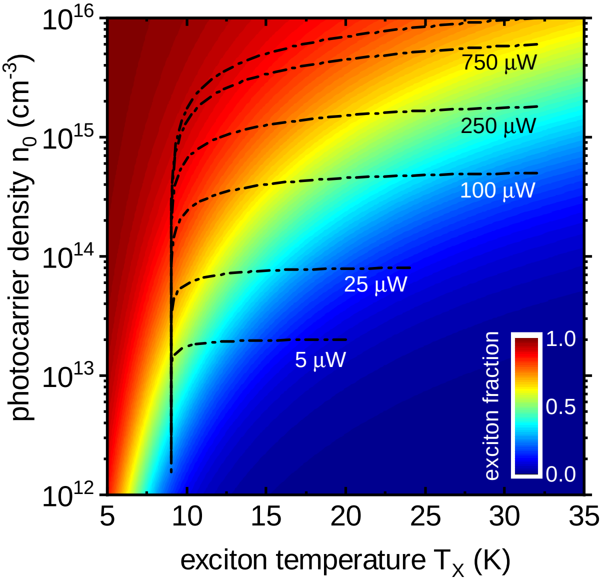

Figure A.4: Color-coded plot of the exciton fraction f_X as described by Eq. A.2. The dash-dotted lines indicate the trajectories of the model time traces shown in Fig. A.3(a).

BIBLIOGRAPHY

[1] B. E. Kane. “A silicon-based nuclear spin quantum computer.” In: *Nature* **393**.6681 (1998), pp. 133–137. ISSN: 1476-4687. DOI: 10.1038/30156.

[2] Ron Jansen. “Silicon spintronics.” In: *Nature Materials* **11** (2012), 400 EP –.

[3] S. A. Wolf et al. “Spintronics: A Spin-Based Electronics Vision for the Future.” In: *Science* **294**.5546 (2001), pp. 1488–1495. DOI: 10.1126/science.1065389.

[4] R. C. Fletcher et al. “Spin Resonance of Donors in Silicon.” In: *Phys. Rev.* **94** (5 1954), pp. 1392–1393. DOI: 10.1103/PhysRev.94.1392.2.

[5] A. Honig. “Polarization of Arsenic Nuclei in a Silicon Semiconductor.” In: *Phys. Rev.* **96** (1 1954), pp. 234–235. DOI: 10.1103/PhysRev.96.234.

[6] David Pines et al. “Nuclear Polarization and Impurity-State Spin Relaxation Processes in Silicon.” In: *Phys. Rev.* **106** (3 1957), pp. 489–498. DOI: 10.1103/PhysRev.106.489.

[7] Elihu Abrahams. “Donor Electron Spin Relaxation in Silicon.” In: *Phys. Rev.* **107** (2 1957), pp. 491–496. DOI: 10.1103/PhysRev.107.491.

[8] Laura M. Roth. “g Factor and Donor Spin-Lattice Relaxation for Electrons in Germanium and Silicon.” In: *Phys. Rev.* **118** (6 1960), pp. 1534–1540. DOI: 10.1103/PhysRev.118.1534.

[9] Hiroshi Hasegawa. “Spin-Lattice Relaxation of Shallow Donor States in Ge and Si through a Direct Phonon Process.” In: *Phys. Rev.* **118** (6 1960), pp. 1523–1534. DOI: 10.1103/PhysRev.118.1523.

[10] G. Feher. “Electron Spin Resonance Experiments on Donors in Silicon. I. Electronic Structure of Donors by the Electron Nuclear Double Resonance Technique.” In: *Phys. Rev.* **114**.5 (1959), pp. 1219–1244. DOI: 10.1103/PhysRev.114.1219.

[11] G. Feher et al. “Electron Spin Resonance Experiments on Donors in Silicon. II. Electron Spin Relaxation Effects.” In: *Phys. Rev.* **114** (5 1959), pp. 1245–1256. DOI: `10.1103/PhysRev.114.1245`.

[12] D. K. Wilson et al. “Electron Spin Resonance Experiments on Donors in Silicon. III. Investigation of Excited States by the Application of Uniaxial Stress and Their Importance in Relaxation Processes.” In: *Phys. Rev.* **124** (4 1961), pp. 1068–1083. DOI: `10.1103/PhysRev.124.1068`.

[13] Daniel Loss et al. “Quantum computation with quantum dots.” In: *Phys. Rev. A* **57** (1 1998), pp. 120–126. DOI: `10.1103/PhysRevA.57.120`.

[14] L. Childress et al. “Coherent Dynamics of Coupled Electron and Nuclear Spin Qubits in Diamond.” In: *Science* **314**.5797 (2006), pp. 281–285. DOI: `10.1126/science.1131871`.

[15] J. P. Gordon et al. “Microwave Spin Echoes from Donor Electrons in Silicon.” In: *Phys. Rev. Lett.* **1** (10 1958), pp. 368–370. DOI: `10.1103/PhysRevLett.1.368`.

[16] Richard E. George et al. “Electron Spin Coherence and Electron Nuclear Double Resonance of Bi Donors in Natural Si.” In: *Phys. Rev. Lett.* **105** (6 2010), p. 067601. DOI: `10.1103/PhysRevLett.105.067601`.

[17] A. M. Tyryshkin et al. “Electron spin relaxation times of phosphorus donors in silicon.” In: *Phys. Rev. B* **68** (19 2003), p. 193207. DOI: `10.1103/PhysRevB.68.193207`.

[18] Jarryd J. Pla et al. “A single-atom electron spin qubit in silicon.” In: *Nature* **489** (2012), 541 EP –.

[19] Eisuke Abe et al. “Electron spin coherence of phosphorus donors in silicon: Effect of environmental nuclei.” In: *Phys. Rev. B* **82** (12 2010), p. 121201. DOI: `10.1103/PhysRevB.82.121201`.

[20] W. M. Witzel et al. “Quantum theory of spectral-diffusion-induced electron spin decoherence.” In: *Phys. Rev. B* **72** (16 2005), p. 161306. DOI: `10.1103/PhysRevB.72.161306`.

[21] B. Andreas et al. “Determination of the Avogadro Constant by Counting the Atoms in a ^{28}Si Crystal.” In: *Phys. Rev. Lett.* **106** (3 2011), p. 030801. DOI: `10.1103/PhysRevLett.106.030801`.

[22] Alexei M. Tyryshkin et al. “Electron spin coherence exceeding seconds in high-purity silicon.” In: *Nature Materials* **11** (2011), 143 EP –.

[23] D. Karaiskaj et al. “Photoluminescence of Isotopically Purified Silicon: How Sharp are Bound Exciton Transitions?” In: *Phys. Rev. Lett.* **86** (26 2001), pp. 6010–6013. DOI: 10.1103/PhysRevLett.86.6010.

[24] M. L. W. Thewalt et al. “Direct observation of the donor nuclear spin in a near-gap bound exciton transition: P31 in highly enriched S28i.” In: *Journal of Applied Physics* **101**.8 (2007), p. 081724. DOI: 10.1063/1.2723181.

[25] A. Yang et al. “Homogeneous linewidth of the P31 bound exciton transition in silicon.” In: *Applied Physics Letters* **95**.12 (2009), p. 122113. DOI: 10.1063/1.3238268.

[26] W. Schmid. “Auger lifetimes for excitons bound to neutral donors and acceptors in Si.” en. In: *phys. stat. sol. (b)* **84**.2 (1977), pp. 529–540. DOI: 10.1002/pssb.2220840216.

[27] A. Yang et al. “Simultaneous Subsecond Hyperpolarization of the Nuclear and Electron Spins of Phosphorus in Silicon by Optical Pumping of Exciton Transitions.” In: *Phys. Rev. Lett.* **102** (25 2009), p. 257401. DOI: 10.1103/PhysRevLett.102.257401.

[28] M. Steger et al. “Optically-detected NMR of optically-hyperpolarized 31P neutral donors in 28Si.” In: *Journal of Applied Physics* **109**.10 (2011), p. 102411. DOI: 10.1063/1.3577614.

[29] M. Steger et al. “Quantum Information Storage for over 180 s Using Donor Spins in a 28Si “Semiconductor Vacuum”.” In: *Science* **336**.6086 (2012), pp. 1280–1283. DOI: 10.1126/science.1217635.

[30] Kamyar Saeedi et al. “Room-Temperature Quantum Bit Storage Exceeding 39 Minutes Using Ionized Donors in Silicon-28.” In: *Science* **342**.6160 (2013), pp. 830–833. DOI: 10.1126/science.1239584.

[31] Theodore G. Castner. “Orbach Spin-Lattice Relaxation of Shallow Donors in Silicon.” In: *Phys. Rev.* **155** (3 1967), pp. 816–825. DOI: 10.1103/PhysRev.155.816.

[32] Peter Y. Yu et al. *Fundamentals of Semiconductors.* Springer, 2010.

[33] James R. Chelikowsky et al. “Electronic structure of silicon.” In: *Phys. Rev. B* **10** (12 1974), pp. 5095–5107. DOI: 10.1103/PhysRevB.10.5095.

[34] W. Kohn et al. “Theory of Donor States in Silicon.” In: *Phys. Rev.* **98** (4 1955), pp. 915–922. DOI: 10.1103/PhysRev.98.915.

[35] G. Breit et al. “Measurement of Nuclear Spin.” In: *Phys. Rev.* **38** (11 1931), pp. 2082–2083. DOI: 10.1103/PhysRev.38.2082.2.

[36] Jan Valenta Ivan Pelant. *Luminescence Spectroscopy of Semiconductors*. Oxford University Press, 2012.

[37] J. R. Haynes. “Experimental Proof of the Existence of a New Electronic Complex in Silicon.” In: *Phys. Rev. Lett.* **4** (7 1960), pp. 361–363.

[38] F. Bloch. “Nuclear Induction.” In: *Phys. Rev.* **70** (7-8 1946), pp. 460–474. DOI: 10.1103/PhysRev.70.460.

[39] Theodore G. Castner. “Raman Spin-Lattice Relaxation of Shallow Donors in Silicon.” In: *Phys. Rev.* **130** (1 1963), pp. 58–75. DOI: 10.1103/PhysRev.130.58.

[40] Sebastian D. Saliba et al. “Linewidths below 100 kHz with external cavity diode lasers.” In: *Appl. Opt.* **48**.36 (2009), pp. 6961–6966. DOI: 10.1364/AO.48.006961.

[41] *Toptica DL 100 Manual*. Toptica Photonics AG. 2005.

[42] Mark Fox. *Optical Properties of Solids*. Oxford University Press, 2010.

[43] *Integriert-optische Modulatoren - Technische Information und Hinweise zur Bedienung*. Jenoptik AG.

[44] Frank Pobell. *Matter and Methods at Low Temperatures*. Springer, 2007.

[45] *DR400 Cryofree Dilution Refrigerator*. Oxford Instuments plc.

[46] E. Hal Bogardus et al. “Bound-Exciton, Free-Exciton, Band-Acceptor, Donor-Acceptor, and Auger Recombination in GaAs.” In: *Phys. Rev.* **176** (3 1968), pp. 993–1002. DOI: 10.1103/PhysRev.176.993.

[47] A. Yang et al. “High-resolution photoluminescence measurement of the isotopic-mass dependence of the lattice parameter of silicon.” In: *Phys. Rev. B* **77** (11 2008), p. 113203. DOI: 10.1103/PhysRevB.77.113203.

[48] Sadao Adachi. “GaAs, AlAs, and AlxGa1xAs: Material parameters for use in research and device applications.” In: *Journal of Applied Physics* **58**.3 (1985), p. 1. DOI: 10.1063/1.336070.

[49] Gary C. Bjorklund. “Frequency-modulation spectroscopy: a new method for measuring weak absorptions and dispersions.” In: *Opt. Lett.* **5**.1 (1980), pp. 15–17. DOI: 10.1364/OL.5.000015.

[50] Wolfgang Demtröder. *Laserspektroskopie - Grundlagen und Techniken*. Springer, 2000.

[51] James M. Supplee et al. “Theoretical description of frequency modulation and wavelengthmodulation spectroscopy.” In: *Appl. Opt.* **33**.27 (1994), pp. 6294–6302. DOI: 10.1364/AO.33.006294.

[52] Selina Volkert. “Konzeption, Aufbau und Evaluierung einer Pound-Drever-Hall basierten Laserfrequenzstabilisierung für hochauflösende Spektroskopie an isotopenreinem Silizium.” MA thesis. Leibniz Universität Hannover, 2018.

[53] Bahaa E. et al. *Fundamentals of Photonics*. John Wiley & Sons, Inc., 1991.

[54] Thomas Legero et al. “Tuning the thermal expansion properties of optical reference cavities with fused silica mirrors.” In: *J. Opt. Soc. Am. B, JOSAB* **27**.5 (2010), pp. 914–919.

[55] Eric D. Black. “An introduction to Pound-Drever-Hall laser frequency stabilization.” In: *American Journal of Physics* **69**.1 (2000), pp. 79–87. ISSN: 0002-9505. DOI: 10.1119/1.1286663.

[56] J. Alnis et al. “Subhertz linewidth diode lasers by stabilization to vibrationally and thermally compensated ultralow-expansion glass Fabry-P\’erot cavities.” In: *Phys. Rev. A* **77**.5 (2008), p. 053809. DOI: 10.1103/PhysRevA.77.053809.

[57] L. D Turner et al. “Frequency noise characterisation of narrow linewidth diode lasers.” In: *Optics Communications* **201**.4 (2002), pp. 391–397. DOI: 10.1016/S0030-4018(01)01689-3. (Visited on 09/23/2018).

[58] D. Karaiskaj et al. “Photoluminescence of Isotopically Purified Silicon: How Sharp are Bound Exciton Transitions?” In: *Phys. Rev. Lett.* **86**.26 (2001), pp. 6010–6013. DOI: `10.1103/PhysRevLett.86.6010`.

[59] P. J. Dean et al. “Absorption due to Bound Excitons in Silicon.” In: *Phys. Rev.* **163**.3 (1967), pp. 721–725. DOI: `10.1103/PhysRev.163.721`.

[60] Albion Yang. “Optical Hyperpolarization and Detection of Electron and Nuclear Spins of Phosphorus Donors in Highly Enriched 28Si.” PhD thesis. Simon Fraser University, 2010.

[61] A. Yang et al. “Single-frequency laser spectroscopy of the boron bound exciton in ^{28}Si.” In: *Phys. Rev. B* **80** (19 2009), p. 195203. DOI: `10.1103/PhysRevB.80.195203`.

[62] G. A. Thomas et al. “Optical study of interacting donors in semiconductors.” In: *Phys. Rev. B* **23** (10 1981), pp. 5472–5494. DOI: `10.1103/PhysRevB.23.5472`.

[63] Manuel Cardona et al. “Temperature Dependence of the Energy Gap of Semiconductors in the Low-Temperature Limit.” In: *Phys. Rev. Lett.* **92**.19 (2004), p. 196403. DOI: `10.1103/PhysRevLett.92.196403`.

[64] Y.P. Varshni. “Temperature dependence of the energy gap in semiconductors.” In: *Physica* **34**.1 (1967), pp. 149 –154.

[65] P. Becker et al. “Enrichment of silicon for a better kilogram.” In: *physica status solidi (a)* **207**.1 (2010), pp. 49–66. DOI: `10.1002/pssa.200925148`.

[66] Aymeric Ramiere et al. “Thermal resistance at a solid/superfluid helium?interface.” In: *Nature Materials* **15** (2016), 512 EP –. URL: `https://doi.org/10.1038/nmat4574`.

[67] D. E. McCumber et al. “Linewidth and Temperature Shift of the R Lines in Ruby.” In: *Journal of Applied Physics* **34**.6 (1963), pp. 1682–1684. DOI: `10.1063/1.1702657`.

[68] A. Ferrier et al. “Narrow inhomogeneous and homogeneous optical linewidths in a rare earth doped transparent ceramic.” In: *Phys. Rev. B* **87** (4 2013), p. 041102. DOI: `10.1103/PhysRevB.87.041102`.

[69] W. Burger et al. “Continuous high-resolution phonon spectroscopy up to 12 meV: Measurement of the A^+ binding energies in silicon.” In: *Phys. Rev. B* **33** (8 1986), pp. 5868–5870. DOI: `10.1103/PhysRevB.33.5868`.

[70] M.L.W. Thewalt. "Excited states of donor bound excitons and bound multiexciton complexes in silicon." In: *Solid State Communications* **21**.10 (1977), pp. 937 –939. DOI: https://doi.org/10.1016/0038-1098(77)90894-8.

[71] A.S. Kaminskii et al. "Luminescence of excitons bound to phosphorus atoms in silicon subjected to a magnetic field." In: *Sov. Phys. JETP* **52** (1980), p. 211.

[72] M. L. W. Thewalt et al. "Direct observation of the donor nuclear spin in a near-gap bound exciton transition: P31 in highly enriched Si28." In: *Journal of Applied Physics* **101**.8 (2007), p. 081724. ISSN: 0021-8979, 1089-7550. DOI: 10.1063/1.2723181.

[73] Jarryd J. Pla et al. "High-fidelity readout and control of a nuclear spin qubit in silicon." In: *Nature* **496** (2013), 334 EP –.

[74] B. K. Ridley. *Quantum Processes in Semiconductors*. Oxford University Press, 2013.

[75] D. K. Ferry. "First-order optical and intervalley scattering in semiconductors." In: *Phys. Rev. B* **14** (4 1976), pp. 1605–1609. DOI: 10.1103/PhysRevB.14.1605.

[76] P. T. Greenland et al. "Coherent control of Rydberg states in silicon." In: *Nature* **465** (2010), 1057 EP –. URL: https://doi.org/10.1038/nature09112.

[77] Carlo Jacoboni et al. "The Monte Carlo method for the solution of charge transport in semiconductors with applications to covalent materials." In: *Rev. Mod. Phys.* **55** (3 1983), pp. 645–705. DOI: 10.1103/RevModPhys.55.645.

[78] D. Karaiskaj et al. "Impurity Absorption Spectroscopy in ^{28}Si: The Importance of Inhomogeneous Isotope Broadening." In: *Phys. Rev. Lett.* **90** (18 2003), p. 186402. DOI: 10.1103/PhysRevLett.90.186402.

[79] Georges Lampel. "Nuclear Dynamic Polarization by Optical Electronic Saturation and Optical Pumping in Semiconductors." In: *Phys. Rev. Lett.* **20** (10 1968), pp. 491–493. DOI: 10.1103/PhysRevLett.20.491.

[80] R. R. Parsons. "Band-To-Band Optical Pumping in Solids and Polarized Photoluminescence." In: *Phys. Rev. Lett.* **23** (20 1969), pp. 1152–1154. DOI: 10.1103/PhysRevLett.23.1152.

[81] R Kubo. "The fluctuation-dissipation theorem." In: *Reports on Progress in Physics* **29**.1 (1966), pp. 255–284. doi: `10.1088/0034-4885/29/1/306`.

[82] M. Oestreich et al. "Spin Noise Spectroscopy in GaAs." In: *Phys. Rev. Lett.* **95** (21 2005), p. 216603. doi: `10.1103/PhysRevLett.95.216603`.

[83] Georg M. Müller et al. "Spin Noise Spectroscopy in GaAs (110) Quantum Wells: Access to Intrinsic Spin Lifetimes and Equilibrium Electron Dynamics." In: *Phys. Rev. Lett.* **101** (20 2008), p. 206601. doi: `10.1103/PhysRevLett.101.206601`.

[84] Ramin Dahbashi et al. "Optical Spin Noise of a Single Hole Spin Localized in an (InGa)As Quantum Dot." In: *Phys. Rev. Lett.* **112** (15 2014), p. 156601. doi: `10.1103/PhysRevLett.112.156601`.

[85] Georg M. Müller et al. "Semiconductor spin noise spectroscopy: Fundamentals, accomplishments, and challenges." In: *Physica E: Low-dimensional Systems and Nanostructures* **43**.2 (2010), pp. 569 –587. issn: 1386-9477. doi: `https://doi.org/10.1016/j.physe.2010.08.010`.

[86] R. de L. Kronig. "On the Theory of Dispersion of X-Rays." In: *J. Opt. Soc. Am.* **12**.6 (1926), pp. 547–557. doi: `10.1364/JOSA.12.000547`.

[87] Ramin Dahbashi. "Spinrauschen in nulldimensionalen Strukturen." PhD thesis. Leibniz Universität Hannover, 2015.

[88] Wilhelm Hanle. "Über magnetische Beeinflussung der Polarisation der Resonanzfluoreszenz." In: *Zeitschrift für Physik* **30**.1 (1924), pp. 93–105. issn: 0044-3328. doi: `10.1007/BF01331827`.

[89] J. L. Cheng et al. "Theory of optical spin orientation in silicon." In: *Phys. Rev. B* **83** (16 2011), p. 165211. doi: `10.1103/PhysRevB.83.165211`.

[90] G.G. Macfarlane et al. "Exciton and phonon effects in the absorption spectra of germanium and silicon." In: *Journal of Physics and Chemistry of Solids* **8** (1959), pp. 388 –392. issn: 0022-3697. doi: `https://doi.org/10.1016/0022-3697(59)90372-5`.

[91] Nils Scharnhorst. "Untersuchung von Auswahlregeln und Spindynamik in 28Si:P." MA thesis. Leibniz Universität Hannover, 2011.

[92] Eduard Sauter. "Spin-Dynamics in Semiconductors." MA thesis. Leibniz Universität Hannover, 2018.

[93] U. O. Ziemelis et al. "Sharp line donor–acceptor pair luminescence in silicon." In: *Canadian Journal of Physics* **59**.6 (1981), pp. 784–801. DOI: `10.1139/p81-102`.

[94] Steffen Bieker. "Time and Spatially Resolved Photoluminescence Spectroscopy of Hot Excitons in Gallium Arsenide." PhD thesis. Julius-Maximilians Universität Würzburg, 2016. URL: `urn:nbn:de:bvb:20-opus-134419`.

[95] Jun-ichi Kusano et al. "Extremely slow energy relaxation of a two-dimensional exciton in a GaAs superlattice structure." In: *Phys. Rev. B* **40** (3 1989), pp. 1685–1691. DOI: `10.1103/PhysRevB.40.1685`.

[96] R. Eccleston et al. "Exciton dynamics in a GaAs quantum well." In: *Phys. Rev. B* **44** (3 1991), pp. 1395–1398. DOI: `10.1103/PhysRevB.44.1395`.

[97] T. Amand et al. "Exciton formation and hole-spin relaxation in intrinsic quantum wells." In: *Phys. Rev. B* **50** (16 1994), pp. 11624–11628. DOI: `10.1103/PhysRevB.50.11624`.

[98] J. Aaviksoo et al. "Kinetics of free-exciton luminescence in GaAs." In: *Phys. Rev. B* **45** (3 1992), pp. 1473–1476. DOI: `10.1103/PhysRevB.45.1473`.

[99] A. Amo et al. "Interplay of exciton and electron-hole plasma recombination on the photoluminescence dynamics in bulk GaAs." In: *Phys. Rev. B* **73** (3 2006), p. 035205. DOI: `10.1103/PhysRevB.73.035205`.

[100] S. Permogorov. "Hot excitons in semiconductors." In: *physica status solidi (b)* **68**.1 (1975), pp. 9–42. DOI: `10.1002/pssb.2220680102`.

[101] E. Gross et al. "Free exciton motion in crystals and exciton-phonon interaction." In: *Journal of Physics and Chemistry of Solids* **27**.10 (1966), pp. 1647 –1651. DOI: `https://doi.org/10.1016/0022-3697(66)90244-7`.

[102] U. Heim et al. "Luminescence and Excitation Spectra of Exciton Emission in GaAs." In: *physica status solidi (b)* **66**.2 (1974), pp. 461–470. DOI: `10.1002/pssb.2220660208`.

[103] R. Ulbrich. “Energy Relaxation of Photoexcited Hot Electrons in GaAs.” In: *Phys. Rev. B* **8** (12 1973), pp. 5719–5727. DOI: `10.1103/PhysRevB.8.5719`.

[104] Jagdeep Shah. “Hot electrons and phonons under high intensity photoexcitation of semiconductors.” In: *Solid-State Electronics* **21**.1 (1978), pp. 43 –50. ISSN: 0038-1101. DOI: `https://doi.org/10.1016/0038-1101(78)90113-2`.

[105] D. Hägele et al. “Cooling dynamics of excitons in GaN.” In: *Phys. Rev. B* **59** (12 1999), R7797–R7800. DOI: `10.1103/PhysRevB.59.R7797`.

[106] D. Bimberg et al. “Recombination-induced heating of free carriers in a semiconductor.” In: *Phys. Rev. B* **31** (8 1985), pp. 5490–5493. DOI: `10.1103/PhysRevB.31.5490`.

[107] W. D. Kraeft et al. “Quantum statistics of an electron–hole plasma.” In: *physica status solidi (b)* **72**.2 (1975), pp. 461–474. DOI: `10.1002/pssb.2220720202`.

[108] M. R. Brozel et al. *Properties of Gallium Arsenide*. INSPEC London, 1996.

[109] J. Szczytko et al. “Determination of the Exciton Formation in Quantum Wells from Time-Resolved Interband Luminescence.” In: *Phys. Rev. Lett.* **93** (13 2004), p. 137401. DOI: `10.1103/PhysRevLett.93.137401`. URL: `https://link.aps.org/doi/10.1103/PhysRevLett.93.137401`.

LIST OF FIGURES

Figure 2.1 Crystal structure of silicon 17
Figure 2.2 Electronic bandstructure of silicon 18
Figure 2.3 Real space representation of the donor electron wave function 21
Figure 2.4 Donor energy levels 22
Figure 2.5 Solution to the Breit-Rabi equation 23
Figure 2.6 Optical Selection rules of donor bound excitons 26
Figure 2.7 Experimental data on T_1 relaxation 28
Figure 3.1 Schematic illustration of an external cavity diode laser 33
Figure 3.2 Cavity modes in an ECDL 34
Figure 3.3 Schematic diagram of a fiber-based EOM . . 35
Figure 3.4 Block diagram of the optical setup 37
Figure 3.5 CAD drawings of the home-built sample chamber 42
Figure 4.1 Sideband power of a phase modulated laser beam 44
Figure 4.2 Illustration of the phase modulation technique 45
Figure 4.3 Influence of Ω on the lineshape of the phase modulation signal 46
Figure 5.1 Transmission spectrum of a Fabry Perot cavity 53
Figure 5.2 Calculated linear CTE of ULE 55
Figure 5.3 FEM simulation for the additional ULE ring 57
Figure 5.4 Calculated coupling coefficients δ for different ULE ring thickness 58
Figure 5.5 The cavity assembly 60
Figure 5.6 Temperature response of the cavity assembly 61
Figure 5.7 Schematic setup for the Pound-Drever-Hall technique 62
Figure 5.8 Measured PDH error signal 64
Figure 6.1 Laser frequency noise PSD 66
Figure 6.2 Calibration of the WLM 67
Figure 6.3 Modulated temperature ramping of the cavity assembly 69
Figure 6.4 Time resolved laser frequency response to the modulated temperature ramping 71

Figure 7.1 D^0X absorption spectrum at zero magnetic field 78
Figure 7.2 Differential D^0X spectrum with skewed Lorentzian fit. 80
Figure 7.3 Temperature dependent D^0X spectra 82
Figure 7.4 Temperature dependence of the silicon bandgap 83
Figure 7.5 FEM simulation on the thermal boundary resistance 85
Figure 7.6 Temperature dependent linewidth and intensity of the D^0X transition 86
Figure 8.1 Experimental verification of the circularly polarized D^0X transitions 87
Figure 8.2 High resolution scan of the hyperfine splitting 88
Figure 8.3 Experimental verification of the linearly polarized D^0X transitions 89
Figure 8.4 Exemplary differential absorption spectra for g-factor determination 90
Figure 8.5 Frequency shifts of the six D^0X doublets in an external magnetic field 91
Figure 8.6 Anisotropy of the light hole g-factor 92
Figure 9.1 Exemplary D^0X spectra illustrating the electron spin polarization by optical pumping . 100
Figure 9.2 Excitation scheme for optical spin pumping of donor electrons 101
Figure 9.3 Calculation of the donor electron polarization 103
Figure 10.1 Knife edge scans of the pump and probe laser 106
Figure 10.2 Typical differential probe absorption spectrum of the D^0X transitions 5 to 8 107
Figure 10.3 Time-resolved polarization decay of the donor ensemble 108
Figure 10.4 Measured polarization decay time in dependence on optical probe intensity 109
Figure 10.5 Calculated dynamics of the hot Auger electrons after excitation into the conduction band 111
Figure 10.6 Schematic representation of the Orbach-type spin relaxation mechanism 113
Figure 10.7 Measured polarization decay time verifying the Orbach-type process 114
Figure 10.8 Donor electron polarization decays with model calculations 115

Figure 11.1 Schematic experimental setup for spin noise spectroscopy . . . 121
Figure 11.2 Exemplary spin noise spectrum of conduction band electrons in GaAs . . . 122
Figure 11.3 Illustration of circular dichroism of the $\mathrm{D}^0\mathrm{X}$ transition . . . 124
Figure 11.4 Calculated absorption spectra of $\mathrm{D}^0\mathrm{X}$ for doublets $(1,2)$ and $(11,12)$ . . . 128
Figure 11.5 Pitfalls in occupation noise spectroscopy . . . 129
Figure 11.6 Theoretical degree of spin polarization and experimental absorption coefficient for the silicon conduction band . . . 132
Figure 11.7 Illustration of the $\mathrm{D}^0\mathrm{X}$ transition as detector for polarized free electrons . . . 135
Figure A.1 Continuous wave PL spectrum of the investigated bulk GaAs sample at 5 K . . . 146
Figure A.2 Time-resolved cooling of the exciton ensemble 147
Figure A.3 Excitation power dependence of the PL rise time detected on the $(FX)-2\hbar\Omega_{LO}$ transition . . . 148
Figure A.4 Color-coded plot of the exciton fraction f_X . 150

LIST OF TABLES

Table 2.1 Natural abundance of silicon isotopes 19
Table 9.1 Summary of the direction of electron spin and relative oscillator strength associated with the six dipole allowed doublets. 99
Table 10.1 Parameters for the calculation of the Auger electron cooling dynamics. 112

SCIENTIFIC CONTRIBUTIONS

JOURNAL PUBLICATIONS

- **M. Beck**, N. V. Abrosimov, J. Hübner, and M. Oestreich, *Impact of optically induced carriers on the spin relaxation of localized electron spins in isotopically enriched silicon*, Phys. Rev. B, **99**, 245201 (2019).
- A. Rinn, T. Breuer, J. Wiegand, **M. Beck**, J. Hübner, R.C. Döring, M. Oestreich, W. Heimbrodt, G. Witte, and S.Chatterjee, *Interfacial molecular packing determines exciton dynamics in molecular heterostructures: the case of pentaceneperfluoropentacene*, ACS Appl. Mater. Interfaces **9**(48), 42020 (2017).
- **M. Beck**, J. Hübner, M. Oestreich, S. Bieker, T. Henn, T. Kiessling, W. Ossau, and L. W. Molenkamp, *Thermodynamic origin of the slow free exciton photoluminescence rise in GaAs*, Phys. Rev. B **93**, 081204(R) (2016).
- T. Henn, J.H. Quast, **M. Beck**, T. Kiessling, W. Ossau, *Hot electron spin diffusion in GaAs*, Eur. Phys. J. Plus **129**,118 (2014).
- T. Henn, A. Heckel, **M. Beck**, T. Kiessling, W. Ossau, L. W. Molenkamp, D. Reuter, and A. D. Wieck, *Hot carrier effects on the magneto-optical detection of electron spins in GaAs*, Phys. Rev. B **88**, 085303 (2013).

- **M. Beck**, N. V. Abrosimov, J. Hübner, and M. Oestreich, *Probe laser induced spin polarization of donor bound electrons in isotopically enriched* 28Si : P (Poster), DPG Spring Meeting of the Condensed Matter Section, Dresden (2017).

- **M. Beck**, N. V. Abrosimov, J. Hübner, and M. Oestreich, *Optical Hyperpolarization of donor bound electron spins in isotopically enriched* 28Si : P (Poster), NanoDay of the Laboratory for Nano and Quantum Engineering, Hannover (2017).

- **M. Beck**, N. V. Abrosimov, J. Hübner, and M. Oestreich, *Low Magnetic Field Wavelength Modulation Absorption Spectroscopy of Donor Bound Excitons in* 28Si : P (Poster), International Winterschool on New Developments in Solid State Physics, Mauterndorf (2016).

- **M. Beck**, N. V. Abrosimov, J. Hübner, and M. Oestreich, *Low Magnetic Field Wavelength Modulation Absorption Spectroscopy of Donor Bound Excitons in* 28Si : P (Poster), DPG Spring Meeting of the Condensed Matter Section, Regensburg (2016).

- **M. Beck**, N. V. Abrosimov, J. Hübner, and M. Oestreich, *Spin noise spectroscopy of artificial atoms in isotopically enriched* 28Si : P (Poster), DPG Spring Meeting of the Condensed Matter Section, Berlin (2015)

- **S. Volkert**, *Konzeption, Aufbau und Evaluierung einer Pound-Drever-Hall basierten Laserfrequenzstabilisierung für hochauflösende Spektroskopie an isotopenreinem Silizium*, master thesis (2018).
- **R. McClelland**, *Pound-Drever-Hall Stabilisation using a Fabry-Perot Cavity*, DAAD rise internship report (2016).
- **M. Steiniger**, *Laserfrequenzstabilisierung mittels Pound-Drever-Hall Verfahren*, bachelor thesis (2016).

CURRICULUM VITAE

Michael Beck, born November 5th, 1986 in Aalen

1994 - 2006	school education
June 2006	Abitur at the Theodor-Heuss-Gymanisum Aalen
2007 - 2013	Studies of physics at the Julius-Maximilians University (JMU) Würzburg
Oct. 2010	B.Sc. degree in physics at the JMU
May 2013	M.Sc. degree in physics at the JMU
since 2014	Employment as research assistant and preparation of the doctoral thesis at the Institute for Solid State Physics - Nanostructures Group, Leibniz University Hannover

ACKNOWLEDGMENTS

First of all, I want to express my gratitude to my supervisor Prof. Dr. Michael Oestreich for giving me the opportunity to pursue this exciting research topic. Thank you for all the countless discussions, meetings, ideas and for providing the financial resources required to realized my ideas.
I also would like to thank Prof. Dr. Fei Ding for being the second examiner and Prof. Dr. Christian Schüller for being the external examiner. Furthermore, I thank Prof. Dr. Klemens Hammerer for chairing the committee.
I'm in debt to PD Dr. Jens Hübner for proofreading the manuscript. Most importantly, I want to thank you, Jens, for your constant interest in my research, your friendly and open manner, the many serious - and not so serious - discussions and for always finding time in your busy schedule to help with the small and the big issues occurring in day-to-day work.
The successful implementation of the high finesse optical cavity for laser frequency stabilization would not have been possible without the advice from Kai Voges, Dr. Mirco Sierke and Dr. Thomas Legero who deserves special thanks for optical contacting of the cavity mirror and many practical tips on PDH locking. In this context, I also thank Rebecca McClelland, Michael Steiniger and Selina Volkert for their contributions to the "cavity project".
I want to express my thanks to Dr. Hendrik Kuhn, Pavel Sterin, Dr. Julia Wiegand, Dr. Ramin Dahbashi and Dr. Fabian Berski for always listening to my problems and for offering discussions and advice even in times of high workload in their own projects. I also thank Dr. Julia Wiegand for proofreading the final manuscript.
I further thank Ronny Hüther for introducing me to the moody cryostat in lab 135, and the whole team of the mechanic workshop for manufacturing essential parts of my setup.

When things don't work the way you have planned them in the lab - which is usually the case - it is important to have colleagues who cheer you up and provide some distraction. In that regard, I am very happy to be a part of the Nanostructures group and I want to thank all present members, which explicitly includes Prof. Dr. Rolf Haug, and all former members for the pleasant working atmosphere. I would particularly like to thank my office fellows: Hendrik, Julia, Lida, Magnus, Pavel and Ramin. I will always remember the (inappropriate) jokes, the casual darts sessions (special thanks to Magnus), lots of cookies, the ice cream breaks and many other things. I had a great time with all of you!
Furthermore, I thank my colleagues from the research training group "Quantum mechanical noise in complex systems" for the informal and friendly atmosphere at the joint seminars and for sharing the good times during workshops and barbecues.
I also want to thank my parents: *Danke für eure bedingungslose Unterstützung und eure aufmunternden Worte in schweren Zeiten. Ohne euch wäre ich nicht so weit gekommen!*
Finally, I whole-heartedly thank my girlfriend Stefanie for always believing in me, for her patience and support and for the wonderful time we've spent together.